ANALYSIS TECHNIQUES AND DIAGNOSTICS OF NON-RELATIVISTIC HADRON BEAMS

By

Christopher Richard

A DISSERTATION

Submitted to
Michigan State University
in partial fulfillment of the requirements
for the degree of

Physics - Doctor of Philosophy

2020

ABSTRACT

ANALYSIS TECHNIQUES AND DIAGNOSTICS OF NON-RELATIVISTIC HADRON BEAMS

By

Christopher Richard

Beam diagnostics are essential to the operation of hadron particle accelerators. They are used to tune the accelerator, verify beamline modes, ensure minimal beam losses, and characterize and monitor the beam quality. By adding and improving the measurements of the beam properties, the operation of the accelerator can be better informed and improved. Addition and improved measurements of the beam properties can be realized by developing new analysis techniques for the existing diagnostic devices.

This dissertation presents further analysis of measurements from two devices. Firstly, it discusses converting phase space measurements taken with an Allison scanner from position-angle coordinates to action-phase coordinates. In this coordinate system, the distribution is stable under changes to linear optics. This allows for direct comparison of phase space measurements taken at different locations or with different transverse focusing. In addition, this stability can make it easier to visualize and quantify the beam tails.

Secondly, beam profile measurements taken with Beam Position Monitors (BPMs) by measuring multiple harmonics are presented. The measurements are primarily focused on non-relativistic beams where the transverse and longitudinal profiles can be fit to the BPM signals. While these measurements were unsuccessful, it understood why they failed and how to avoid the same issues for future measurements.

Lastly, the design of a test stand to calibrate BPMs for non-relativistic effects is presented.

The test stand relies on a helical transmission line can can propagate signals with phase velocity of 0.03c. It is shown, with the appropriate geometry, that the phase velocity, pulse propagation, and field profiles from the helical transmission line can match the those of a non-relativistic bunch.

For Grandad

ACKNOWLEDGMENTS

First and foremost, I would like to thank my adviser, Steve Lidia. I am grateful for his encouragement and patience for me to pursue my own ideas that were fruitful as often as not. I also must thank my mentor at Fermilab, Sasha Shemyakin. Our almost daily discussions during my time working with him always gave me several ideas and paths forward to consider. I learn a great deal from Steve and Sasha about accelerator physics and how to be a successful scientist. In addition, thank you to the rest of my guidance committee: Steve Lund, Peter Ostroumov, Scott Bogner, and Selin Aviyente.

I am grateful for everyone who has helped me with experiments and through discussions. Special thanks must be given to Scott Cogan who developed the TIS waveforms and Sasha Plastun for taking measurements for me when I could not. Without them, my work with the BPMs would not be possible. In addition, I am indebted to the entire PIP2IT group at Fermilab Lionel Prost, Jean-Paul Carneiro, Arun Saini, and Bruce Hanna. They were tremendously helpful and welcoming during my short stay with them. Also, conversations with Greg Saewert were greatly helpful for the development of the helical transmission line.

I cannot thank everyone at Fermilab without acknowledging the Accelerator Science and Engineering Training (ASET) program at MSU. The ASET program made this research possible and provided me with the experience of spending a year working at Fermilab.

I am immensely grateful for my friends and fellow graduate students: James Kakos, Mel Miller, Bryan Isherwood, Jonathan Wong, Andrew Lajoie, Crispin Contreras, and many others. Many of them helped directly through conversations and critiquing my research presentations and they all provided much needed humor and emotional support. Lastly, thank you to my family. I know most of them have no idea what I do, but regardless they

provided continuous support.

TABLE OF CONTENTS

LIST OF TABLES

LIST OF FIGURES

Chapter 1

Introduction

1.1 Hadron Accelerators

Hadron accelerators for fundamental science research continue to push to higher beam power which is a product of the beam energy and current [1] (Fig. 1.1). The energy frontier is pushed in proton accelerators such as the Large Hadron Accelerator (LHC) at CERN. These accelerators are used for high energy physics research to produce and study exotic, heavy particles such as the Higgs boson. Other machines increase the power by increasing the beam current. These machines, such as the Facility for Rare Isotope Beams (FRIB) currently being built at Michigan State University (MSU), require higher currents to increase production rates of rare phenomena to achieve better statistics for the users. Hadron accelerators also have uses in the medical field, e.g. production of radioactive isotopes for tumor imaging, and industry, e.g. processing of semiconductors.

All of the machines in this large family of accelerators require minimal beam losses. For high power accelerators, the beams can cause significant damage to the accelerator if even a small portion of the beam is lost. Due to the significantly higher mass of hadrons compared to electrons, when hadrons strike a surface they deposit their energy over a relatively short distant which can cause significant damage to the material. For lower power machines, losses need to be avoided to reduce maintenance and increase up time. To ensure minimal losses, the beam quality must be measured and monitored with a diagnostic suite.

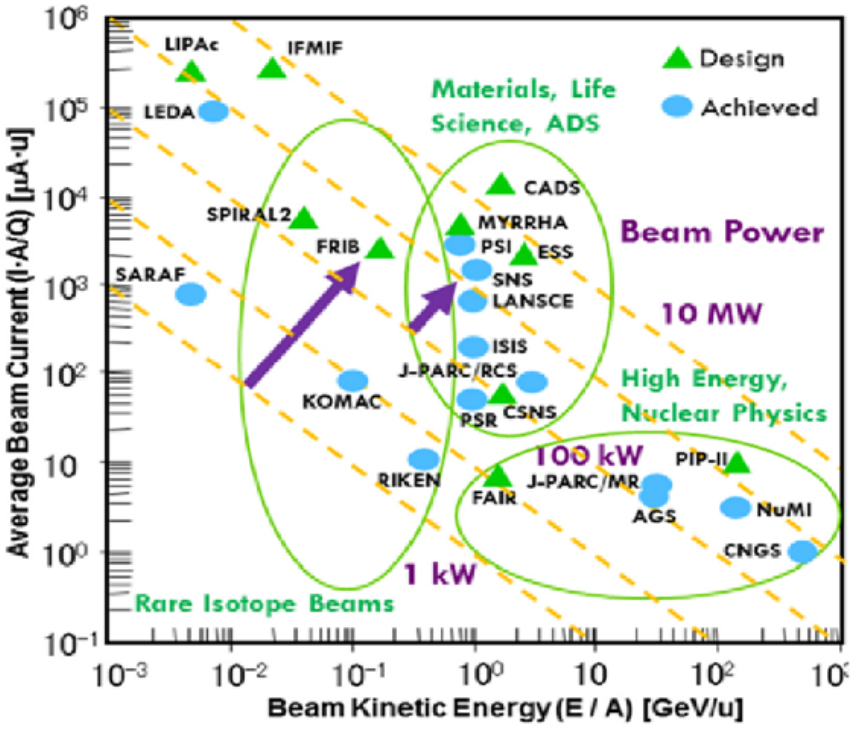

Figure 1.1: The beam of high intensity hadron accelerators [1]. The yellow lines represent beam power contours.

1.2 Accelerator front ends

One of the important sections of hadron accelerators is the front end. In the front end, the beam is created, focused, and initially accelerated before it enters the main accelerator. This section is typically comprised of four parts: the beam source, the Low Energy Beam Transport (LEBT), the Radio Frequency Quadrupole (RFQ), and Medium Energy Beam Transport (MEBT).

1.2.1 Hadron beam sources

Hadron beams are generated as a continuous, DC beam with energy ∼10s keV/u where u is the number of nucleons. Proton accelerators typically use H^- sources [9] because these are easier to produce than fully stripped hydrogen. The electrons are stripped off to create

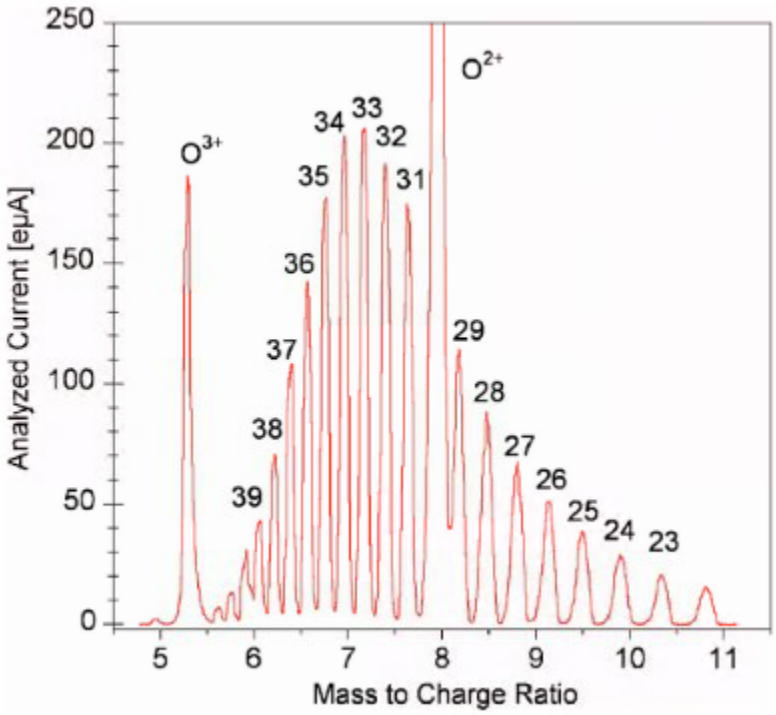

Figure 1.2: Charge states of uranium produced by and ECR ion source [2].

a proton beam further down the beamline once the beam as been accelerated. Heavy ion accelerators rely on sources such as Electron Cyclotron Resonance (ERC) ion sources to generate high charge state ions [10]. Both H^- and ECR ion sources produce a variety of ions. H^- sources can output electrons and several charge states of hydrogen. ECR ion sources produces a wide range of charge states, e.g. the produced charge states of uranium from an ECR ion source are shown in Fig. 1.2.

1.2.2 Low energy beam transport

The beam from the ion source goes into the LEBT. The LEBT ideally selects a single charge state created by the ion source to inject into the main accelerator. Accelerators typically can only propagate one charge state and the rest would be lost because accelerators rely on electric and magnetic fields to focus and accelerate the beam. To remove the contaminating

particles, the beam is passed through dipole bending magnets. The bending radius r of a particle with mass m, charge q, and momentum p traveling through dipole with strength B is

$$r = \frac{m}{q}\frac{p}{B}. \tag{1.1}$$

Therefore, different charge states of a given isotope will be deflected by a different amount. By choosing the correct dipole strength, the desired charge state and momentum will pass through the bend. However, because the beam pipe has a non-zero aperture, it allows for some range of momenta Δp and range of charge states Δq to pass through the bend. These contaminating charge states follow different trajectories and can be removed by limiting the aperture of the beam pipe by inserting slits to intercept the unwanted particles.

In addition, the LEBT focuses the beam transversely. Transverse focusing relies on linear focusing forces from either electric or magnetic quadruples or solenoid magnets. The focusing from a quadrupole field provides uncoupled motion between the x and y planes. However, the fields from these magnets will focus the beam in one plane and defocus in the other. Therefore, at least two quadrupole magnets are required to proved net focusing in both x and y planes. Typically quadrupoles are grouped into structures of two or three magnets, call doublets and triplets respectively, that will focusing in both planes. Solenoid magnets provide focusing in x and y which can make them more compact. However, they couple the motion in the x and y planes making the dynamics more complex [11].

1.2.3 Radio frequency quadrupole

The LEBT transports the beam into the RFQ. The RFQ provides traverse focusing and accelerates the beam to energies on the order of 1 MeV/u [3]. The transverse focusing is

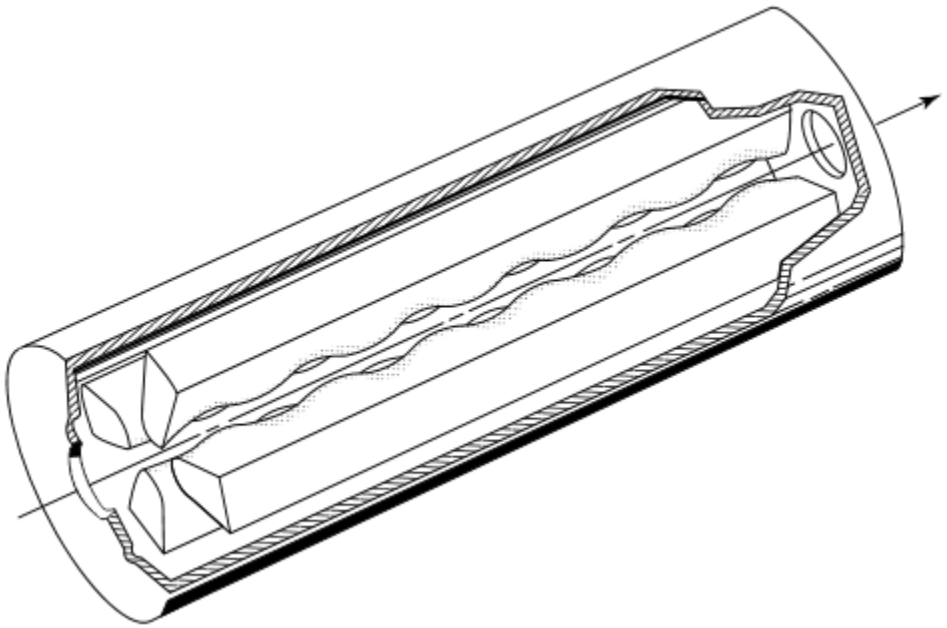

Figure 1.3: Sketch of an RFQ [3]. Four vanes create a quadrupole field to focus the beam transversely. The vanes are modulated to create a longitudinal field to accelerator the beam.

provided by a time-varying electric field modulated at a radio frequency. The field is shaped by four conducting vanes (see Fig. 1.3) to create a quadrupole field. Because the electric field is modulated in time, the structure alternates between focusing and defocusing in each plane, resulting in net focusing in both planes. To accelerate the beam, the pole tips of the vanes are shaped with a sinusoidal modulation to create a longitudinal electric field. Because this structure relies on a radio frequency (RF) field, only particles that are affected a positive longitudinal electric field will be accelerated. Particles that are aligned with the negative field will be decelerated. This results in the DC input beam becoming separated into discrete groups called bunches separated in time by the RF period. This time structure of the beam is often called a bunch train.

1.2.4 Medium energy beam transport

After the RFQ, the beam propagates through the MEBT which transports the beam to the main accelerator. Transverse focusing is provided with quadrupole or solenoid magnets. In addition, the MEBT focuses the beam longitudinally to maintain the bunch structure. The longitudinal focusing is provided by an RF buncher cavity. These devices have an RF longitudinal electric field that is phased such that particle with the average energy will arrive when the electric field is zero. Particles with higher energy will arrive early and a negative electric field will decelerate them. Likewise, lower energy particles will arrive late and positive electric field will accelerate them.

The MEBT also must manipulate the beam so it is within the acceptance of the main accelerator to avoid losses. This is further discussed in section 1.3.2. In addition, it may be necessary to remove particles that are far from the center of the beam, typically called halo or tails, because they are the most likely to be lost in the accelerator. These particles can be removed by inserting plates called scrapers into the beamline to intercept the extraneous particles. It is often preferable to purposefully remove the halo and tails in the MEBT when they have low energy an will not cause significant damage rather than risk them being lost later at higher energies where the damage can be more detrimental.

1.2.5 Measured beamlines

The measurements presented in this dissertation were taken in the front ends of two separate accelerators. The first is the Proton Improvement Plan 2 Injector Test (PIP2IT) [12]. This accelerator is a test stand for the front end of the Proton Improvement Plan 2 (PIP-II) project at Fermilab [13]. PIP2IT accelerates H^- ions starting with a 30 keV source and a solenoid

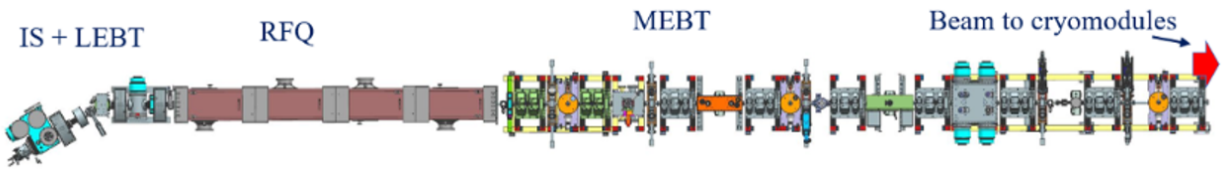

Figure 1.4: PIP2IT front end.

focusing LEBT (Fig. 1.4). The RFQ operates at 162.5 MHz and accelerates the beam to 2.1 MeV. The transverse focusing in the 10 m MEBT is provided by two quadrupole doublets and seven triplets and the longitudinal focusing is proved by three RF buncher cavities.

Measurements were also taken with the front end at the Facility for Rare Isotope Beams (FRIB) at Michigan State University (MSU) [14]. Beams of heavy ions up to ^{238}U are created with an ECR ion source at 7 keV/u. The LEBT focuses the beam with a combination of solenoids and quadrupoles starting at ground level then vertically dropping 30 feet to the RFQ (Fig. 1.5). The RFQ operates at 80.5 MHz and accelerates the ions to 0.5 MeV/u. The MEBT focusing the beam with four quadrupole triplets and two RF bunchers.

1.3 Transverse beam dynamics

1.3.1 Single particle dynamics

The dynamics of a particle of mass m in an electromagnetic field defined by the potentials ϕ and $\mathbf{A}$ can be determined from the Hamiltonian [11]

$$H_t = e\phi + T = e\phi + c\sqrt{m^2c^2 + (\mathbf{P} - e\mathbf{A})^2} \tag{1.2}$$

where $\mathbf{P}$ is the canonical momentum $\mathbf{P} = \mathbf{p} + e\mathbf{A}$ [15]. For simplicity, this Hamiltonian assumes a linear coordinate system which is sufficient for the discussion here of front ends

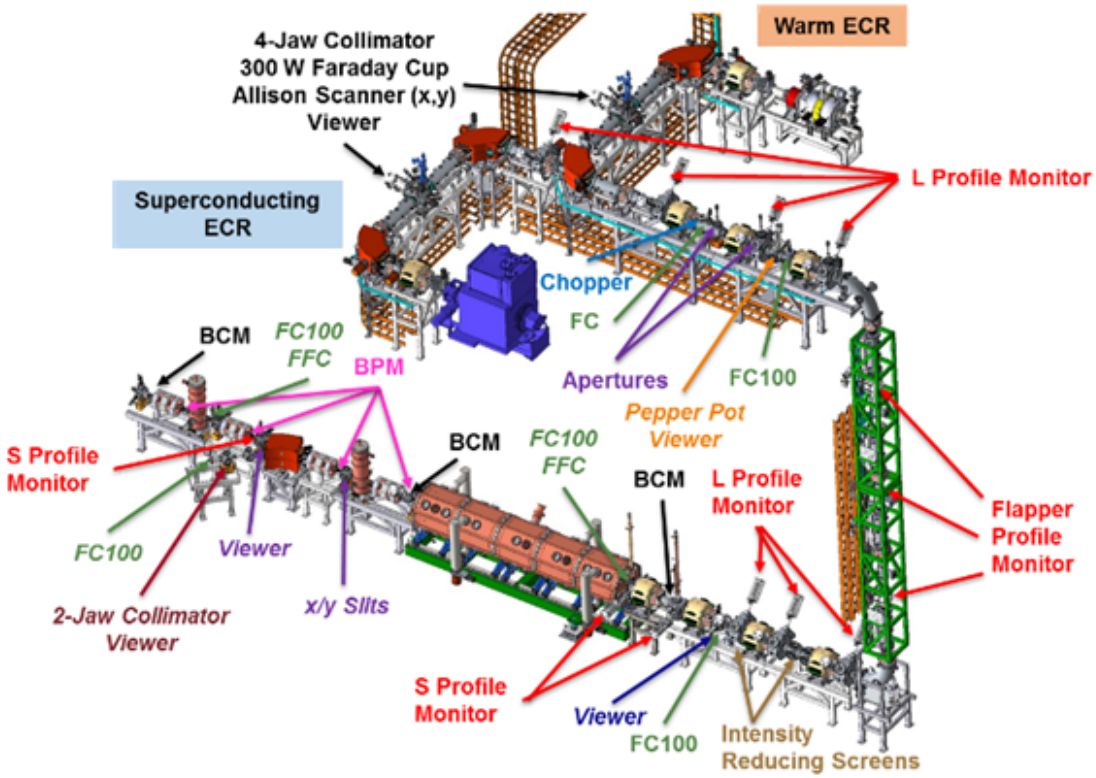

Figure 1.5: Overview of the diagnostics in the FRIB front end.

because they are predominately straight. A more general form in curvilinear coordinates can be used when bends are a significant feature of the optics [11]. The independent variable of this Hamiltonian is time t. In accelerators, it is often preferable to use the longitudinal coordinate z as the independent variable as it determines the location in the machine. With z as the independent variable and normalizing to the total momentum p, the Hamiltonian becomes

$$H_z = -\frac{eA_z}{p} - \sqrt{1 - \left(\frac{p_x}{p}\right)^2 + \left(\frac{p_y}{p}\right)^2} \tag{1.3}$$

$$H_z = -\frac{eA_z}{p} - \sqrt{1 - x'^2 + y'^2} \tag{1.4}$$

where $x' = dx/dz$ and $y' = dy/dz$ are referred to as angles and measured in radians.

Hamilton's equations are

$$\frac{\partial x}{\partial z} = \frac{\partial H_z}{\partial x'} \tag{1.5}$$

$$\frac{\partial x'}{\partial z} = -\frac{\partial H_z}{\partial x} \tag{1.6}$$

which, using the paraxial approximation $x' \ll 1$ and $y' \ll 1$, gives the equation of motion

$$-u'' = -\frac{e}{p_z}\frac{\partial A_z}{\partial u}. \tag{1.7}$$

For linear, uncoupled optics, e.g. a quadrupole magnet with $A_z = G(y^2 - x^2)/2$, the equation of motion becomes

$$u'' + \kappa u = 0 \tag{1.8}$$

where κ is the focusing strength of the optic. This is known as Hill's equation. In general κ is a function of z as the beamline consists of focusing magnets separated by regions without focusing fields, $\kappa = 0$ called drift spaces. Hill's equation is widely used in accelerator physics because most accelerators primarily rely on linear optics to focus the beam. However, to satisfy Maxwell's equations, the focusing fields must have non-linear components. The effects from the non-linear components are lessened by purposefully designing the magnets to minimize the non-linearities and simulations can be performed if it necessary to account for these effects [16].

The linear dynamics of the particles can be determined by integrated Hill's equation over the beamline. However, it is often more practical to use a transfer matrix $\mathbf{M}$ that relates

the coordinates of the particle at one location z_1 to another z_2

$$\begin{bmatrix} u \\ u' \end{bmatrix}_{z=z_2} = \mathbf{M}(z_2|z_1) \begin{bmatrix} u \\ u' \end{bmatrix}_{z=z_1} . \tag{1.9}$$

Equation 1.9 holds for uncoupled, linear transverse motion as described by Eq. 1.8. It can also be generalized to the full 4D transverse phase space (x, x', y, y') and the full 6D dynamics $(x, x', y, y', \Delta z, \Delta p_z/p_z)$. These matrices can be found in literature for most beamline elements such as dipoles, quadrupoles, and solenoids [17].

1.3.1.1 The betatron function

The beamline optics tend to arranged in quasi-periodic structures. Because of this, the motion of the particles can be described in phase-amplitude form

$$u = \sqrt{\epsilon\beta(z)}\cos(\phi(z) - \phi_0) \tag{1.10}$$

where ϵ is an overall amplitude and ϕ_0 is an arbitrary phase offset. The dynamics are determined by the betatron function $\beta(z)$ and the betatron phase $\phi(z)$. The dynamics of β and ϕ can be determined by taking the second derivative of Eq. 1.10, plugging into Eq. 1.8, then separately setting the cosine and sine terms to zero. This gives two equations

$$\frac{1}{2}\left(\beta\beta'' - \frac{1}{2}\beta'^2\right) - \beta^2\phi'^2 + \beta^2\kappa = 0 \tag{1.11}$$

$$\beta'\phi' + \beta\phi'' = 0. \tag{1.12}$$

Equation 1.12 can easily be integrated to determine $\psi(z)$

$$\beta'\phi' + \beta\phi'' = (\beta\phi')' = 0 \tag{1.13}$$

$$\beta\phi' = \text{constant} \equiv 1 \tag{1.14}$$

$$\phi(z) = \phi_0 + \int_0^z \frac{\mathrm{d}\bar{z}}{\beta(\bar{z})}. \tag{1.15}$$

Equation 1.14 can then be used in Eq. 1.11 to determine the dynamics of the $\beta(z)$

$$\frac{1}{2}\beta\beta'' - \frac{1}{4}\beta' + \kappa\beta^2 = 0. \tag{1.16}$$

The betatron function is typically accompanied by $\alpha = -\frac{1}{2}\beta'$ and $\gamma = (1+\alpha^2)/\beta$. Together, α, β, and γ are known as the Twiss parameters and their physical meaning is discussed is section 1.3.2. The betatron phase advance has a well defined meaning for periodic focusing lattices because the particle trajectory will also be periodic with the period defined by where $\phi(z) = 2\pi n$. This is is typically characterized by the betatron tune which is the number of oscillations per lattice period. For quasi-periodic focusing structures, such as are found in linacs, the exact nature of the betatron phase is more complicated but the same intuition holds.

1.3.1.2 Action-phase coordinates

The Hamiltonian shown in Eq. 1.4 is useful because uses the physical coordinates (u, u', z). It can be simpler analytically to work in normalized coordinates $(w, \dot{w}, \phi)$ where ϕ is the

betatron phase and $\dot{w} = \mathrm{d}w/\mathrm{d}\phi$ [11]. In this coordinate system the Hamiltonian is

$$H_w = \frac{1}{2}w^2 + \frac{1}{2}\dot{w} \tag{1.17}$$

A canonical transformation can be made to action-phase coordinates (J, ϕ, ϕ) (that is not a typo, the betatron phase is being used for a transverse and longitudinal coordinate) using the generator function

$$G = -\frac{1}{2}w^2 \tan(\phi - \phi_0) \tag{1.18}$$

where ϕ_0 is an arbitrary phase. The normalized coordinates can be found by

$$\frac{\partial G}{\partial w} = \dot{w} = -w\tan(\phi - \phi_0) \tag{1.19}$$

$$\frac{\partial G}{\partial \psi} = \frac{-w^2}{2\cos^2(\phi - \phi_0)} \equiv J \tag{1.20}$$

and solving for w and $\dot{w}$

$$w = \sqrt{2J}\cos(\phi - \phi_0) \tag{1.21}$$

$$\dot{w} = -\sqrt{2J}\sin(\phi - \phi_0). \tag{1.22}$$

This gives the Hamiltonian

$$H_w = J \tag{1.23}$$

and the equations of motion in action-phase coordinates are

$$\dot{J} = 0 \tag{1.24}$$

$$\dot{\phi} = 1. \tag{1.25}$$

The action J is a constant of motion and the transverse dynamics are entirely determined by the betatron phase advance.

To relate this coordinate system to physical coordinates, Eqs. 1.21 and 1.22 can be written in terms of u and u'

$$w = \frac{u}{\sqrt{\beta}} \tag{1.26}$$

$$\dot{w} = \sqrt{\beta}u' + \alpha w. \tag{1.27}$$

Plugging these into $H_w = J$ the action of a particle can be determined in terms of its location in phase space u, u', and the Twiss parameters

$$J = \frac{1}{2}\left(\beta u'^2 + 2\alpha u u' + \gamma u^2\right). \tag{1.28}$$

This is the equation of an ellipse in $u - u'$ phase space with orientation determined by the Twiss parameters and size determined by J. The location of the particle on this ellipse is determined by ϕ

$$\phi = -\arctan\left(\frac{\alpha u + \beta u'}{u}\right). \tag{1.29}$$

The beam dynamics can therefore by interpreted as particles traveling along these ellipses of constant action. In real space, the orientation of the ellipse will evolve according the the

applied focusing, but the action of the particle will remain constant.

1.3.2 Phase space dynamics

The above derivations concern the dynamics of a single particle. Unsurprisingly, a beam consists of a collection of particles. While the individual particles travel along elliptical trajectories in phase space as defined by the action and betratron phase, the general distribution is not necessarily elliptical. However, the Twiss parameters and emittance are still well defined for general beam distributions by describing the ellipse that encompasses the beam distribution. The emittance and Twiss parameters can be found from a general beam distribution by

$$\epsilon = \sqrt{\left\langle u^2 \right\rangle \left\langle u'^2 \right\rangle - \left\langle uu' \right\rangle} \tag{1.30}$$

$$\beta = \frac{\left\langle u^2 \right\rangle}{\epsilon} \tag{1.31}$$

$$\alpha = -\frac{\left\langle uu' \right\rangle}{\epsilon} \tag{1.32}$$

$$\gamma = \frac{\left\langle u'^2 \right\rangle}{\epsilon} \tag{1.33}$$

where $\langle ... \rangle$ denotes averages. These are typically taken from rms values. This brings physical meaning to the parameters: the emittance, a conserved quantity, is the rms area of the beam in phase space and the Twiss parameters are the second order moments normalized to the emittance. The geometric emittance ϵ is often scaled by the relativistic factors and referred to as the normalized emittance $\epsilon_n = \gamma_r \beta_r \epsilon$. This is done to keep the emittance constant as the beam is acceleratred. Equation 1.16, determining the evolution of the betatron function through the beamline, is a description of the evolution of the beam size.

Like the first order moments, the second order moments can also be propagated through focusing elements using the transfer matrices. The second order moments can be put in matrix form

$$\sigma = \begin{bmatrix} \langle u^2 \rangle & \langle uu' \rangle \\ \langle uu' \rangle & \langle u'^2 \rangle \end{bmatrix} \tag{1.34}$$

which can be propagated by the transfer matrices like a second order tensor

$$\sigma(z = z_2) = M^T(z_2|z_1)\sigma(z = z_1)M(z_2|z_1). \tag{1.35}$$

Note that $|\sigma| = \epsilon^2$ and therefore must be constant. To preserve the determinate, the transfer matrices must be symplectic.

There is a maximum emittance, called the acceptance, that can be propagated through the accelerator without losses. For transverse dynamics this is determined by the optics and the apertures of the beam pipe and beamline elements. In addition, to avoid losses, the MEBT optics must correctly orient the beam in phase space at the end of the front end to 'match' the beam to the accelerator optics. This is achieved by aligning the beam distribution with the expected ellipse in phase space that the particle trajectories will follow. If the beam is not properly matched, the beam will oscillate around the matched condition resulting in larger beam sizes that can cause losses.

1.3.3 Space charge effects

The beam is a collection of charged particles and, for intense beams, the electric field created by these particles will affect the dynamics. This results in a non-linear addition to Hill's

equation [18]

$$u'' + \kappa u = -\frac{q}{m\gamma_b^3\beta_b^2 c^2}\frac{\partial \phi}{\partial u} \tag{1.36}$$

where q and m are the charge and mass of the particles, γ_b is the Lorenz factor, $\beta_b c$ is the beam velocity, and ϕ is the potential of the self-field. This can be approximated for a uniform beam of radius r_b and line charge density λ as

$$u'' + \kappa u = \frac{Q}{r_b^2} \tag{1.37}$$

where Q is called the normalized perveance

$$Q = \frac{q\lambda}{2\pi\epsilon_0 m\gamma_b^3\beta_b^2 c^2}. \tag{1.38}$$

This effect of space charge decays rapidly with increasing beam energy as $\gamma_r^3\beta_r^2$. Near the source typical values of Q are on the order of 10^{-2} and higher energies $Q \leq 10^{-6}$. This linear space charge force causes a reduction of the betatron phase advance called betatron tune depression.

Space charge forces also affect the beam size. The dynamics of the second order moments can be determined from Eq. 1.37 by multiplying by u and taking an average

$$\left\langle uu'' \right\rangle + \kappa \left\langle u^2 \right\rangle - \frac{Q}{r_b}\left\langle u^2 \right\rangle = 0 \tag{1.39}$$

The beam radius can be defined at twice the rms beam size $r_b = 2\left\langle u^2 \right\rangle^{1/2}$ and this gives a definition of the edge emittance of $\epsilon = 4\epsilon_{\text{rms}}$. These definitions are exact for a Kapchinsky-Vladimirsky (KV) disitrbution [19] and are approximations for general distributions [18].

The derivatives of r_b are

$$r' = 2\frac{\langle uu' \rangle}{\langle u^2 \rangle^{1/2}} = 4\frac{\langle uu' \rangle}{r_b} \tag{1.40}$$

$$r'' = 4\frac{\langle uu'' \rangle}{r_b} + \frac{\epsilon^2}{r_b^3}. \tag{1.41}$$

Plugging these into Eq. 1.39 gives the envelope equation dictating the dynamics of the beam radius

$$r_b'' + \kappa r_b - \frac{Q}{r_b} - \frac{\epsilon^2}{r_b^3} = 0 \tag{1.42}$$

The beam radius evolves according to the beam optics κ. In addition, there is a thermal defocusing affect related to the emittance and a space charge defocusing affect that proportional to Q. The beam is said to be space charge dominated if $Q/r_b \gg \epsilon^2/r_b^3$ and emittance dominated if $Q/r_b \ll \epsilon^2/r_b^3$.

For a general beam distribution, the space charge forces will be non-linear. These forces distort the distribution in phase space causing filamentation resulting in tail and halo grown and increasing the emittance (Fig. 1.6). These affects need to be characterized and, if necessary, compensated for before the beam leaves the MEBT to ensure a quality beam is accelerated.

1.4 Diagnostics

It is crucial to ensure a high quality beam enters the main accelerator. Not only is this important to minimize beam losses but also it challenging to deliver a quality beam to the users if the initial conditions are poor. To characterize and monitor the beam quality, the front ends have extensive diagnostic suites (e.g. see Fig. 1.5) because the beam is traveling

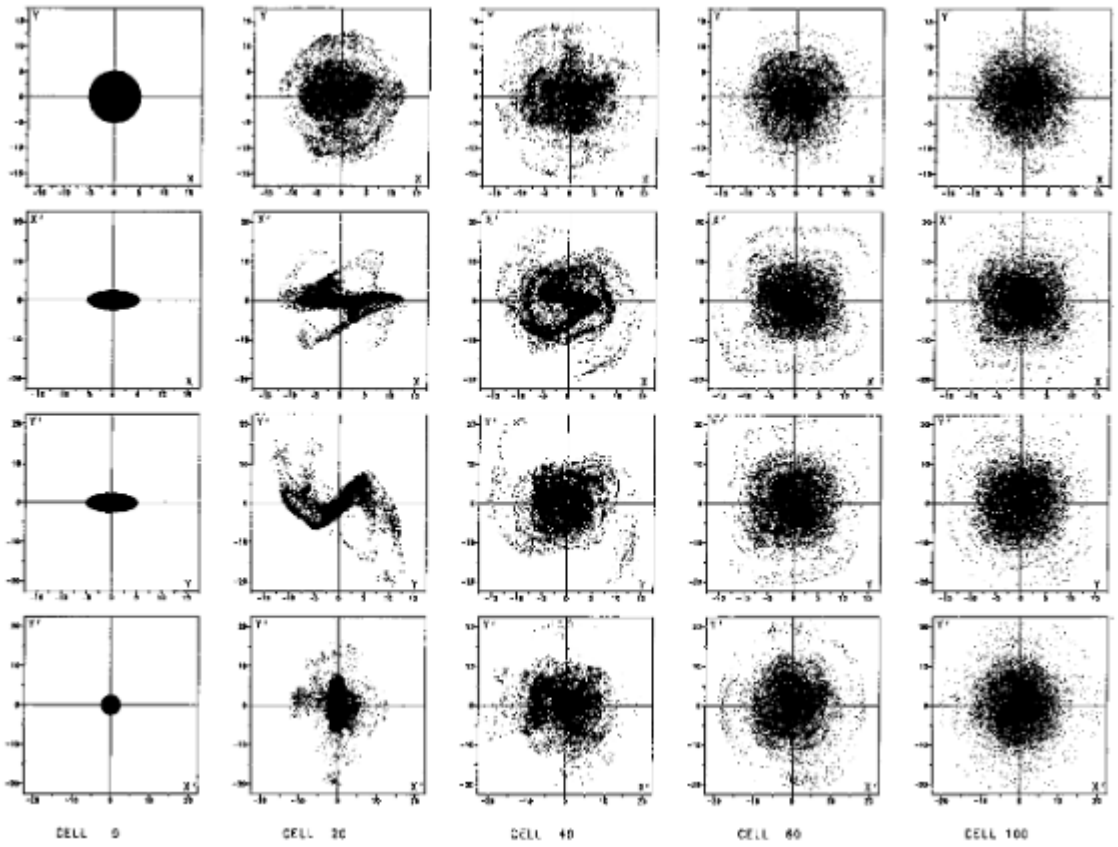

Figure 1.6: An initially uniform beam distribution in phase space evolving in a quadrupole focusing channel with space charge [4]. The beam undergoes filamentation, develops an "S" shape and diluting the entire phase space causing the emittance to increase.

non-relativistically and therefore beam evolves rapidly due to its low magnetic rigidity and can experience tail and halo growth caused by space charge and non-linear forces. Listed below is a subset of the diagnostic devices used in front ends.

1.4.1 Beam position monitoring

One of the most common devices in hadron accelerators are Beam Position Monitors (BPMs). Measuring the beam position is important to verify the beam optics and also ensure the beam is near the center of the beam pipe to avoid losses.

BPMs in hadron accelerators commonly rely on capacitive pickups that couple to the electric field generated by the beam. These have four pickups located at the top, bottom, left, and right sides of the beam pipe. To measure the beam position, the image charge generated by the electric field from the beam on each of the pickups is measured. The radial electric field in cylindrical coordinates (r, ϕ, z) from a pencil beam located at (r_0, ϕ_0) in a pipe of radius R_p traveling at $v = \beta_r c$ and charge modulated with frequency ω is given by [20]

$$E_r(r,\phi,z) = D_\omega \cos\left(\omega\left[t + \frac{z_0 - z}{\beta_r c}\right]\right) \sum_{n=0} \frac{g I_n(g r_0)}{\epsilon_0 N \pi I_n(g R_p)} \cos(n[\phi - \phi_0]) \times \left[I_n'(gr) K_n(g R_p) - I_n(g R_p) K_n'(gr)\right] \tag{1.43}$$

where I_n and K_n are the modified Bessel functions of the first and second kind [21], primes denote derivatives with respect to the argument, and

$$N = \begin{cases} 2, & \text{n=0} \\ 1, & \text{else} \end{cases} \tag{1.44}$$

is a harmonic factor and

$$g = \frac{\omega}{\gamma_r \beta_r c} \tag{1.45}$$

acts as a transverse propagation constant. g is proportional to the ratio of the photon and beam momenta and g is small when the beam momentum is large and g is large when the beam momentum is small. The image charge at a point on the beam pipe is

$$\sigma(\phi, z) = -D_\omega \cos\left(\omega\left[t + \frac{z_0 - z}{\beta_r c}\right]\right) \sum_{n=0} \frac{I_n(gr_0)}{N\pi R_p I_n(gR_p)} \cos(n[\phi - \phi_0]) \tag{1.46}$$

The beam position can be determined by are measuring the image charge at two locations on opposite sides of the beam pipe at the azimuthal locations $\phi = \phi_m$ and $\phi = \phi_m + \pi$. The difference of these two signals Δ divided by the sum Σ is

$$\frac{\Delta}{\Sigma} = \frac{\sum_n \frac{I_n(gr_0)}{NI_n(gR_p)} \left(\cos(n[\phi_m - \phi_0]) - \cos(n[\phi_m + \pi - \phi_0])\right)}{\sum_n \frac{I_n(gr_0)}{NI_n(gR_p)} \left(\cos(n[\phi_m - \phi_0]) + \cos(n[\phi_m + \pi - \phi_0])\right)}. \tag{1.47}$$

This can be approximated by taking terms up to n=3

$$\frac{\Delta}{\Sigma} \approx \frac{2\frac{I_1(gr_0)}{I_1(gR_p)} \cos(\phi_0 - \phi_m) + 2\frac{I_3(gr_0)}{I_3(gR_p)} \cos(3(\phi_0 - \phi_m))}{\frac{I_0(gr_0)}{I_0(gR_p)} + 2\frac{I_2(gr_0)}{I_2(gR_p)} \cos(2(\phi_0 - \phi_m))} \tag{1.48}$$

then expanding in r_0 up to 5^{th} order using Mathematica [22]

$$\begin{aligned}\frac{\Delta}{\Sigma} \approx & \frac{I_0(gR_p)}{I_1(gR_p)}\cos(\phi_m-\phi_0)r_0+ \\ & \left(\frac{I_0(gR_p)}{24I_3(gR_p)}\cos(3(\phi_m-\phi_0))-\frac{I_0^2(gR_p)}{4I_1(gR_p)I_2(gR_p)}\cos(\phi_m-\phi_0)\cos(2(\phi_m-\phi_0))-\right. \\ & \left.\frac{I_0(gR_p)}{8I_1(gR_p)}\cos(\phi_m-\phi_0)\right)r_0^3+ \\ & \left(\frac{I_0(gR_p)}{48I_1(gR_p)}\cos(\phi_m-\phi_0)+\frac{7I_0^2(gR_p)}{96I_1(gR_p)I_2(gR_p)}\cos(\phi_m-\phi_0)\cos(2(\phi_m-\phi_0))-\right. \\ & \frac{I_0^3(gR_p)}{16I_1(gR_p)I_2(gR_p)}\cos(\phi_m-\phi_0)\cos^2(2(\phi_m-\phi_0))- \\ & \frac{I_0^2(gR_p)}{96I_2(gR_p)I_3(gR_p)}\cos(2(\phi_m-\phi_0))\cos(3(\phi_m-\phi_0))- \\ & \left.\frac{I_0(gR_p)}{128I_3(gR_p)}\cos(3(\phi_m-\phi_0))\right)r_0^5.\end{aligned} \tag{1.49}$$

The position of the beam can then be estimated by taking only the term linear in r_0

$$\frac{\Delta}{\Sigma} \approx \frac{gI_0(gR_p)}{I_1(gR_p)}r_0\cos(\phi_m-\phi_0) \tag{1.50}$$

$$\frac{\Delta}{\Sigma} \approx \frac{gI_0(gR_p)}{I_1(gR_p)}\left[x_0\cos(\phi_m)+y_0\sin(\phi_m)\right] \tag{1.51}$$

where $x_0 = r_0\cos(\phi_0)$ and $y_0 = r_0\cos(\phi_0)$ is the location of the beam centroid in Cartesian coordinates. Therefore the position of the beam can be determined using the Δ/Σ signal from a horizontal pair of pickups to measure x_0 and a vertical pair to measure y_0. For large enough gR_p the result is dependent on gR_p, i.e. the measured frequency and beam momentum, and therefore multiple calibrations must be used to correctly measure the beam position as the beam accelerates and β increases. If $gR_p \ll 1$, generally corresponding to

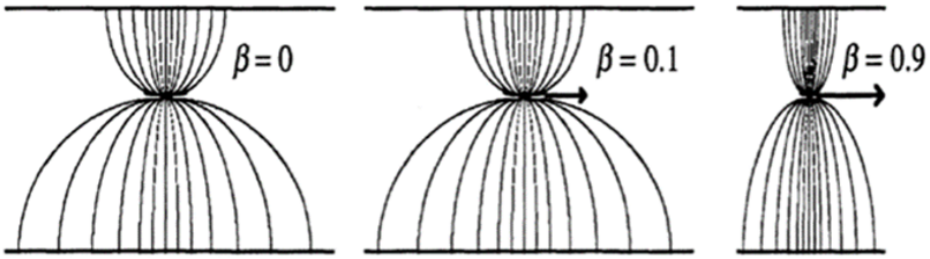

Figure 1.7: As the beam accelerates the electric field is compressed into to the plane perpendicular to the velocity resulting in the same field profile on opposite sides of the beam pipe [5].

relativistic beams $\gamma_r \beta_r \gg 1$, then Eq. 1.51 becomes momentum and frequency independent

$$\frac{\Delta}{\Sigma} \approx \frac{2}{R_p} \left[x_0 \cos(\phi_m) + y_0 \sin(\phi_m) \right]. \tag{1.52}$$

The dependence on gR_p for large gR_p is due to the profile of the electric field on the pipe wall generated by a non-relativistic beam extending beyond the length of the bunch and the fields profiles are different on each pickup and vary with beam position. As the beam is accelerated and increases in energy, relativistic effects 'pancake' the field distribution into the plane perpendicular to the beam velocity (see Fig. 1.7) and the longitudinal profile of the fields becomes similar to the beam profile. At these higher energies, varying the beam position causes little variation in the field profiles on the wall and only changes the amplitude resulting in no frequency dependence in position measurements [23].

The low β_r, high gR_p effects are most important in the front ends of hadron machines where the beam is traveling non-relativistically [24]. For example, at FRIB, with f=161 MHz and $R_p \approx$20 mm, these effects will cause a 2% error in the measured position at $\beta \approx 0.18$ [6]. However, in the MEBT the beam has velocity β_r=0.033 corresponding to gR_p=2.4 and non-relativistic effects must be accounted for.

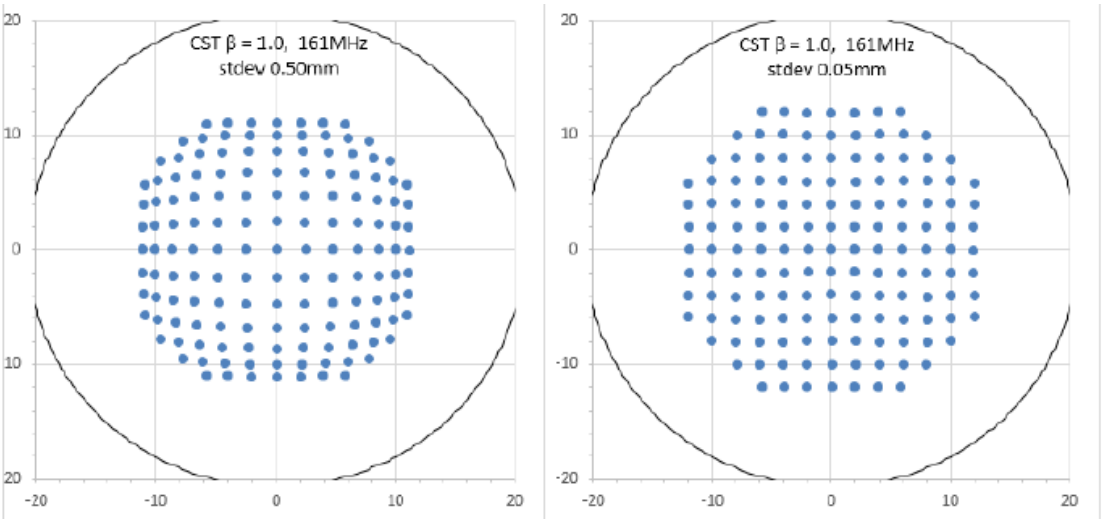

Figure 1.8: Simulation results for the calculated beam position using the linear Δ/Σ (left) and a higher order polynomial correction (right) [6].

The linear response of Eqs. 1.51 and 1.52 hold for small beam offsets from the center of the BPM relative to R_p. When the beam is further away, the Δ/Σ signals vary non-linearly with beam position (see Fig. 1.8). These non-linearities are mapped on a test stand by stringing a straight wire through the BPM and sending a tone down the wire and recording the response of the BPM pickups. This is repeated for different locations of the wire to map the response for different beam positions. To determine the position, the wire location is related to the pickup signals using a higher order polynomial, e.g. the FRIB BPMs use a fifth order polynomial [6].

The shape of the BPM pickups affect the measured signals and must be taken into account. The pickups have some finite size causing their measured signal to be the integrated image charge over the button geometry

$$\sigma_{\text{pickup}}(\omega) = \int_{\text{button}} \sigma \, \mathrm{d}A_{\text{but}}. \tag{1.53}$$

Common BPM pickup geometries are round button pickups [6], rectangular split-plate pick-

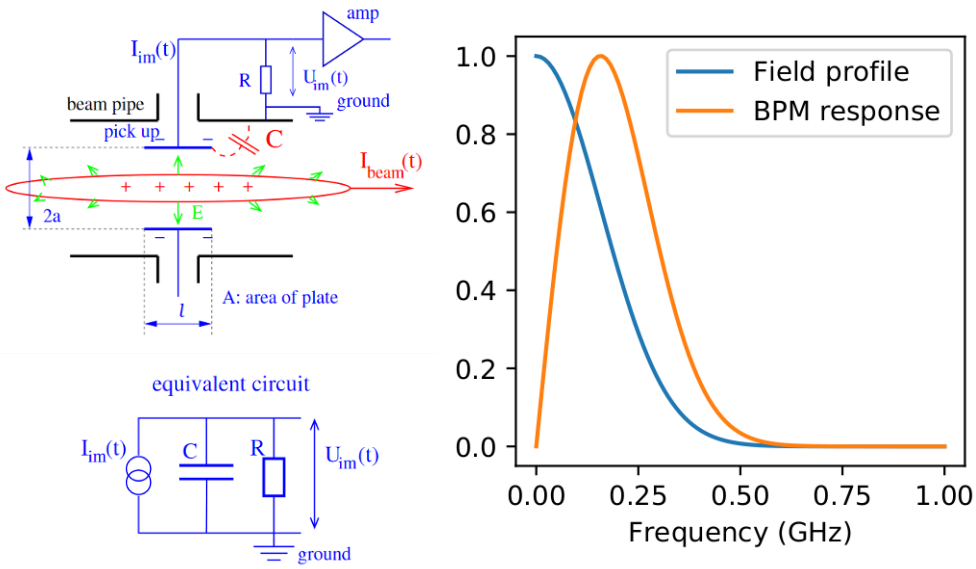

Figure 1.9: A sketch of a capacative BPM and its equivalent circuit is shown on the left [7]. Due to the capacitance to ground, BPMs suppress the low frequency components of the measured signals (right, $R = 50\ \Omega$, C=3 pF).

ups [25], and stripline pickups [26]

The measured signals also are affected by the impedance of the BPM pickup. The BPM pickups are capacitive and connected to a 50 Ω cable (see Fig. 1.9). This system acts as a high pass filter with cut off frequency $\omega_c = 1/RC$ where R is the resistance and C is the capacitance of the pickup to ground. The measured voltage from a capacitive BPM pickup is [7]

$$V_{\text{meas}}(\omega) \propto \frac{\omega/\omega_c}{\sqrt{1+(\omega/\omega_c)^2}}\sigma_{\text{pickup}}(\omega). \tag{1.54}$$

This suppresses the low frequency components of the measured signal causes the measured signals to appear like the derivative of the electric field at the wall. For FRIB C=3.3 pF and ω_c=6.06 GHz [6].

The BPM signals are, unsurprisingly, affected by noise and one main concerns is thermal noise. When measuring the voltage across a resistor R at temperature T, the rms voltage

from thermal noise is related to the measured bandwidth Δf [27]

$$V_{T,rms} = \sqrt{4k_B T R \Delta f} \tag{1.55}$$

where k_B is the Boltzmann constant. While the BPM pickups have a broadband response to the beam, typically narrowband filtering is use to reduce the thermal noise. The narrowband filtering selects a single harmonic of the bunch repetition rate. This is often the first harmonic because it has the highest amplitude. However, the second harmonic is also be used to prevent the signals from being affected by the RF accelerating elements operating at the principle harmonic. Because BPMs rely on measuring the frequency content of a bunch train, they can be used the the MEBT but not the LEBT. In the LEBT profile monitors can be used to determine the beam position.

1.4.2 Profile measurements

Like position monitoring, measuring the transverse profiles in real space of the beam is used to verify the beamline optics. In addition, these measurements can be used to characterize the beam quality and ensure the beam is small enough to avoid losses. Due to the low energy in front ends, devices that intercept the beam are commonly used measure the beam profiles in this region. For higher energy beams, interceptive diagnostics are less commonly used and alternative methods are employed such as gas jets [28].

One common profile monitor is a scintillator screen [29]. These are inserted into the beamline and when the beam strikes the screen, energy is deposited that excited the scintillator molecules causing them to produce light which is recorded with a camera. The more energy that is deposited the more light that is produced so the areas with higher beam in-

tensity will be brighter. Assuming the intensity of the light is linear with the beam intensity, the recorded image is a direct replication of the 2D transverse distribution.

Scintillators must be chosen such that their response is linear within the range of expected beam intensities to avoid saturation. An additional consideration is the scintillating properties will decay with use. If the beam is always striking the same spot on the scintillator, the response at the high intensity region will decay faster which will eventually distort the measured distributions.

Another commonly used device is a wire profile monitor. These devices insert a thin conducting wire into the beam and when the particles strike it, they excite a current in the wire that can be recorded. The current is proportional to the total intensity intercepted by the wire. By stepping the wire through the beam, the profile in one direction can be mapped [5]. To reduce noise, the measurements at each location can be averaged in time and background measurements without the beam can be taken. Wire profile monitors typically have three wires to measure the x and y profiles as well as one at 45° to measure $x - y$ coupling.

The resolution of these scanners is determined by step size and the size of the wire. However, arbitrarily thin wires cannot be used because the wire must be able to withstand the beam intensity that it intercepts. If the wire is too thin and overheats it can be deformed or break. An additional consideration is when the beam strikes the wire, the wire can emit secondary electrons. This would affect the measured current as charge is leaving the wire. To prevent this the wires are typically held at voltage. Further more, if multiple wires are used, then crosstalk between the wires will limit the ability to measure the low intensity portions of the beam.

1.4.3 Phase space distribution measurements

The distribution of the beam in $u - u'$ phase space is often measured in front ends with slit scanners. These devices have a thin slit that is inserted into the beamline to only allow a small slice of the beam at a specific location to pass. The particles in the passed beamlet will have some range of angles which will cause the particles to diverge. For example a particle with $u' = 10$ mrad will drift 1 mm transversely over 100 mm while a particle with $u' = 5$ mm will only drift 0.5 mm. Therefore, if the transverse profile of the passed beamlet is measured downstream, the u' profile of the particles at the location of the slit can be reconstructed. The entire $u - u'$ phase space distribution can be measured by stepping the slit through the beam and recording the transverse profile of the passed beamlet at each step. These measurements of the phase space distribution are referred to here as phase portraits.

There are as many forms of these scanners as there are types of profile monitors, e.g. pepperpots [30], slit-slit scanners [31] and slit-wire harp scanners [32]. The phase portraits presented in chapter 2 were taken with an Allison-type scanner [33] in the PIP2IT MEBT. Allison scanners consist of a rigid box with a thin slit on either end and a variable electric dipole between the slits (Fig. 1.10). The beam is intercepted by the front plate and particles can only pass through the first slit to select narrow position range. The passed beamlet is deflected by the dipole field until it strikes rear wall. If the particles have the correct initial transverse angle then the deflection will cause the particles to pass through the second slit and into a Faraday cup to measure the passed current. For an Allison scanner of length ℓ and a beam of mass m traveling at $v = \beta_r c \ll c$ the passed angle x'_0 for a given voltage V is

$$x'_0(V) = \frac{qV\ell}{2m\beta_r^2 c^2}. \tag{1.56}$$

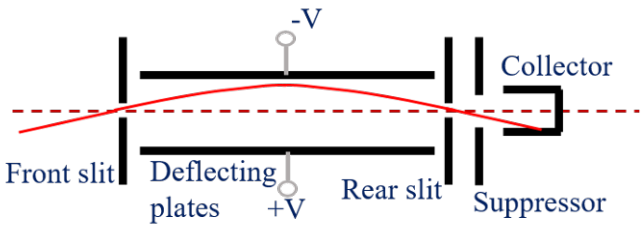

Figure 1.10: Simplified schematic of an Allison scanner. The red line shows the trajectory of particles through the device.

The 2D transverse phase space can therefore be measured by stepping the whole box through the beam so the front slit can take slices at different positions and at each position the electric dipole strength is swept to scan a range of angles. At each position-dipole setting the current on the Faraday cup is measured to determine the intensity of the beam in the small phase space area that passed through the scanner.

It is important to handle the background noise when analyzing the measured phase portraits. There are many methods for accounting for the noise. A simple and inelegant method is to set a cut threshold in intensity that is high enough to remove all the noise [34]. This level can be set by varying the cut level and calculating the rms emittance for each cut level and finding a knee point where the noise starts to affect the measured values. This will inevitably remove a portion of the beam signal, but if it is small then the impact on the rms parameters will be minimal. Another method is to calculate the rms emittance over an ellipse in phase space with the same Twiss parameters as the beam core [35]. If this ellipse is too large noise will effect the calculated rms emittance. Therefore the noise can be excluded by varying the size of this ellipse find a range where the emittance is stable. Ref. [36] sets the cut threshold to a negative value to include all measured pixels, and relies on perfect cancellation of the random noise outside of the beam when calculating the rms parameters.

1.4.4 Beam tail measurements

It is generally agreed that the beam tails have densities in the range of 10^{-1} to 10^{-4} of the peak density with the halo having even lower density [37] and typically have a different distribution from the core. However, there are a variety of definitions of tails are used based on the needs of different accelerators. In addition, beam tails can be challenging to quantify because the beam rotates in phase space and the variations from beam dynamics must be isolated from variations caused by tail growth. This is particularly challenging when measuring the tails with profile monitors.

Even when measuring the distribution of the beam in phase space, it can be challenging to quantify the beam tails. A typically practice is to only calculate the rms parameters of the phase portrait and 'qualify' the beam tails visually.

Chapter 2

Analysis of Phase Portraits using Action-Phase Coordinates

A method that has been used to analyze tails in simulations is to convert the particle locations from $u-u'$ coordinates to normalized coordinates $w-\dot{w}$ [38]. In this coordinate system there is a well defined notion of radius because w and $\dot{w}$ have the same units. The tail growth can then be quantified by the particle density as a function of radius.

This idea can be further developed by using $J-\phi$ coordinates instead of $w-\dot{w}$. This gives a better physical interpretation as the 'radius' of a particle is its action. The intensity distribution as a function of J will be constant under linear forces and therefore it can be used to study tail growth due to non-linear effects and characterize the beam quality. In addition, this analysis can be applied to beamline measurements taken in $x-x'$ coordinates from a phase space scanner by determining the Twiss parameters of the beam and calculated J and ϕ of each pixel using Eqs. 1.28 and 1.29. An example of a phase portrait measured with an Allison scanner in the PIP2IT MEBT is shown in Fig 2.1 in $x-x'$ coordinates and with each pixel converted into $J-\phi$ coordinates. The phase portrait in $J-\phi$ coordinates should be stable modulo shifts ϕ caused by changes to the optics.

There measurements presented in this chapter were taken with an Allison scanner in the PIP2IT MEBT. The PIP2IT MEBT was assembled and beam measurements were performed

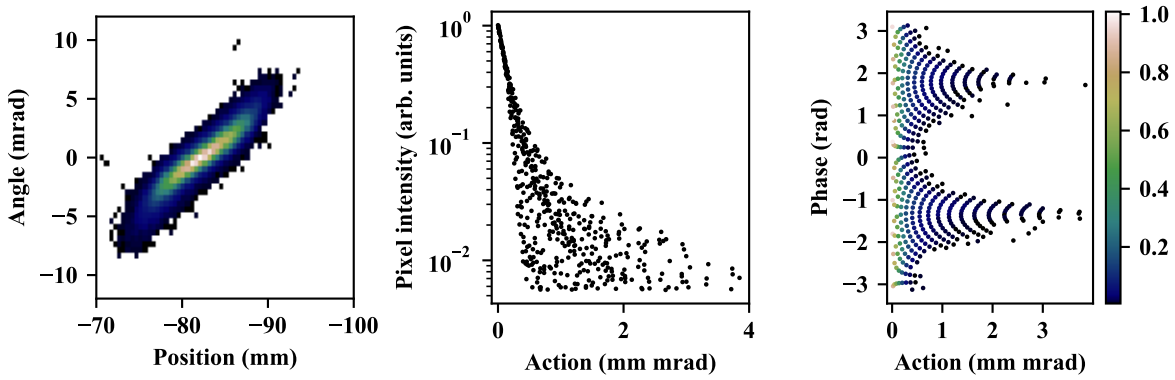

Figure 2.1: Measured phase portrait in $x - x'$ coordinates and $J - \phi$ coordinates taken at location 1.

in several stages between 2016 - 2018. Its initial configuration is shown in Fig. 2.2 and configuration at the end of the 2018 run is shown in Fig. 2.3. The primary beam parameters in the MEBT are summarized in Table 2.2. The Allison scanner was used in three locations and was moved at different phases of the MEBT construction:

1. Location 1, downstream of the second quadrupole doublet as shown in Fig. 2.2, in the horizontal position

2. Location 2, in the middle of the beamline, in the vertical position

3. Location3, toward the end of the beamline downstream of all focusing optics, as shown in Fig. 2.3, in the vertical position.

Most of the measurements presented here were taken at the first location of the Allison scanner (Fig. 2.2). Results from other two locations are explicitly noted.

2.0.1 Allison scanner noise

Measurements take with the PIP2IT MEBT Allison scanner unfortunately had significant electronic noise compared to the measured signal intensities. For a typical scan of a 5 mA

Table 2.1: Parameters of the PIP2IT MEBT Allison scanner

Parameter	Value	Unit
Slit size	0.2	mm
Slit separation	320	mm
Plate voltage	±1000	V
Plate length	300	mm
Plate separation	5.6	mm
Maximum measurable angle at 2.1 MeV	±12	mrad

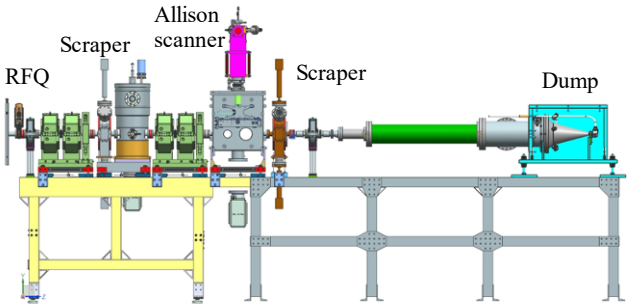

Figure 2.2: Initial PIP2IT MEBT configuration. The Allison scanner is in location 1 and measures the transverse phase space in the horizontal plane

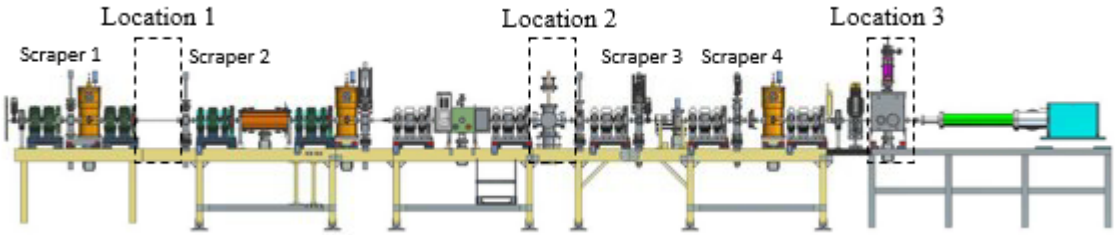

Figure 2.3: Final configuration of the PIP2IT MEBT with the Allison scanner in location 3 and oriented to measure the transverse phase space in the vertical plane. Transverse focusing is provided by quadrupoles with two doublets and seven triplets.

Table 2.2: PIP2IT MEBT beam parameters

Parameter	Value	Unit
Beam energy	2.1	MeV
Macro-pulse repetition rate	1-20	Hz
Macro-pulse length	0.005-25	ms
Bunch repetition rate	162.5	MHz
Pulse beam current	Up to 10	mA
Transverse emittance, rms norm.	≤ 0.23	mm mrad
Longitudinal emittance, rms norm.	≤ 0.34	mm mrad

beam, its rms noise is 0.2%-0.3% of the maximum amplitude for nominal operation. This limited the dynamic range of the device to ∼2 orders of magnitude. The source of the noise was investigated but no remedy was found.

In addition, significant jitter of the beam centroid was measured with the BPMs in the MEBT, but the source of the jitter could not be located nor the jitter eliminated [39]. Spectral analysis of the BPM readings shows the jitter has frequencies up to ∼3 Hz with no dominant harmonics. Therefore, even individual angular scans are affected as it takes ∼1 s to sweep the voltage over the angle range while measuring at 20 Hz and approximately 5 minutes to complete a typical phase space measurement [40]. In the MEBT, the amplitude of the jitter varies along the beamline in accordance with the optics and reaching up to 0.2 mm rms in amplitude.

The source of centroid jitter was determined to be in the LEBT, but the exact source was not determined nor fixed. The motion can be rotated between the horizontal and vertical planes by changing the strength of a solenoid focusing magnet in the LEBT [41]. However, for the optimal performance of the RFQ, the LEBT solenoids need to be set such that the jitter was primarily in the vertical plane. This noticeably impacted the measurements taken at locations two and three. The majority of the results presented in the following sections use measurements taken in the first location of the Allison scanner where the scanner was oriented horizontally to reduce the effects of the jitter.

To estimate the effect of the jitter on the pixel amplitude, multiple phase portraits taken with the same focusing were used to estimate the rms scatter at each pixel σ_{I_i} [42]. At location one, σ_{I_i} was found to increase approximately linearly with the pixel amplitude I_i

(Fig. 2.4 left) with the linear fit

$$\sigma_{I_i} = 0.0067 + 0.024 I_i. \tag{2.1}$$

The intensities vary by 2-3% for pixels near the center of the beam and is dominated by electronic noise at low intensities. The error bars shown in results from measurements taken at location one follow Eq. 2.1.

For measurements taken at locations two and three, the jitter in the vertical plane significantly increases the variation in the pixel amplitude and follow the general trend (Fig. 2.4 right)

$$\sigma_i = \begin{cases} 0.01 + 0.3 I_i & \text{for } I_i < 0.9 \\ 0.28 & \text{for } I_i \geq 0.9 \end{cases} \tag{2.2}$$

This jitter has minimal effect on the measured rms parameters of the beam and causes an error of only $\sim$2% [40]. However, it confounds the detailed measurements of the distribution in phase space and beam tails using $J - \phi$ coordinates.

2.1 Beam description using $J - \phi$ coordinates

2.1.1 Core description

When the phase portraits measured in the MEBT were converted to action-phase coordinates, it was found that in the central portion of the beam, i.e. pixels at small actions, the pixel amplitude is mostly independent of the phase and decreases exponentially with action

$$I_{\text{gauss}} = I_0 e^{-J/\epsilon_c} = I_0 e^{-\frac{1}{2\epsilon_c}\left(\gamma x^2 + 2\alpha x x' + \beta x'^2\right)} \tag{2.3}$$

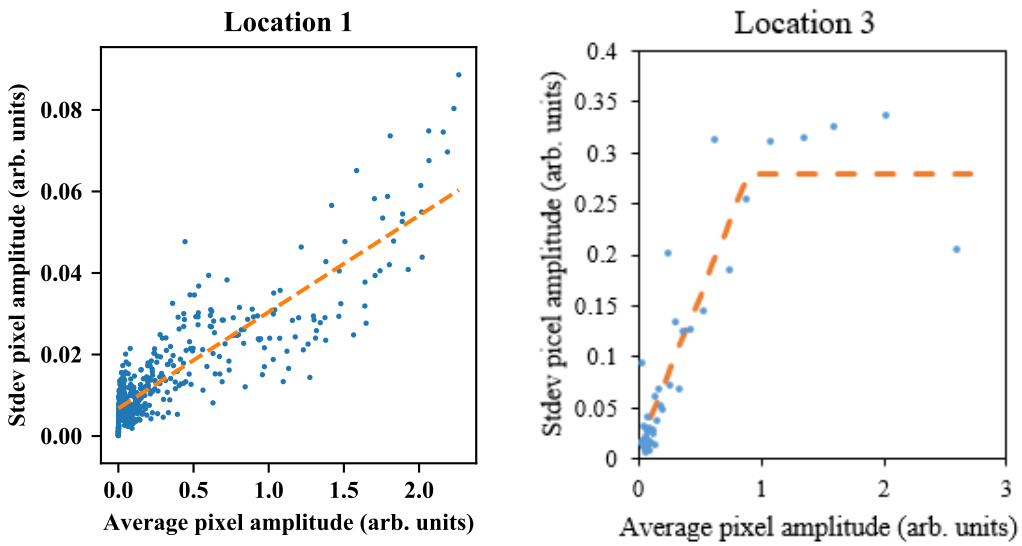

Figure 2.4: The rms scatter of the pixel amplitudes plotted as a function of the average amplitudes (blue) phase portraits measured at location one (left) and location three (right). The orange lines show the fits from Eqs.2.1 and 2.2.

which describes a Gaussian distribution in $x - x'$ coordinates with constant emittance ϵ_c. On semi-logarithmic scale, Eq. 2.3 represents a straight-line with slope $-1/\epsilon_c$, ϵ_c is referred to here as the central slope. Since Eq. 2.3 describes a perfect Gaussian distribution, ϵ_c is a measure of how broad the core distribution is and can be interpreted as the rms emittance of the beam if the Gaussian core was extended and the tails removed.

2.1.2 Discussion on the beam distribution

The choice of the describing the core as Gaussian was not immediately obvious. One consideration was, in the PIP2IT LEBT, the transverse beam distribution was measured to not be Gaussian [43]. Instead it was uniform-Gaussian (UG) caused by the beam being initially spatially limited by the ion source extraction aperture resulting in the beam distribution coming for the ion source being uniform in position and Gaussian in angle. The UG distribution, projected onto one plane in action-phase coordinates is

$$I_{UG}(J,\phi) = I_0\sqrt{1-\frac{J\cos^2(\phi)}{2\epsilon_{UG}}}e^{-\frac{J\sin^2(\phi)}{\epsilon_{UG}}} \times H\left(1-\frac{J\cos^2(\phi)}{2\epsilon_{UG}}\right) \tag{2.4}$$

where I_0 is the peak intensity, ϵ_{UG} is the rms emittance, and H is the Heaviside function

$$H(x) = \begin{cases} 0 \text{ if } x < 0 \\ \\ 1 \text{ if } x \geq 0 \end{cases}. \tag{2.5}$$

In addition, according to Refs. [18, 44], after experiencing multiple betatron oscillations in a periodic structure, the transverse distribution is expected to relax towards an equilibrium distribution. For a space charge dominated beam the equilibrium distribution is uniform and for an emittance dominated beam it is a Maxwell-Boltzmann distribution in action which corresponds to Eq. (2.3). The beam arrives to the MEBT after passing ∼12 betatron periods in the RFQ and it was not obvious if this was sufficient for the relaxation. Also, for nominal 5 mA operation the perveance in the MEBT is $Q \sim 10^{-6}$ and the rms radius is $r \approx 3$ mm and geometric emittance is $\epsilon \approx 3$ mm mrad. Putting these values into the envelope equation (Eq. 1.42), we find the strength of the space charge and emittance terms are on the same order, $Q/r_b \approx \epsilon^2/r_b^3 \sim 10^{-4}$, therefore the beam was not expected to be space charge or emittance dominated.

To determine the distribution of the beam core at low action, the measured distribution was fit to Eq. 2.3 and Eq. 2.4. In addition, the phase portrait was fit to two other models commonly used for approximating the beam distribution: the Kapchinskiy-Vladimirskiy

(KV) and waterbag (WB) distributions. In action they are

$$I_{KV}(J,\phi) = I_0 \cdot H\left(1 - \frac{J}{2\epsilon_{KV}}\right) \tag{2.6}$$

$$I_{WB}(J,\phi) = I_0 \left(1 - \frac{J}{3\epsilon_{WB}}\right) H\left(1 - \frac{J}{3\epsilon_{WB}}\right) \tag{2.7}$$

where ϵ_{KV} and ϵ_{WB} are the corresponding emittances.

In Fig. 2.5, the high-amplitude pixels within the normalized action $J < 0.15$ mm mrad (containing 60% of the measured beam), are plotted together with fits of the idealized distributions Eq. 2.3, Eq. 2.4, Eq. 2.6, and Eq. 2.7. The Gaussian distribution Eq. 2.3 is the best fit with reduced $\chi^2 = 2.07$. For a waterbag distribution, the reduced $\chi^2 = 6.55$ (χ^2 normalized to the degrees of freedom), however, this model abruptly deviates from the measured distribution outside of the fitting region. The UG and KV distributions poorly fit the data with the reduced χ^2 of 47 and 687 respectively.

The large value of χ^2 for the Gaussian fit indicates that Eq. 2.3 does not fully characterize the distribution. Moreover, the χ^2 value grows quickly when including in the fit additional pixels with larger action. The growth is caused primarily by appearance at large J of a phase dependence of the pixel amplitudes, which is discussed below.

2.1.2.1 Central parameters

The initial attempts to compare the measured data with Eq. 2.3 showed a relatively large scatter of pixel intensities for any given action, even at low actions (Fig. 2.6, blue). This was caused by the choice of Twiss parameters used to define the action which can significantly affect the distribution in $J - \phi$ coordinates. Intially, the Twiss parameters used were the rms parameters of the entire beam (referred here as the rms Twiss parameters). This choice

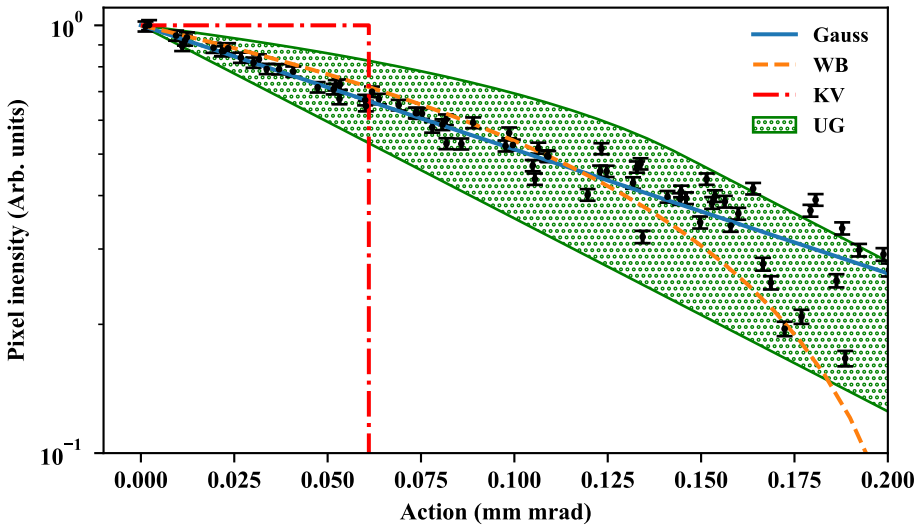

Figure 2.5: Comparison of the measured distribution in action in the beam core (black) with several ideal distributions: Gaussian, KV, UG, and WB. Note that the UG distribution is phase-dependent, and, therefore, pixel intensities vary for a given action and is represented here by the area shaded in green.

of Twiss parameters results in a large scatter even for particles with low action because it includes the non-Gaussian beam tails which skew the rms description of the beam away core distribution.

Alternatively, the action can be defined using pixels in the 'central' portion of the beam. The central portion was found by removing the lower intensity pixels of the beam then fitting Eq. 2.13 to determine the 'central' Twiss parameters and central slope. The fraction removed was scanned from 30-60% of the total intensity in 1% steps. Generally, the central slope increases at large and small cuts (Fig. 2.7). The increase at small cuts is attributed to the tails affecting the fit and at large cuts poor statistics increases the central slope significantly when the number pixels is below ∼30. To avoid both of these effects, the central slope was fit to a cubic polynomial and the cut was chosen to be the point closest to the minimum of the fitted curve. If a cubic polynomial could not be fit, the cut was set to 50%.

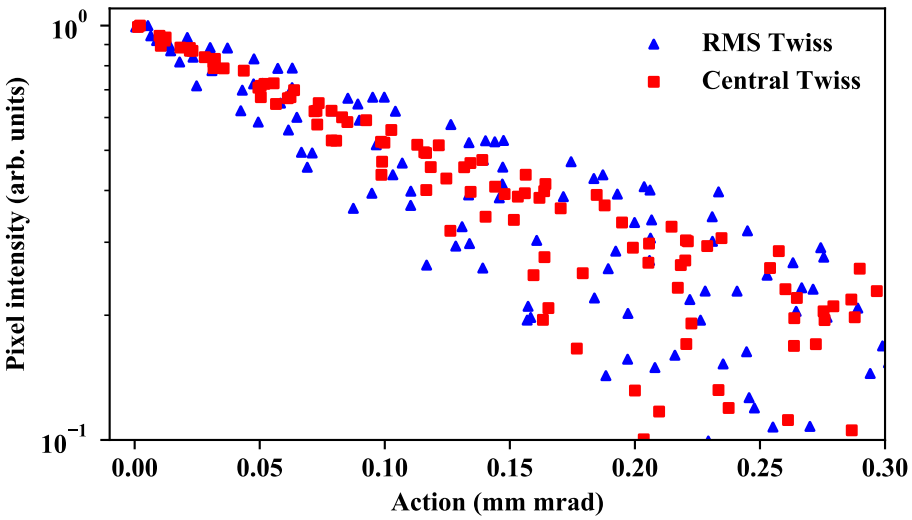

Figure 2.6: Action distribution using central Twiss parameters (red) and rms Twiss parameters (blue).

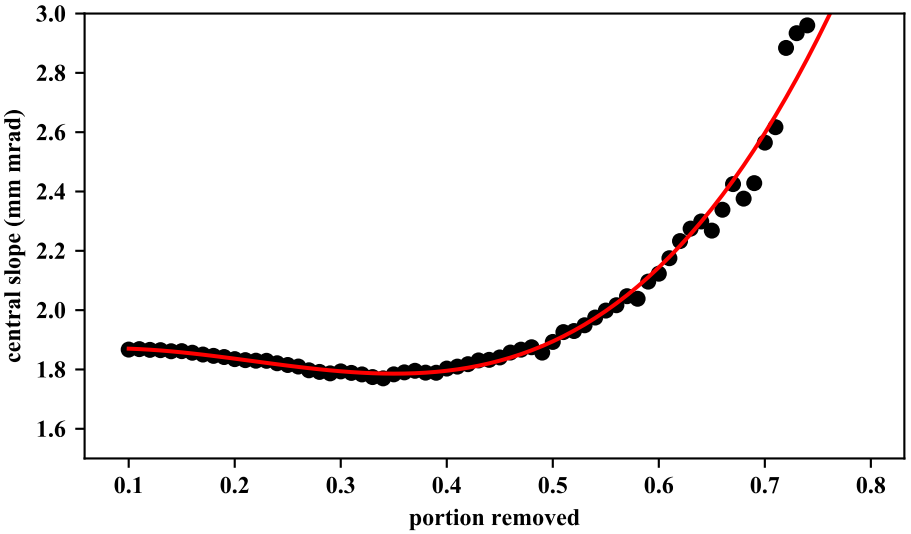

Figure 2.7: Central slope as a function of the portion of the beam removed. The curve is fit to a cubic polynomial to determine the minimum ϵ_c which is used to define the central paramters.

When the central Twiss parameters are used to define action and phase, the scatter in the beam's central region is reduced (Fig. 2.6, red). This is seen in the reduced χ^2 for fitting Eq. 2.3 to pixels with $J < 0.15$ mm mrad which is χ^2=64 when using the rms Twiss parameters and χ^2=2 when using the central Twiss parameters.

2.1.3 Allison scanner phase dependence

Equation 1.56 tacitly assumes the slits in the Allison scanner are infinitesimally small to determine the passed angle for a given voltage . In reality the slits have finite size $2d$. This causes the measured phase space area for every position-voltage setting to be a rhomboid (Fig. 2.8) with vertices at

$$\left(x_0 + d, x_0'\right) \tag{2.8}$$

$$\left(x_0 - d, x_0'\right) \tag{2.9}$$

$$\left(x_0 + d, x_0' - \frac{2d}{\ell}\right) \tag{2.10}$$

$$\left(x_0 - d, x_0' + \frac{2d}{\ell}\right). \tag{2.11}$$

This distorts the measured distribution from the true distribution. For example, if a pure 2D Gaussian is measured with an Allison scanner of slit to slit length ℓ and slits y_1 and y_2 extending from $-d$ to d the measured intensity distribution is given by integrating over both slits [45]

$$I_{\text{meas}}(x, x') = \frac{1}{4d^2}\int_{-d}^{d}\int_{-d}^{d} \exp\left(-\frac{1}{2\epsilon_c}\left[\gamma(x+y_1)^2 + 2\alpha(x+y_1)\left(x' + \frac{y_2 - y_1}{\ell}\right) + \beta\left(x' + \frac{y_2 - y_1}{\ell}\right)^2\right]\right) \mathrm{d}y_1 \mathrm{d}y_2. \tag{2.12}$$

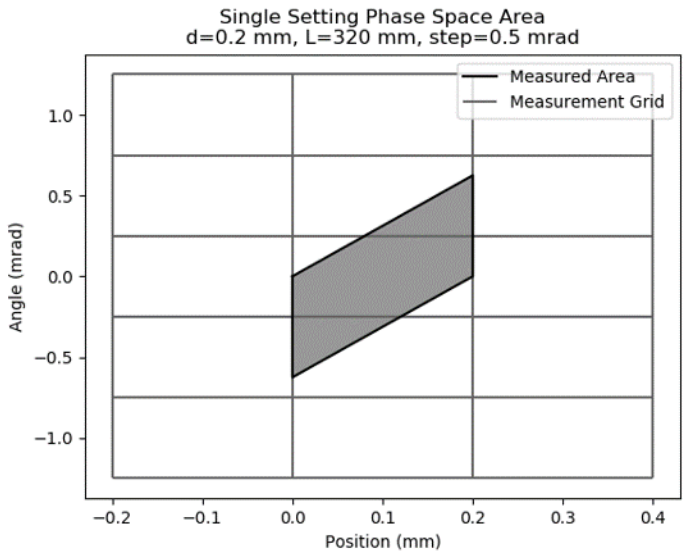

Figure 2.8: The shaded area represents the passed phase space area for a given position and voltage setting of an Allison scanner. The grid is the displayed pixel size.

The integrand can be expanded to second order in y_1 and y_2 and the resulting measured distribution up to order d^2 is

$$I_{\text{meas}}(x, x') = \exp\left(-\frac{1}{2\epsilon_c}\left[\gamma x^2 + 2\alpha x x' + \beta x'^2\right]\right) \left(1 + \frac{d^2}{6\epsilon_c^2}\left[\epsilon_c\left(\frac{2\alpha}{\ell} - \frac{2\beta}{\ell^2} - \gamma\right) + 2\left(\frac{\alpha x + \beta x'}{\ell}\right)^2 + \left(\alpha x' + \gamma x\right)^2 - 2\left(\frac{\alpha x + \beta x'}{\ell}\right)\left(\alpha x' + \gamma x\right)\right]\right). \quad (2.13)$$

At large J, when the parameters in Table 2.1 are used, this variation is approximately 2% of the measured intensity variation at a given action and was generally ignored. However, at low J, this distortion needs to be accounted for when defining action and the central parameters.

The effect of the slits can be seen by varying the strength of a quadrupole magnet directly upstream of the Allison scanner to change the Twiss parameters at the Allison scanner (Fig.

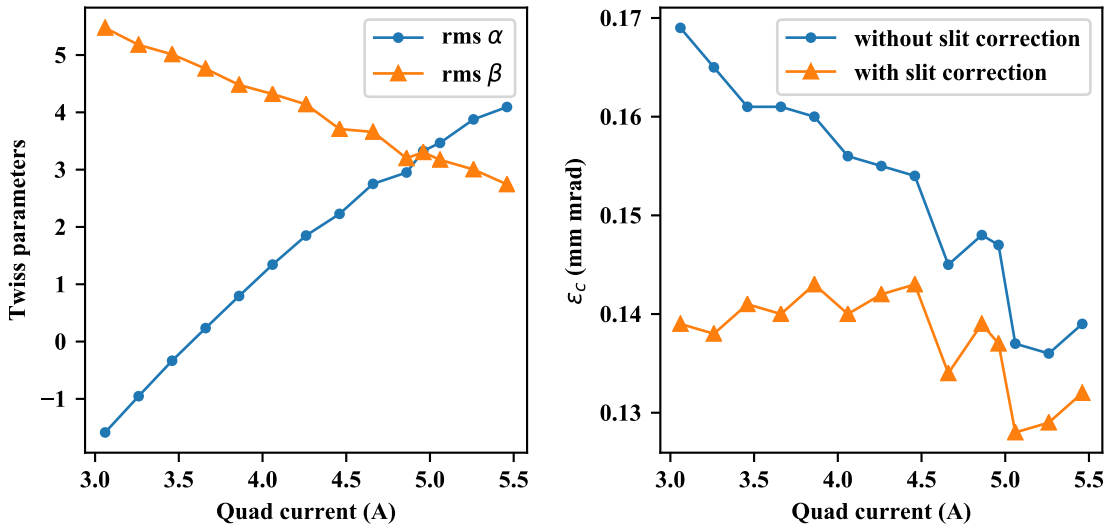

Figure 2.9: Left: Variation of the Twiss parameters with quadrupole current. Right: The central slope is constant when accounting for effects of the slit size.

2.9 left). Because this is changing a linear optic, the action distribution and ϵ_c should not change. If the slit effect is not accounted for and the central Twiss parameters are found by taking rms values over the high intensity pixels, then the central slope decreases linearly with the quadrupole excitation current (Fig. 2.9 right). If instead, the central slope and central Twiss parameters are found by fitting to Eq. 2.13 then ϵ_c is constant within $\pm 5\%$.

The recorded pixel intensity is also affected by the thickness of the slits [46]. This effect was neglected in these measurements because the effect is related to the angle of the measured particles which is comparatively small in the PIP2IT MEBT of ± 12 mrad. Most Allison scanners are used LEBTs where the lower energy results in a larger range of transverse angles of $\approx \pm 40$ mrad. The thickness of the slits for phase portraits recorded in the PIP2IT MEBT, the slit thickness is estimated to have at most a 2% affect on the pixel intensities.

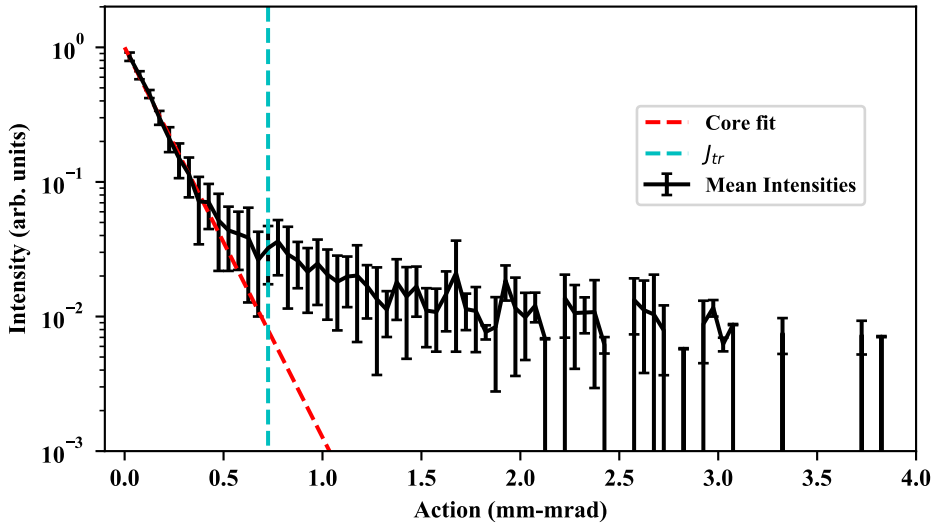

Figure 2.10: The intensities are binned in action to determine J_{tr} with Eq. 2.14 to separate the tails from the core. The error bars represent $\pm 3\sigma$.

2.1.4 Tail description

The distinction between the beam core and tails is defined by the transition action J_{tr} where the distribution deviates significantly from Gaussian Eq. 2.3. The transition action is found by firstly, determining the central parameters as outlined above and calculating the action and phase of each pixel. Then, all the pixels are sorted into normalized action bins J_i, typically 0.05 mm mrad in size, and the mean amplitude $I(J_i)$ and the standard deviation $\sigma_{Int}(J_i)$ of the amplitude in each action bin is calculated. The value of J_{tr} is chosen as the action of the bin where the mean amplitude deviates from the fit of Eq. 2.3 by more than three times the standard deviation of the mean (see Fig. 2.10)

$$I(J_{tr}) - I_0 e^{-J_{tr}/\epsilon_c} = 3\sigma_{Int}(J_{tr}). \tag{2.14}$$

All particles with action less than the transition action are defined to be in the core, and particles with larger action are in the tail. This gives a measure of the extent of the beam

core. The relative weight of the core can be quantified by the fraction of the total intensity in the beam core. The percentage of the beam intensity in the tails is typically 10-20% of the total intensity.

With these definitions, the transition action and the percent of the beam in the core are constant under linear forces and can be used as a metric for tail growth due to non-linear effects. In theory the maximum action can also be used. However, in practice, because the pixel with maximum action has intensity just above the noise floor, the maximum action is very noisy rendering it an unreliable quantitative measure.

At actions above J_{tr} the scatter of pixel intensities at a given action clearly deviates from the Gaussian core (Fig. 2.11 (b)). The dominant part of this scatter comes from strong phase dependence with the tail being split into two "branches" of similar intensities that are separated in phase by approximately π rad which are clearly evident when the data is plotted in $J - \phi$ coordinates (Fig. 2.11 (c)). The location in phase of the branches ϕ_b is defined by the phase of the second harmonic of this distribution. This is found by taking the Fourier transform of the pixel intensities as a function of phase for $J > 1.5J_{tr}$. Unfortunately, attempts to find an analytical description of the tail distribution did not succeed.

Hence, the measured beam distribution is described in action phase coordinates by seven parameters. The beam core is characterized by the central slope ϵ_c and central Twiss parameters α_c, β_c and is defined by pixels with action less than the transition action J_{tr}. All particles with action larger than the transition action are in the tails which are characterized by the phase of the branches ϕ_b, the maximum action $J_{\max}$, and the fraction of the particles in the core.

Note that because the beam centroid jitter is assumed to be from a single source and therefore predominately along a single line in phase space, it would add an asymmetry

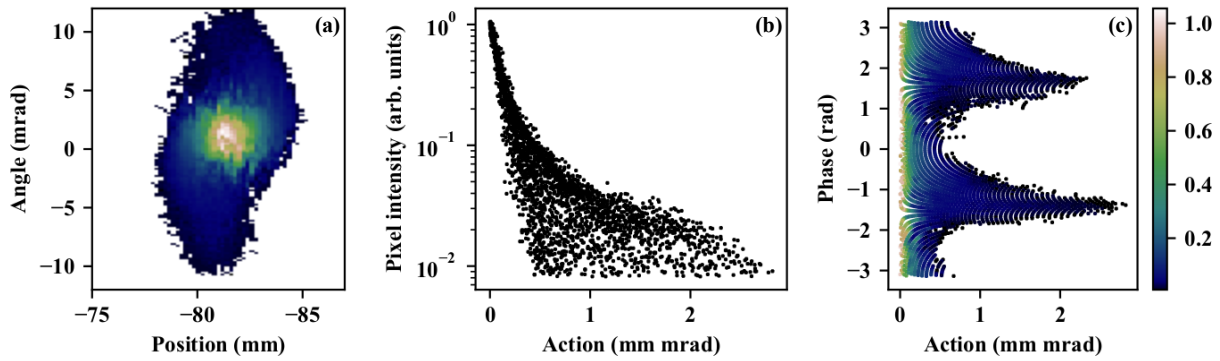

Figure 2.11: Phase portrait in position-angle phase space (a) and action-phase phase space (c). The beam splits into two branches separated in phase at large actions. The pixel amplitude versus action (b) shows deviation from the core distribution at large action.

for an initially symmetric distribution. To determine if the centroid jitter was responsible of the measured tails, this effect was modeled using a 2D Gaussian distribution with rms parameters equal to the typically measured central parameters and 0.2 mm rms position jitter added. The amplitudes of the zeroth and second harmonics were calculated for the given distribution by taking the Fourier transform with respect to phase in normalized action bins ΔJ=0.05 mm mrad wide. The resulting asymmetry, quantified by the amplitude of the second harmonic in phase calculated for pixels with actions $J > 0.5$ mm mrad, was found to be at least an order of magnitude lower than observed in measurements (Fig. 2.12) at large action. At lower action, in the core, the amplitude of the second harmonic is similar between the model and the measurements. This supports the claim that the core is Gaussian and the measured deviations are expected.

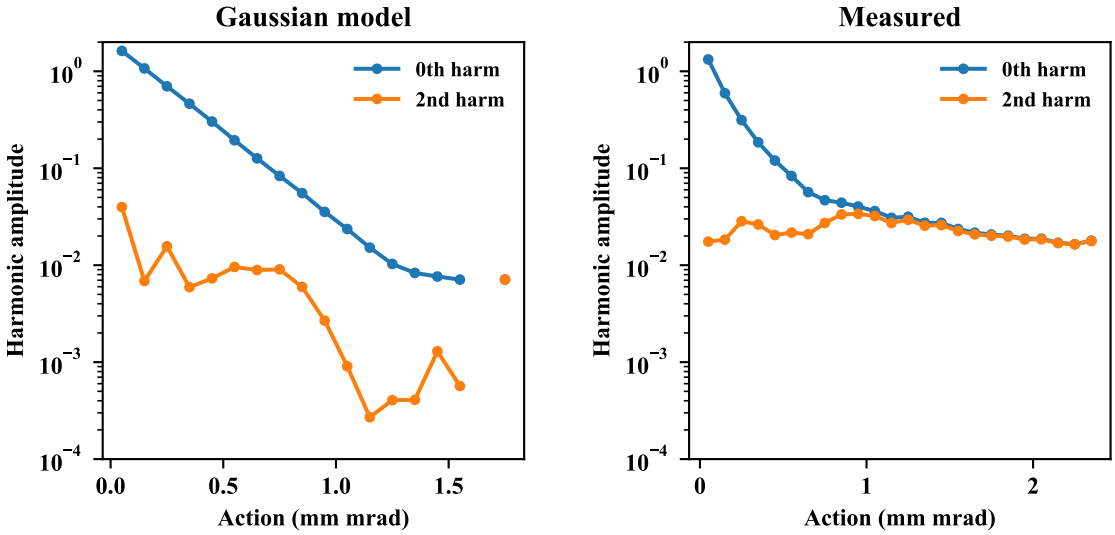

Figure 2.12: The amplitude of the 0^{th} harmonic of the pixel intensities as a function of ϕ for a Gaussian model is at least an order of magnitude larger than the amplitude of the 2^{nd} harmonic. For the measured beams, the ratio of the 0^{th} and 2^{nd} harmonic amplitudes is similar to the model at low J. However, the tails cause the 2^{nd} harmonic to dominate at large action.

2.2 Selected beam measurements

2.2.1 Background noise removal

After taking a scan, the scanner operating program removes the background and calculates the rms parameters of the phase portrait. The background removal is performed by setting to zero all pixels with intensity less than a user-defined threshold. By default, the threshold is set to 1% of the peak intensity [42], which was adequate to remove the noise for the nominal 5 mA beam. However, for low intensity beams this rejection threshold does not remove all noise, artificially increasing the reported emittance. And, for high intensity, the cut level can be too aggressive, removing otherwise observable beam tails. Therefore a more robust method is desired. Section 1.4.3 briefly describes alternative methods to account for the electronic noise, however, they are based around determining the rms parameters of the

distribution and are not overly concerned with including some noise or excluding a small portion of the beam signal.

In order study beam tails, we define the cut threshold based on the noise level and remove only the pixels that cannot be distinguished from the beam signal. This cut level is established by firstly, finding the area that is most likely to contain only noise. The measured portrait cell array is divided into four identical quadrants. In the quadrant with minimum total intensity, the 6×6 pixel square in the outermost corner of this rectangle is assumed to contain only signal from noise. This assumption was confirmed by taking measurements without the beam and comparing the signals in the corners to measurements with a beam present. The mean signal of this square is calculated and subtracted from each pixel over the entire portrait. The rms noise level σ_n in this square is calculated and the cut threshold T_c is set to

$$T_c = A_n \sigma_n. \tag{2.15}$$

To determine the coefficient A_n, let us consider a rectangular portrait containing $N_{pixels} = K \times M$ pixels for which amplitudes are determined by random Gaussian noise so that the probability density P_p of finding a pixel with a given intensity I_p is

$$\frac{dP_p}{dI_p} = \frac{1}{\sqrt{2\pi}\sigma_n} e^{-\frac{I_p^2}{2\sigma_n^2}}. \tag{2.16}$$

The probability P_0 of having a pixel with amplitude A_n times higher than the rms noise amplitude σ_n is

$$P_0 = 0.5\text{erfc}\left(\frac{A_n}{\sqrt{2}}\right) \tag{2.17}$$

where erfc is the standard error function [21]. The probability P_1 of having at least one pixel

above the threshold is

$$P_1 = 1 - (1 - P_0)^{N_{pixels}} \approx P_0 N_{pixels}. \tag{2.18}$$

This cleaning procedure can use P_1 to set a cut threshold that will remove all the noise. To achieve this we require $A_n \approx 3.3$. However, if after the cut single pixels remain above the threshold with all zero neighbors then these can be easily removed. Therefore, the cut level can be set lower and afterwards single pixels can be removed. For this, the cut threshold needs to be set high enough so no pairs of neighboring pixels (side-by-side or diagonally) will be above the cut threshold $A_n\sigma_n$. The total number of independent neighboring pairs N_{pairs} is

$$N_{pairs} = 4KM - 3(K + M) + 2, \tag{2.19}$$

which is approximated by

$$N_{pairs} \approx 4N_{pixels} \text{ for } K \gg 1,\ M \gg 1. \tag{2.20}$$

The probability P_2 that two neighboring pixels are both above the threshold is

$$P_2 = 1 - (1 - P_0^2)^{N_{pairs}} \approx 4P_0^2 N_{pixels}. \tag{2.21}$$

In practice, it was accepted that one in ~ 100 portraits may contain an un-removed noise pair ($P_2 = 0.01$). The value of P_0 is calculated from Eq. 2.20 and 2.21 and then the threshold is determined by inverting Eq. 2.17. For a typical number of pixels of 3000, the multiplier in Eq. 2.15 is $A_n \approx 2.2$. For the nominal beam in PIP2IT, the cut threshold calculated with

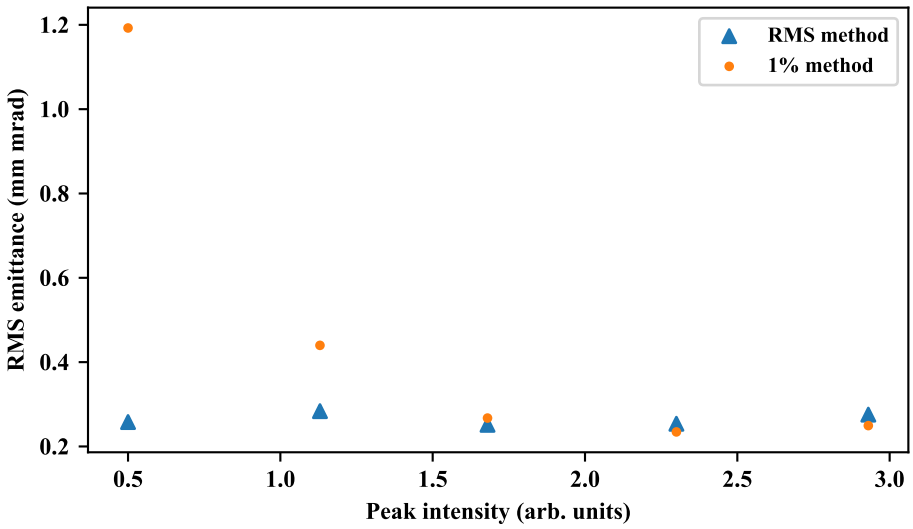

Figure 2.13: Vertical RMS emittance with horizontal scraping. The five data points correspond to 1, 2, 3, 4, 5 mA of beam current after scraping.

this method is typically ∼0.5% of the peak intensity. This limits the dynamic range of the scanner to approximately two orders of magnitude.

To test the robustness of this method, a horizontal scraper was stepped through the beam upstream of the Allison scanner at location three and the phase portraits in the vertical plane were measured at each step. Removal of the beam horizontally results in a lower intensity of a given pixel in the vertical phase space, so that the peak intensity can be used as a measure of the remaining current. When the noise-based cut is used, the measured emittance is constant within 10%, showing that the beam ellipse is not x-y coupled (Fig. 2.13). However, when the same data are analyzed with the default 1% cut, the emittance appears to increase when the peak intensity goes below ∼1.5, corresponding to a beam current of roughly 2 mA, due to noise flooding the phase portrait.

2.2.2 Quadrupole scan

To test that the stability of the measured distributions in $J-\phi$ coordinates, the strength of an upstream quadrupole magnet close to the Allison scanner was varied. This is a change to the linear focusing optics so the Twiss parameters will change but no significant changes in the distribution over action are expected. Despite the dramatic visible changes of the portraits in $x - x'$ coordinates (seee Fig. 2.14(a)), the distribution in action-phase coordinates stays the same (see Fig. 2.14 (d,e)), and portion of particles outside of a given action is stable for more than 99% of the measured beam (see Fig. 2.14 (f)). The portion of particles in the core and the central slope are found to be stable (see Fig. 2.14(b)) within $\pm 3\%$ and $\pm 5\%$, respectively.

The phase of the particles for scans with different optics shifts by the difference in betatron phase advance between these portraits. While a phase shift cannot modify the appearance of the phase-independent core, the phase position of the tails should change accordingly. In the case of the presented quadrupole scan, the change in the phase advance is small because the distance between the varied quadrupole and the Allison scanner is short. The observed phase position of the branches is in agreement, within measurement errors, with the simulated phase advance (see Fig. 2.14 (c)).

2.2.3 Comparison of measurements in different locations

The stability of description of the distributions in action-phase coordinates allows for comparisons of the phase portraits of the beam that have passed through significantly different optics. As mentioned above, phase portraits were recorded in three locations and with two scanner orientations over 18 months. The results of these measurements, performed with

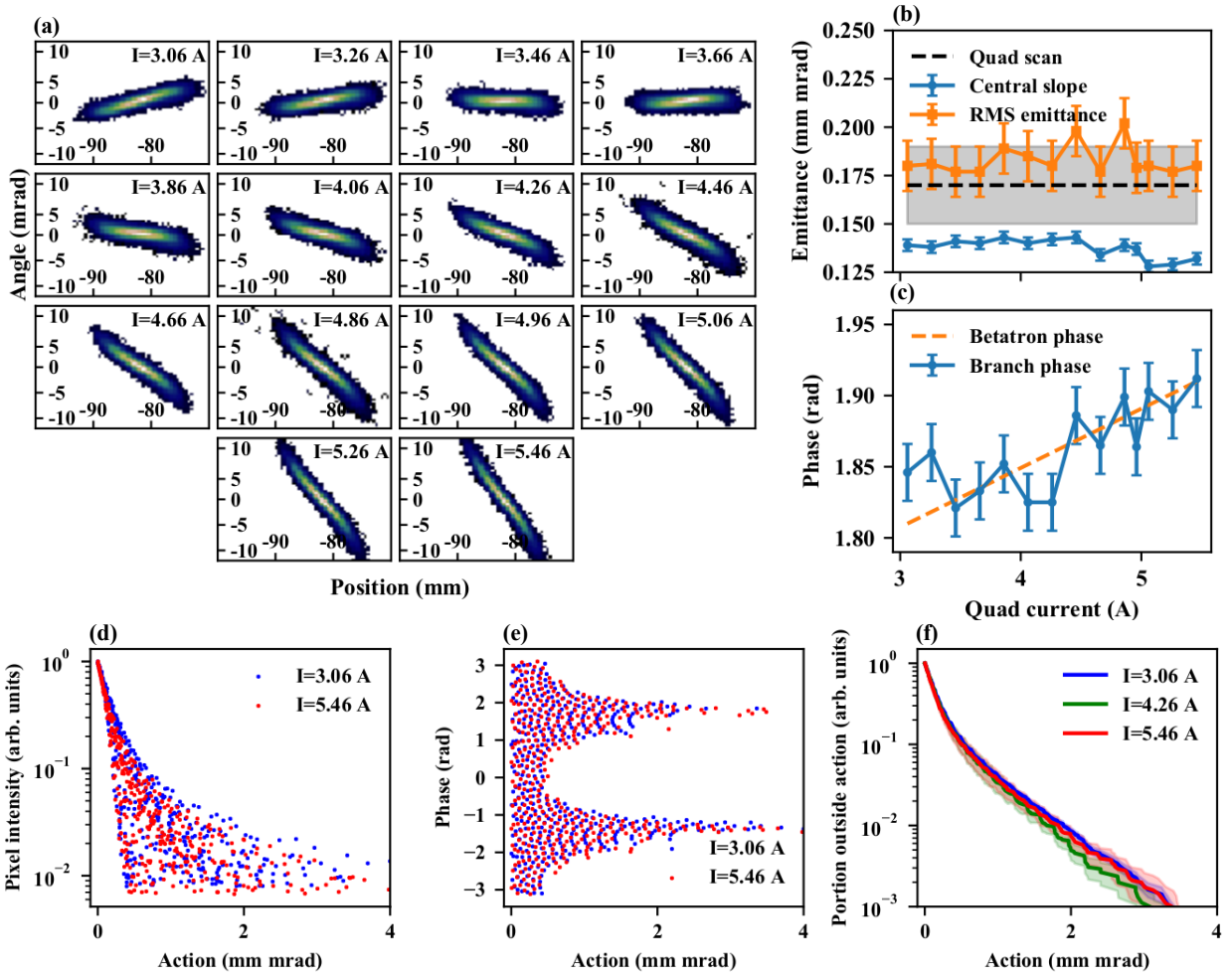

Figure 2.14: Analysis of phase protraits in a quadrupole scan. (a) phase portraits in $x - x'$ coordinates recorded at the quadrupole currents increasing from left to right and from top to bottom from 3.06A to 5.46 A. The x and x' ranges in each plot are 30 mm and 24 mrad, correspondingly. No significant variation of the slit - corrected central slope and percent in the core are observed while the quadrupole strength was scanned (b). The average branch phase agrees with small changes of the simulated betatron phase (c). Phase portraits in action-phase coordinates for the minimum and maximum quadrupole currents overlap (d), (e). The portion of the beam outside of a given action is stable over most of the beam (f).

the same settings for the ion source, LEBT, and RFQ, are summarized in Table 2.3. Each result represents an average over 10 measurements made on different days in an attempt to separate day-to-day variability from difference between locations and orientation. The presented errors are the rms variations over each set of 10 measurements.

Across all three locations of the Allison scanner, the rms emittance is the same within the errors which was initially interpreted as no significant differences in the distributions. However in $J-\phi$ phase space, higher values of the central slope and percent in the core at the location 1 were measured. This is attributed to a difference between the distributions in the horizontal and vertical planes, since these values stay constant from location 2 to location 3. This difference between the two planes is also seen in the larger spread in intensities at low action for the horizontal plane at location 1 compared to the other two locations (Fig. 2.15 left). However, direct comparison by measuring both planes in single location was not performed to confirm this theory.

There is no change, within the scatter, in ϵ_c and the fraction of the intensity in the core between locations 2 and 3 in which the Allison scanner measured in the vertical plane. This is interpreted as an absence of measurable changes in the beam core parameters in the MEBT. The extent of the beam tails can be more easily seen by plotting the total intensity of pixels with action larger than some value as a function of action, i.e. integrating the intensity-action distribution (Fig. 2.15 right). Outside of $\sim 95\%$ of the measured beam intensity, the difference between distributions is larger that one would expect from statistical fluctuations and reconstruction errors by comparing with Fig. 2.14 (f). The increase of particle population outside of large actions from location 2 to location 3 visible in Fig. 2.15 (right) may be a sign of tail growth. However, due to the limited dynamic range of the Allison scanner and existence of beam jitter, it is difficult to make a definitive claim.

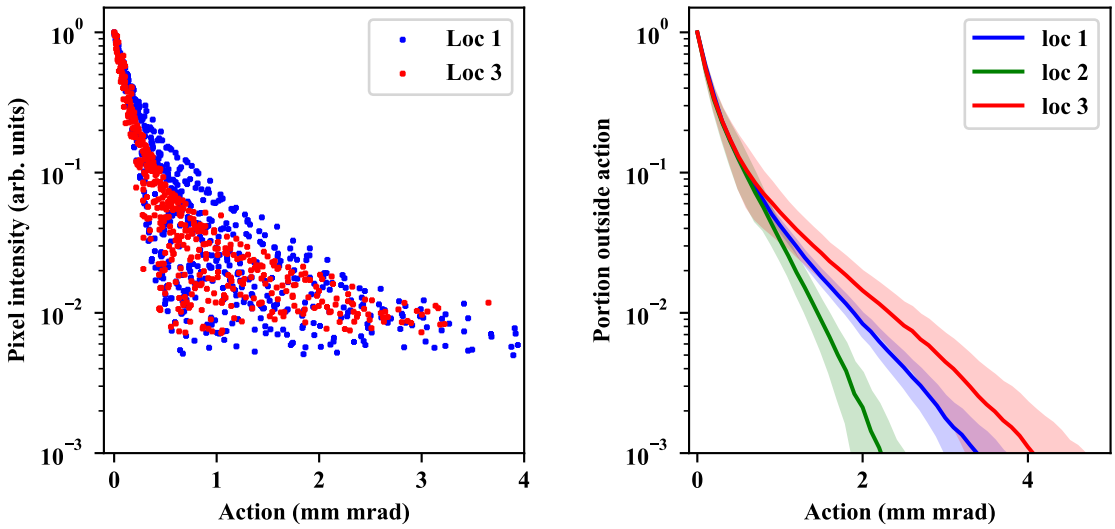

Figure 2.15: Comparison of the amplitude versus action distribution (left) at the beginning and end of the MEBT shows a difference between the horizontal and vertical planes. The far tails extend farther at location 3 compared to location 2 (right) which is a sign of tail growth. The portion outside a given action at location one cannot be used to search for tail growth because it represents a different plane. The shaded areas represent the rms errors calculated by propagation of the pixel amplitude fluctuations.

Table 2.3: Average rms emittances and core and tail parameters for the three locations of the Allison scanner.

Location	rms ϵ	ϵ_c	% in core
1 - horz	0.20 ± 0.013	0.146 ± 0.003	88 ± 2.5
2 - vert	0.19 ± 0.015	0.117 ± 0.013	71 ± 11
3 - vert	0.22 ± 0.024	0.123 ± 0.011	72 ± 10

2.2.4 Distribution at different beam currents

Changing the beam current is another example where distribution over action gave more detailed information about the beam distribution than the rms parameters. Figure 2.16 shows how the beam parameters at location 1 vary when the beam current is increased by increasing the extraction voltage of the ion source. All other settings, tuned to optimize performance at the nominal 5 mA, are kept constant.

Looking solely at the rms parameters that are were initially used to quantify the dis-

tributions, an increase in the rms emittance is seen starting at ∼3 mA coincident with the flattening of the peak intensity of the beam. This appears to be a saturation of the beam core resulting in increased tails.

However, the parameters used to describe the action distribution tell a different story. At 3 mA the fraction of the beam in the core plateaus as does J_{tr} signifying minimal tail growth at higher currents. The central slope, however, continues to increase for all currents. At low current, the growth of the central slope is compensated by a reduction in the size of the tails resulting in minimal changes to the rms emittance. Above 3 mA, the central slope continues to broaden, but the tails see less variation. It is the broadening of the central region that causes in the increase in the rms emittance, not tail growth.

2.2.5 Scraping

The PIP2IT MEBT contains four sets of four scrapers each set consists of a bottom, top, right, and left scraper. One goal of the scraping system in the PIP2IT MEBT is to remove far tails and intercepting part of the beam with the scraping system was foreseen as a normal mode of operation. Preliminary estimates for tail removal were made for a phase-independent Gaussian beam in Ref. [47]. In this case, it is optimal to separate the scraper by $\pi/2$ betatron phase advance to minimize the maximum passable action. However, measurements with the Allison scanner showed the situation to be more complicated due to the phase-dependent branches. For illustration, Fig. 2.17 compares phase portraits recorded at location three when removing beam with a single scraper at different locations. For this study the top scraper was moved into the beam at each of the scraping stations, one at a time, to intercept 10% of the current (0.5 mA) based on the measured current at the beam dump. In Fig. 2.17 phase portraits with (red) and without (blue) scraping are overlapped in $x - x'$ (left) and

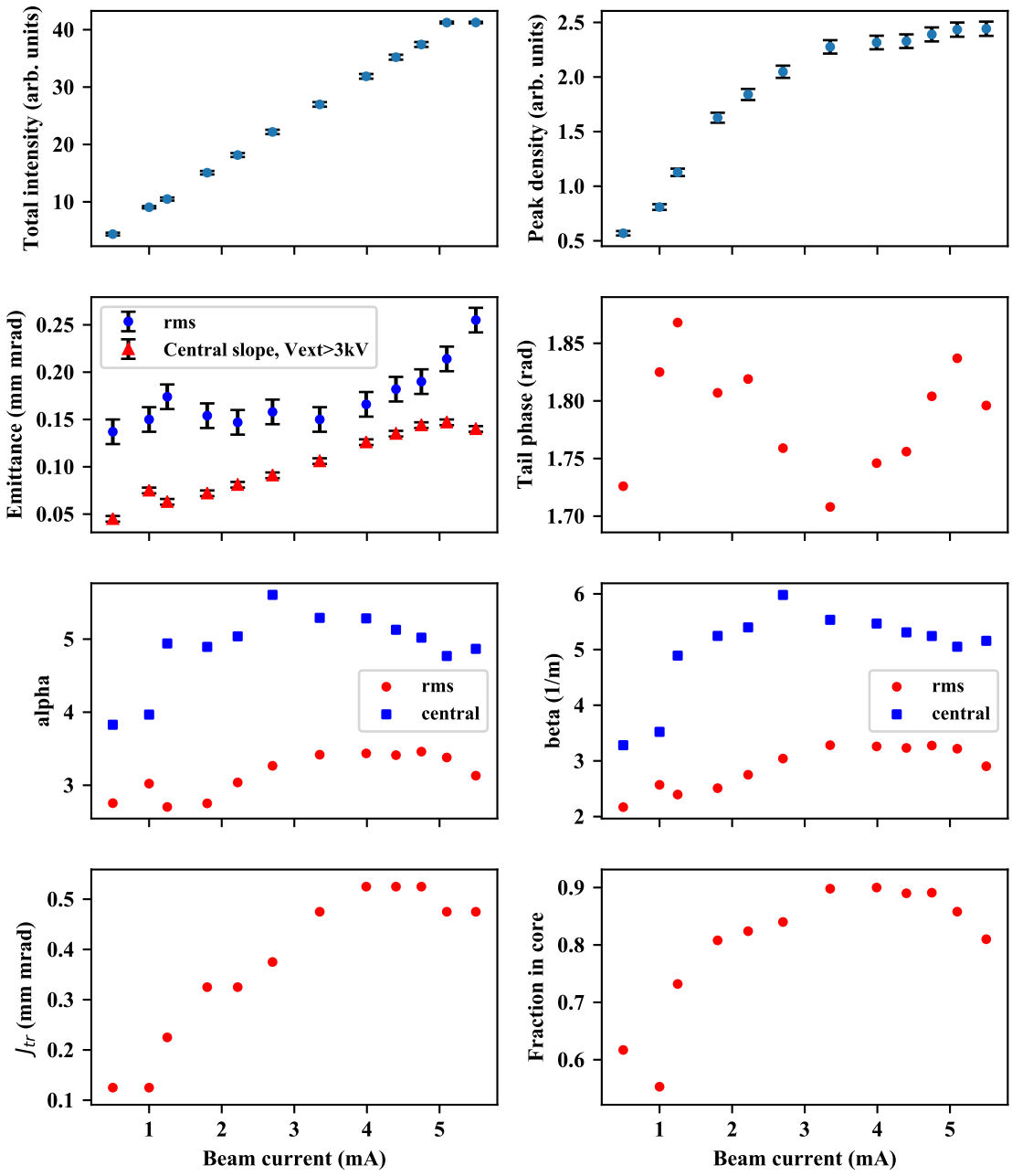

Figure 2.16: The total beam intensity (a), peak pixel amplitude (b), emittance (c), and Twiss parameters (d) for different extraction voltages V_{extr}. Parameters are plotted as functions of the beam current in the LEBT.

$J - \phi$ (right) coordinates. The action and phase of the scraped beams are calculated using the beam centroid and the central Twiss parameters of the non-scraped beam to maintain the same definition of action for direct comparisons.

Figure 2.17 shows that scraping the same fraction of the beam current by different scrapers results in different removal of the tails due to a strong dependence of the tail intensity on phase. For example, inserting the scraper M71 (Fig. 2.17(d)) removes primarily the tail particles, while the scraper just upstream, M61 (Fig. 2.17(c)) misses a significant portion of the branches and does not reduce the maximum action of the beam. Instead, in order to remove 10% of the current, the scraper removes particles with lower action. Therefore, in order to achieve maximal tail reduction for a given reduction of the output beam current, the beam phasing at the scrapers can be optimized by adjusting the optics and/or scraper locations such that the phases of the branches are at 0 or π at the scrapers. Alternatively, if such changes to the optics are not possible, scrapers that are not expected to intercept the tails can be positioned to remove less of the total beam current with minimal increase to the passed maximum J. This can result in a more efficient scraping regime than will remove less of the total current but still remove the large action beam tails.

Phase portraits for scraping near location 1 with scraper M00 visibly show a rounded edge on the scraped side. This is visually distinct from scraping near location 3 with scraper M71 where phase portraits have a straight scraped edge, Fig. 2.17. This hints that for the upstream scrapers propagation through the beam line smears the scraping boundary beyond of what is expected from the finite width of the scanner slits. This could be related to non-linear space-charge fields, as expected from preliminary simulations in Ref. [47]. In attempting to make a numerical estimation of this effect, one can propagate the scraper footprint using the transport matrix and calculate the portion of the particles beyond the

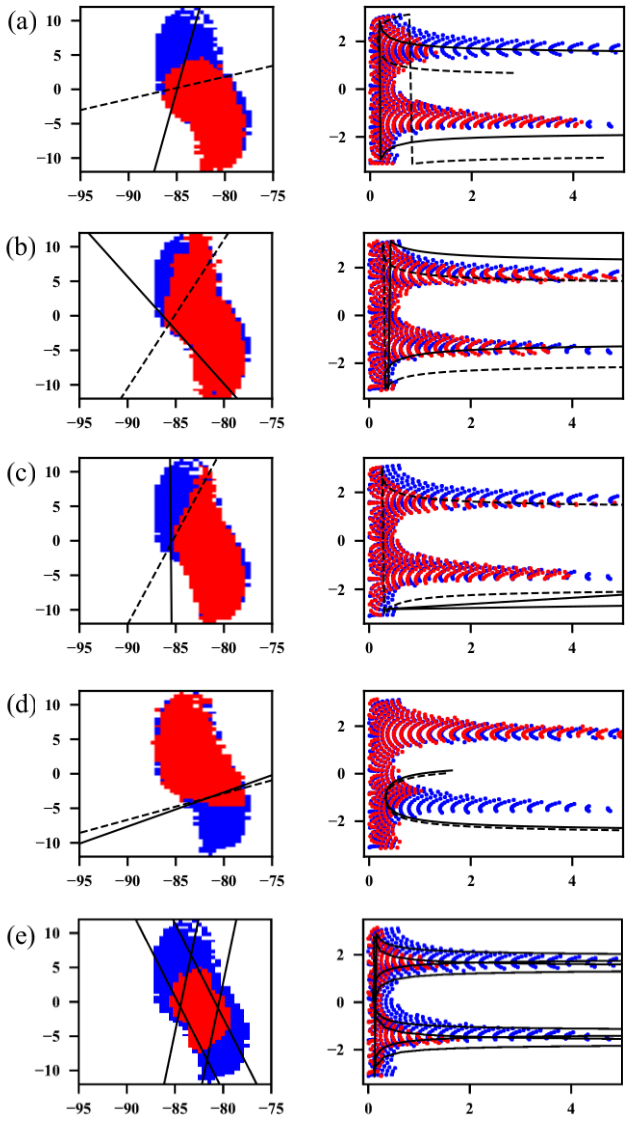

Figure 2.17: Phase portraits with scraping. Rows (a) - (d) correspond to moving into the beam one of the scrapers along the beam line presented in Fig. 2.3; from top to bottom M00, M11, M61, M71. In each case, 0.5 mA is intercepted out of the initial 5 mA. The row (e) represents the 'flat' beam when top and bottom scrapers are inserted in M00 and M11 stations. The solid lines represent the attempt of propagating the scrape lines according to 5 mA beam simulations. The dashed lines represent propagation with the phase advance increased by 10%. See other details in the text.

cut line in the recorded portrait. A scraper with vertical offset d from the beam center produces a line in the Allison scanner portrait

$$u_1'(u) = \frac{u}{\beta_1}\left(\cot(\Delta\phi) - \alpha_1\right) - \frac{d}{\sqrt{\beta_0\beta_1}\sin(\Delta\phi)} \tag{2.22}$$

where subscripts 0 and 1 denote the locations of the scraper and Allison scanner, correspondingly, $\Delta\phi$ is the vertical betatron phase advance between the two locations, and α and β are the Twiss parameters. The center of the coordinate system is placed at the center of the distribution. The rms Twiss parameters at the Allison scanner are measured directly. At the scraper, the offset and the rms beam size and, assuming a constant emittance, β_0 can be reconstructed by stepping the scraper through the beam and recording the passed current on the beam dump. The dump current as a function of the scraper position can be fit to the standard error function to determine the first and second order moments. The phase advance needs to be delivered by the optics model. The rms parameters, simulated by TraceWin [48], are found in a good agreement with the envelope measurements performed with scrapers [49], and the phase advances are calculated using the rms beam sizes and emittances delivered by the program. The scraper footprints drawn according to Eq. 2.22 are shown on all plots of Fig. 2.17 with solid lines. These lines were expected to approximately coincide with the scraped edge of the beam distribution. However, this visually is not the case, and numerical estimations of the particles' diffusion over the scraper footprints cannot be made. A possible interpretation of this result is that the accuracy of prediction with the linear model with uniform phase advance for all particles becomes unsatisfactory for the case of long propagation of the tails with non-linear space charge and focusing forces. Simulations performed with the same initial conditions and the same magnet settings but with a zero

beam current show the phase advances that are larger than at nominal 5 mA by 10 - 20% [47] (depending on the longitudinal position). Because the density varies across the beam, it can assumed that the tail particles advance in the phase with a rate somewhere between the zero current and nominal cases. The dashed lines in Fig. 2.17 drawn with the phase advances increased by 10% to estimate the reduced betatron tune depression of the tails for each portrait are indeed visually closer to the scraper footprints.

This assumption of non-uniform phase advances is supported by an increasing phase shift of the second harmonic as a function of action throughout the MEBT. The second harmonic was calculated by taking the Fourier transform with respect to phase in normalized action bins ΔJ=0.05 mm mrad wide. This was done for measurements at each of the three locations of the Allison scanner and the phases were shifted by a constant to have zero phase at higher J for easier comparison (Fig. 2.18). At location 1, the phase is mostly constant with action. At location two, the phase starts to decrease at lower actions and this behavior becomes larger at location three. The shift in the second harmonic is approximately proportional to the amplitude of the 0^{th} harmonic at all locations, i.e. the amplitude of the local density. This effect can be interpreted as the tails have a different phase advance from the core resulting in the beam becoming 'S' shaped [18].

This increasing 'S' shape can explain that despite having the same ϵ_c and fraction in the core, the distribution at location 3 extends to higher action compared to location 2 (see Fig. 2.15). The tail particles are shifting away from the primary axis of the ellipse defined by the central parameters encompassing the core. This would cause the tails to move to higher actions without the central distribution or the total population of tail particles changing.

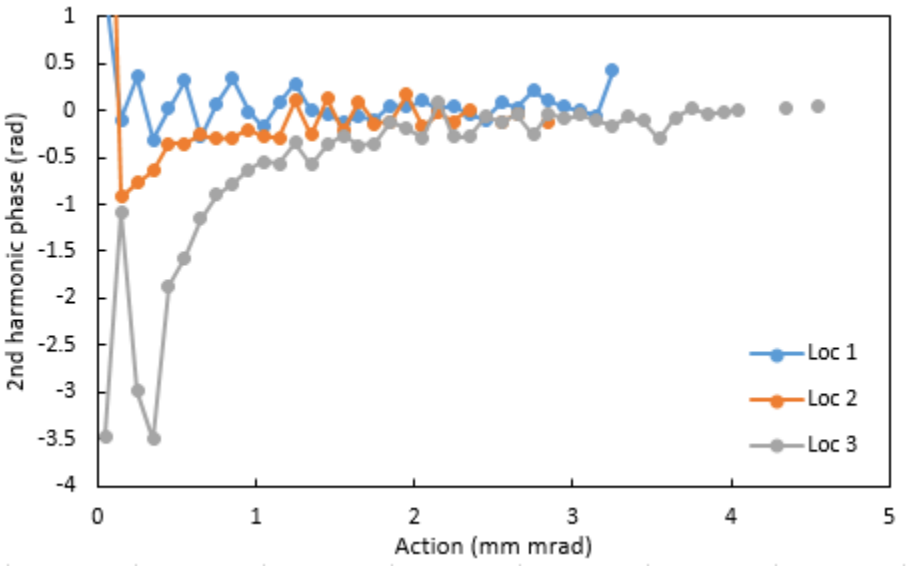

Figure 2.18: Phase of the second harmonic of the pixel intensities as a function of phase varies with action. Larger variations are seen father from the start of the MEBT showing the phase advance varies across the beam.

2.3 Future work

The development of the analysis of phase portraits using $J - \phi$ coordinates was intended for studying the beam tails. Unfortunately, noise issues with the Allison scanner in the PIP2IT beamline made this challenging. The thermal noise was quite large and limited the dynamic range of the device to roughly two orders a magnitude. To adequately measure the beam tails, a dynamic range of at least three or four orders of magnitude is required. While we did investigate the source of the large noise floor, no correction was found.

In addition, the beam jitter distorts the measured phase space distribution. The jitter appears to be random, therefore the measured distribution on average should be mostly unaffected and adequate for determining the rms beam parameters. However, the jitter does affect the pixel intensities on the individual level which confounds detailed analysis of the phase portraits using action.

Because of these issues, it is challenging to further the development of this analysis

technique using phase portraits taken in the PIP2IT MEBT. Future studies should be taken of a more stable beam with a phase space scanner with a larger dynamic range.

Also, the intensities of the individual pixels are known to be affected by the geometry of the Allison scanner. Equation (2.13) provides a simple model of this effect for a Gaussian beam and it is needed to determine the central parameters. It would be ideal to correct the intensity of each pixel for this effect. This procedure is essentially a deconvolution of the measured phase portrait with the passed phase space area for a given position-voltage setting (Fig. 2.8) and a procedure for this is described in Ref. [46]. However, deconvolution is an inherently noisy process and, due the added noise from beam jitter, attempts to carry out this correction failed. Once again, cleaner signals are needed to improve the analysis.

Chapter 3

Beam profile measurements using beam position monitors

Measurements of the beam distribution in phase space are useful to fully characterize the beam. However, these devices can typically only be used in low energy regions of the beamline because they rely on the lower magnetic rigidity of beam to sample discrete portions of the beam. In addition, because these devices intercept the beam, they must be able to withstand the deposited beam power which becomes more challenging at higher energies. Also, because they are inserted into the beamline, the phase space measurements cannot be performed during operation. While slit based phase scanners are useful for characterizing the beam distribution, typically, there will only be a couple phase space scanners in a beamline and cannot be used to continuously monitor the beam properties.

On the other hand, the most prevalent diagnostic devices in almost every beamline are beam position monitors. These non-intercepting devices are used throughout the entirety of accelerators as one of the primary tools to verify the beam dynamics and tune of the beamline. Standard analysis of the BPM signals only determines the first order moments (centroid) of the beam. Expanding the analysis of the BPM signals to give more information about the beam distribution would allow for passive monitoring of more beam properties at many locations. This additional information would be highly beneficial for determining the

operation points of particle accelerators.

3.1 BPM signals

3.1.1 Validity of the pencil beam model

The electric field given by Eq. 1.46 holds for a infinitesimally small beam transversely with charge modulated longitudinally at a single frequency. While, this is clearly a significant abstraction from an actual beam, it is an adequate model of the BPM signals in most cases and widely used [5]. The single frequency model is acceptable because the processing of the BPM pickups' signals typically use narrowband filtering to measure a single harmonic of the bunch repetition rate to reduce noise. In addition, at higher beam energies, the Δ/Σ signals are approximately frequency independent.

The pencil beam is an acceptable model of the transverse distribution if the beam is small compared the pipe radius. However, when the beam size covers an appreciable portion of the pipe aperture, the signals measured by the pickups can be modeled by summing over a collection of pencil beams at different locations to generate the transverse profile. The components of this discretized model far from the center will be affected by the non-linearities in the pickups' response and cause the measured position to be distorted [7]. This distortion is dependent on the exact transverse distribution making it challenging to model. Because this effect is due solely to non-linearities caused by the geometry of the BPM, it is independent of gR_p and non-relativistic effects.

This is effect is typically on the order of a few percent variation and typically is not considered when determining the beam position. For example, consider a Gaussian beam with $\sigma_y = 2$ mm located at x_0=2 mm and y_0=1 mm in a pipe of radius $R_p = 23.5$ mm. When

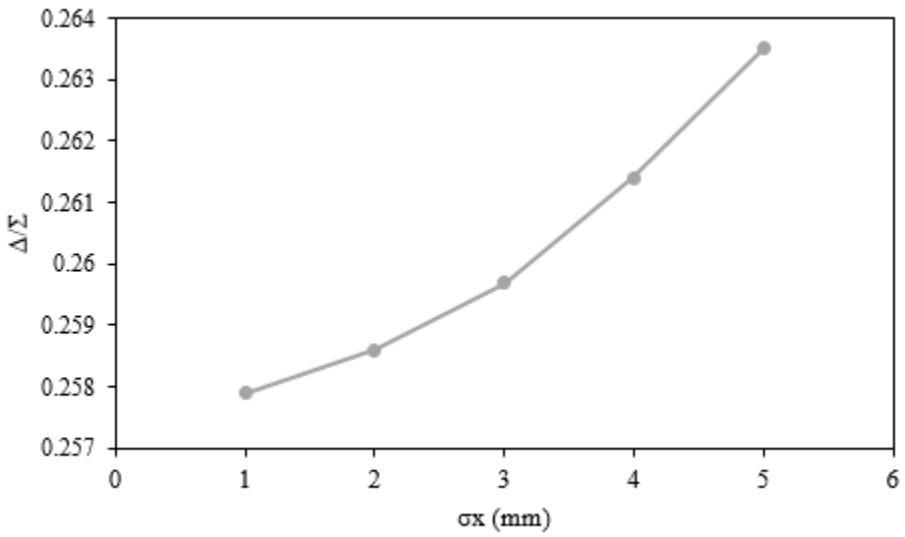

Figure 3.1: Variation of Δ/Σ when changing σ_x of a Gaussian beam centered at x_0=2 mm and y_0=1 mm for a 47 mmm aperture BPM with 20 mm diameter round pickups.

σ_x is varied from 1 mm to 5 mm, the resulting Δ/Σ, and therefore the position measurement, varies by 2-3% (Fig. 3.1). While these beam offsets are larger than ideal, these parameters are representative of a beam in the FRIB MEBT.

3.1.2 A more detailed BPM model

While this infinitesimally thin, single frequency model of a beam is generally adequate for position measurements, in reality the signals from BPM pickups also contain information of the longitudinal bunch profiles. The BPM signals are directly proportional to the Fourier amplitude of the longitudinal profile D_ω at the measured frequency. Therefore, it is possible, using beamline models, to measure the longitudinal size of the bunch by varying the longitudinal optics and measuring changes in the amplitude of a signal harmonic to calibrate for these effects and use the BPMs to measure the longitudinal bunch length [50, 51]. In theory, the beamline model dependence can be removed by recording the BPM pickups' response at multiple frequencies. In order to achieve this, a more complete analytic model than Eq.

1.46 is needed.

One important missing feature in Eq. 1.46 is the dependence on the transverse distribution which is more complex than the longitudinal distribution dependence. The dependence of the image charges on the pipe wall σ_{wall} for a given transverse distribution $T(r,\phi)$ can be found by integrating Eq. 1.46 for σ from a pencil beam over $T(r,\phi)$

$$\sigma_{\text{wall}}(\omega, z_m, \phi_m) = D_\omega \cos\left(\omega\left[t + \frac{z_0 - z_m}{\beta c}\right]\right) \times \iint r dr d\phi \sum_{n=0} T(r,\phi) \frac{I_n(gr/R_p)}{\pi N I_n(gR_p)} \cos[n(\phi_m - \phi)]. \tag{3.1}$$

The effect of the transverse distribution is more discussed in section 3.1.3.

The image change must now be integrated over the pickup. For a round pickup, which are used at FRIB, of radius R_b Eq. 1.53 becomes

$$\sigma_{\text{pickup}}(\omega) = \int_{-R_b}^{R_b} \mathrm{d}z \int_{-\frac{1}{R_p}\sqrt{R_b^2 - z^2}}^{\frac{1}{R_p}\sqrt{R_b^2 - z^2}} R_p \, \mathrm{d}\phi_m \sigma_{\text{wall}}. \tag{3.2}$$

For simplicity all terms in σ_{wall} independent of z_m and ϕ_m will be put into a single coefficient

$F(g, r, \phi)$ and $\phi \mapsto \phi + \phi_p$ to accommodate any azimuthal pickup location ϕ_p. This gives

$$\sigma_{\text{meas}}(\omega) = \int_{-R_b}^{R_b} \mathrm{d}z_m \int_{-\frac{1}{R_p}\sqrt{R_b^2-z^2}}^{\frac{1}{R_p}\sqrt{R_b^2-z^2}} R_p \, \mathrm{d}\phi_m \iint r \mathrm{d}r \mathrm{d}\phi \times \sum_{n=0} F \cos[n(\phi_m - \phi_p - \phi)] \cos\left[\frac{\omega}{\beta c}(z_m - z_0)\right] \tag{3.3}$$

$$\sigma_{\text{meas}}(\omega) = \iint r \mathrm{d}r \mathrm{d}\phi \sum_{n=0} F R_p \frac{2}{n} \cos[n(\phi_p + \phi)] \times \int_{-R_b}^{R_b} \mathrm{d}z_m \cos\left[\frac{\omega}{\beta c}(z_m - z_0)\right] \sin\left[\frac{n}{R_p}\sqrt{R_b^2 - z^2}\right] \tag{3.4}$$

$$\sigma_{\text{meas}}(\omega) \equiv \iint r \mathrm{d}r \mathrm{d}\phi \sum_{n=0} F R_p \cos[n(\phi_p + \phi)] \cdot P(\omega) \tag{3.5}$$

where

$$P(\omega) = \frac{2}{n} \int_{-R_b}^{R_b} \mathrm{d}z_m \cos\left[\frac{\omega}{\beta c}(z_m - z_0)\right] \sin\left[\frac{n}{R_p}\sqrt{R_b^2 - z^2}\right] \tag{3.6}$$

is the transit time factor for a round button pickup. Therefore the correction for the button shape can be separated from the effects of the beam distribution.

This derivation approximates the pickup geometry as flush with the round pipe wall. In practice, flat button pickups are commonly used because they are simple to manufacture. Show in Fig. 3.2 is the inside of a BPM used at FRIB where flat, 20 mm diameter pickups are used and they are recessed 1 mm from the inner pipe wall. This difference in geometry needs to be accounted for when the measured wavelength is on the same order as the pickup size. For the 20 mm diameter pickups used at FRIB, the frequency needs to be above ∼0.5 GHz for a beam traveling at $\beta = 0.033$ corresponding to the beam energy exiting the RFQ. This estimate is confirmed by CST Microwave Studio [52] simulations of the two BPM geometries at this velocity which show the difference becomes significant at ∼400 MHz (Fig. 3.3). To limit the effect of the curved approximation, the broadband measurements presented below

Figure 3.2: Geometry of the FRIB MEBT BPMs. The pipe radius is 23.75 mm and the pickup radius is 10 mm [6].

with the FRIB BPMs were limited to 400 MHz.

3.1.3 Pickup signal variation with transverse distribution

The variation of the field profile with beam position, as mentioned in section 1.4.1., can be seen from the measured spectra from various offsets of a pencil beam (Fig. 3.4). Because, for non-relativistic beams, the signals on the pickups vary with ω and β_r, they are best characterized in terms of gR_p with higher gR_p corresponds to higher frequency and lower β_r. The effect of offsetting the beam is significant for $gR_p > 1$ with variations on the order of 10s of percent for values of gR_p up to $\sim$10. For $gR_p < 1$ the spectra on the buttons from an offset beam are the same as the spectra for a centered beam. Therefore, for $gR_p > 1$

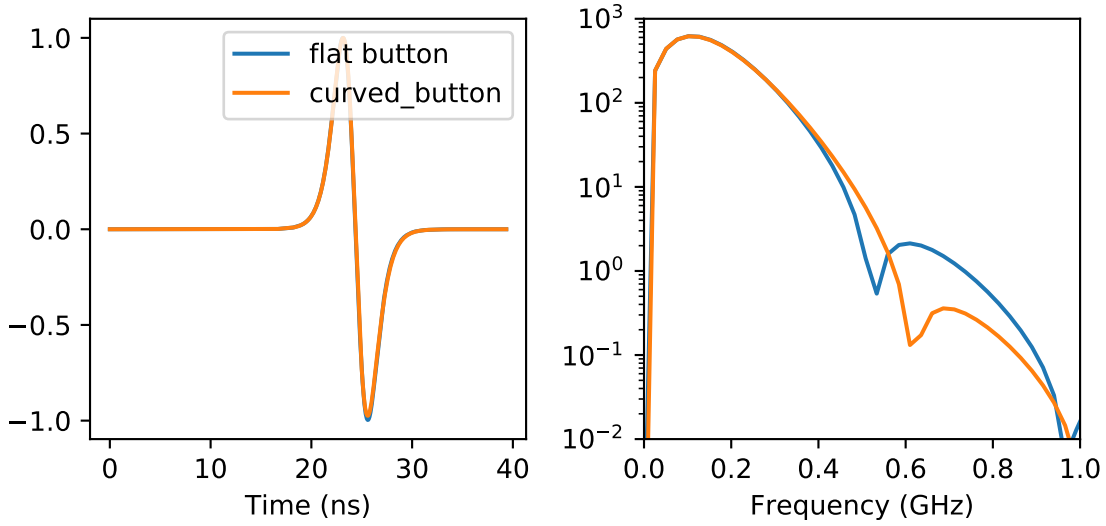

Figure 3.3: Signal on a flat and curved 20 mm diameter BPM pickup from a β=0.033 beam. The two geometries give similar results up to ∼400 MHz.

Eq. 1.51 must be used to correctly determine the position and for $gR_p < 1$ Eq. 1.52, which independent of g, can safely be used.

To see the effect of the transverse distribution, the amplitude of the integral in Eq. 3.1 is plotted in Fig. 3.5 as a function of gR_p and are normalized to the result a pencil beam. A Gaussian beam with $\sigma_x = \sigma_y$ was used and the transverse size was varied. Similar to offsetting the beam, the variations due to transverse beam size are significant for $gR_p > 1$. For $gR_p < 1$, the transverse size can be neglected and a pencil beam can be assumed. Similar effects are seen when varying σ_x or σ_y individually while leaving the other fixed. This dependence on the transverse distribution at high gR_p caused by the electric field distribution and is distinct from the errors caused by the transverse beam distribution due to non-linearities discussed in section 1.4.1. Because the transverse distribution can affect the field profiles on the BPM pickups, the transverse distribution should be able to be determined from the pickup signals. This would require measurements at multiple frequencies to separate the transverse effects from longitudinal profile effects. Such would measurements would

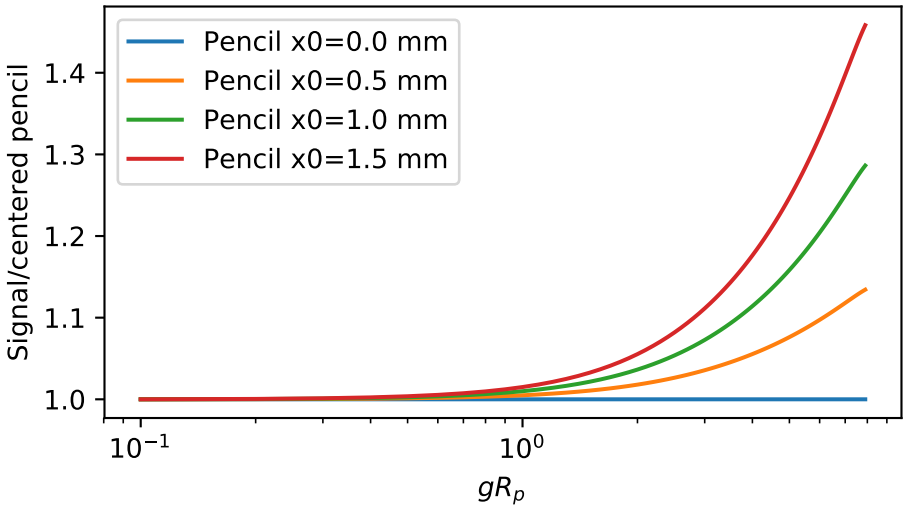

Figure 3.4: Variation in the measured spectra on a 20 mm diameter pickup in a 47.5 mm diameter pipe for an offset pencil beam. The spectra are normalized to the centered case.

Table 3.1: Parameters of the distributions used in Fig. 3.6.

	Amp 1	x_0 1	y_0 1	σ_x 1	σ_y 1	Amp 2	x_0 2	$_y$0 2	σ_x 2	σ_y 2
Double Gaussian	1	0 mm	1.07 mm	1.7 mm	2.49 mm					
Single Gaussian	1	0 mm	0 mm	1.7 mm	1 mm	0.4	0 mm	2 mm	1.7 mm	3 mm

effective turn BPMs into transverse and longitudinal profile monitors.

If a BPM is operating in a region where where transverse distributions must be accounted for, it is important to use the exact distribution. It is not sufficient to use a model with the same first and second order moments. For example, consider a beam with transverse profile that is the sum of two Gaussian and a beam with a single Gaussian profile with the same first and second order moments, e.g. distribution with parameters given in Table 3.1. At high gR_p the measured signals significantly differ both in amplitude and profile resulting in errors in the measured position (Fig. 3.6). This effect is difficult to correct because it requires an accurate model of the the beam. At lower gR_p the measured spectra become nearly identical on all pickups and the distribution no longer needs to be taken into account.

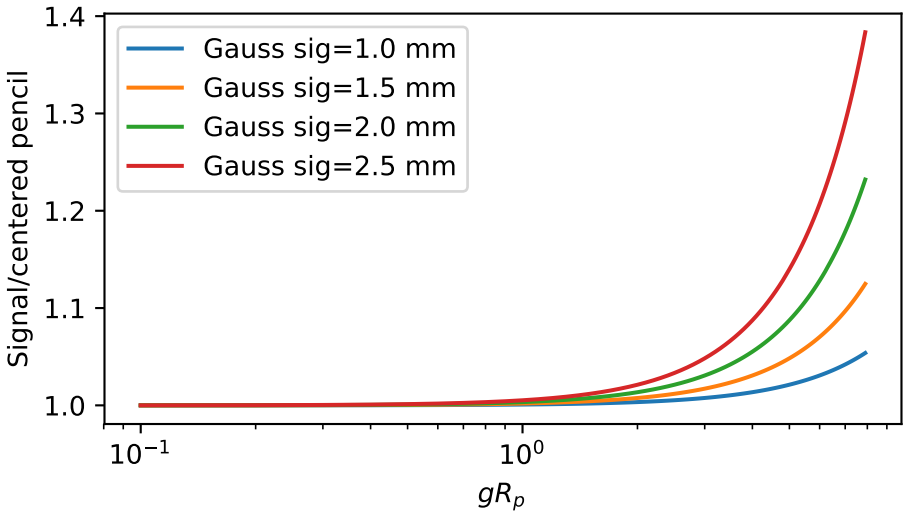

Figure 3.5: Variation in the measured spectrum for a centered round Gaussian beam of different sizes. The spectra are normalized to a centered pencil beam.

3.1.4 Button sum signal

The dependence on the pickup spectra on the transverse distribution makes measurements of the beam profiles challenging. To partially alleviate this sensitivity, the signals from all four buttons can be added together. By summing Eq. 3.5 over the four pickups, the summed signal is found to be

$$\sigma_{\text{sum}}(\omega) = P(\omega) \iint r\mathrm{d}r\mathrm{d}\phi \sum_{n=0} FR_p \Big(\cos[n(0+\phi)] + \cos[n(\pi/2+\phi)] + \cos[n(\pi+\phi)] + \cos[n(3\pi/2+\phi)] \Big) \tag{3.7}$$

$$\sigma_{\text{sum}}(\omega) = P(\omega) \int \mathrm{d}A_{\text{beam}} \sum_{n=0} FR_p \cdot 4\cos(n\phi) \begin{cases} 1, & n \equiv 0 \pmod 4 \\ 0, & \text{else} \end{cases} \tag{3.8}$$

For the circular button pickups used for FRIB, only azimuthal harmonics that are zero modulo four remain after summing. This significantly reduces the dependence of the signal

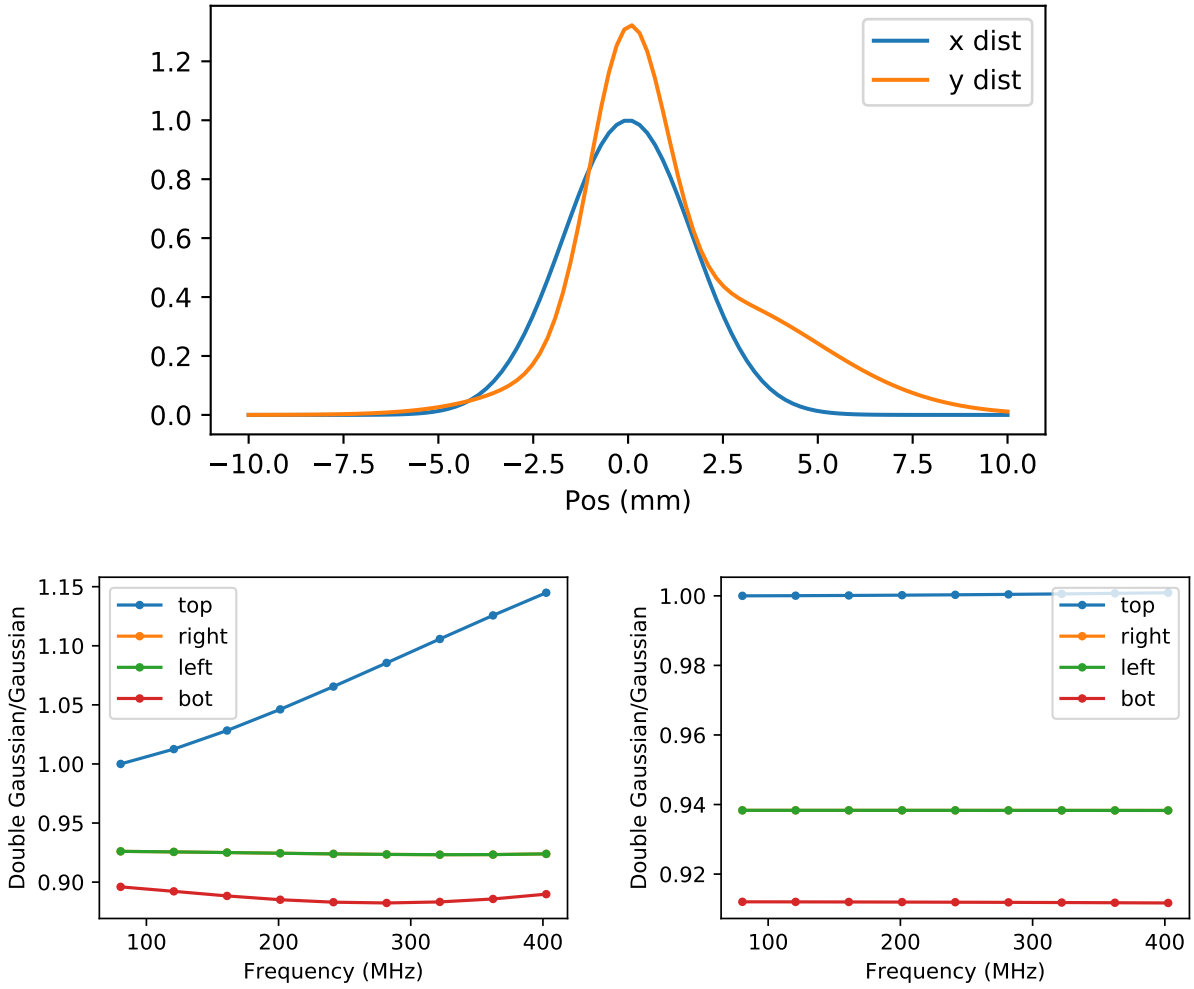

Figure 3.6: Comparison of measured spectra from a Gaussian and double Gaussian beam with the same first and second order moments with β=0.033 (left) and β=0.15 (right). At large g the different distribution results in a different measured spectra.

on ϕ as well as the dependence on the beam position and transverse distribution. In the case of rectangular pickups that cover the full 2π solid angle, only the $n = 0$ component remains and the signal is independent of ϕ.

The scalings with the transverse distribution discussed above are repeated in Fig. 3.7 using the summed signals for the FRIB BPM geometry. The dependence on beam offset for a pencil beam is reduced by a factor of $\sim$7 and the dependence on the transverse size for a Gaussian beam is reduced by >20% at high gR_p. The reduction of dependence on the transverse bunch shape is independent of the size of the beam. These reductions allow for the summed signal the beam can be assumed to be a pencil beam at $gR_p \approx 3$ which is an improvement from the non-summed signals which require $gR_p \approx 1$ to assume a pencil beam.

However, while this method reduces the sensitivity to the transverse distribution which is beneficial for determining the longitudinal profile, for low enough β_r, gR_p will be large enough that the transverse distribution still needs to be accounted for. But, due to symmetry, the x and y profiles cannot be distinguished from each other in the summed signal and the position can only be determined modulo a phase of $\pi/4$. This can result in the aggravating situation where the same number of parameters must be used to describe the beam as the non-summed case, but less information is obtained. In general, the sum signal should be used when information of the transverse distribution is not needed and when $gR_p \in (1, 3)$.

3.1.5 BPM response simulations

The required correction to recover the beam parameters from the measured signals were checked using CST Microwave Studio simulations [52]. The simulations were performed using the wakefield solver with a mono-energetic pencil beam and the field at the pipe wall was measured at a single point to confirm Eq. 1.46. This eliminates corrections for

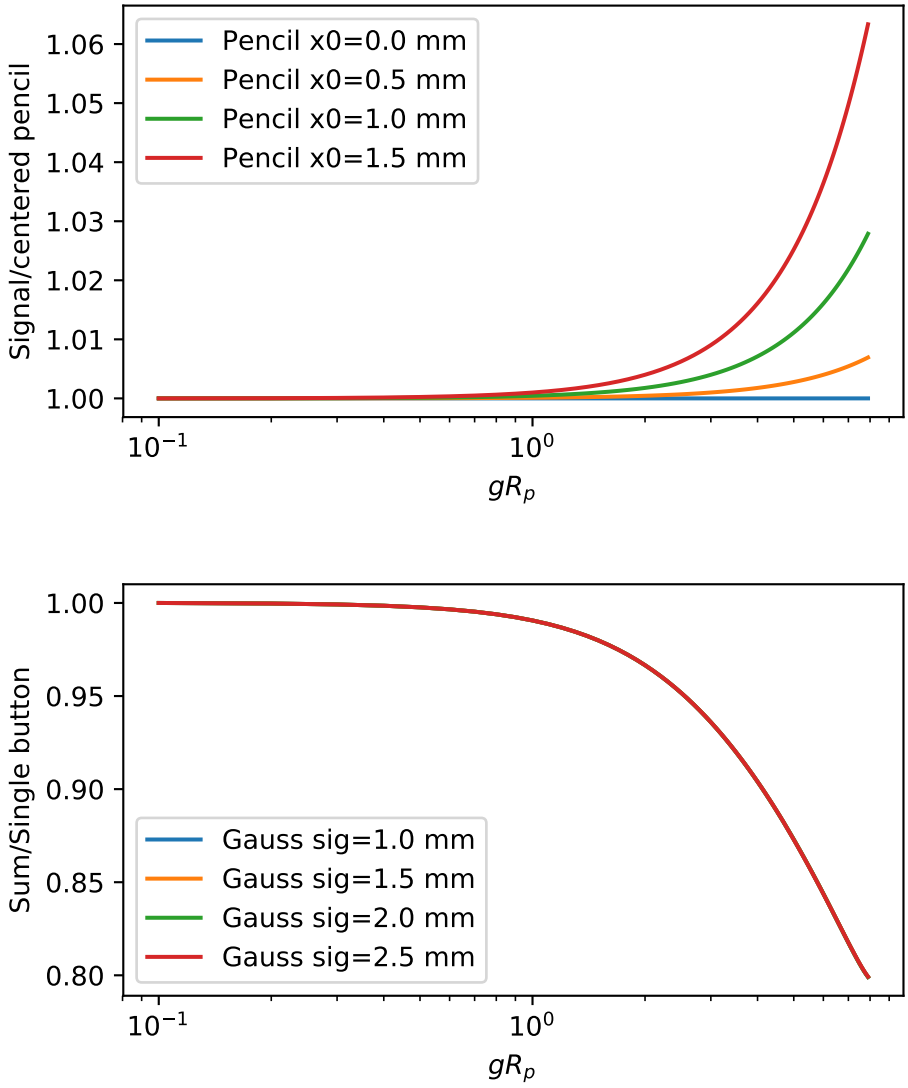

Figure 3.7: (Top) Variation of the summed signal for an offset pencil beam. The variations in the spectra are a factor of ∼7 lower than the non-summed signals. (Bottom) The summed signals of a 1 mm offset Gaussian beam normalized to the single pickup signals. The variations of the summed spectra are reduced by 20% compared to the non-summed signals.

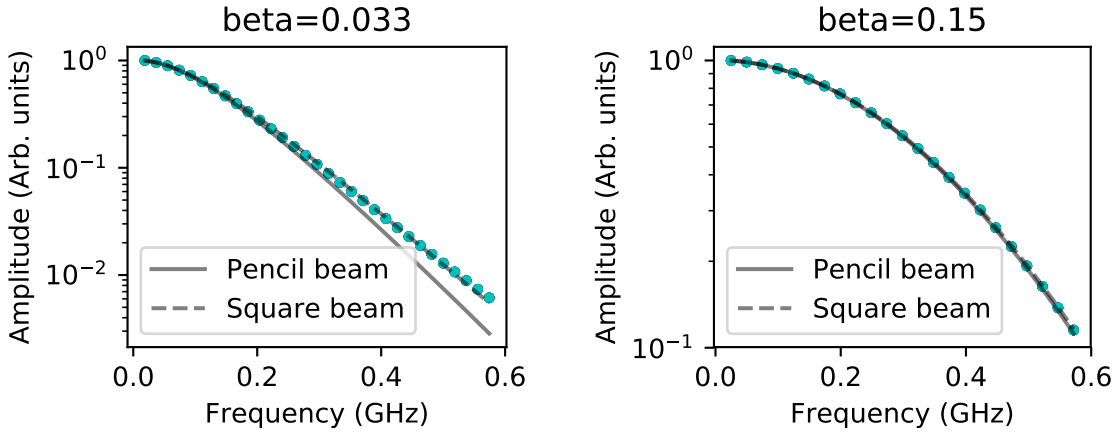

Figure 3.8: CST simulations using the wakefield solver must be fit to a uniform square beam with side length given by the mesh size. For the given frequency range, this artificial transverse distribution can be ignored for β >0.15.

the transverse size and the pickup geometry and impedance; these features were planned be added later to test Eq. 3.5. However, simulations using the wakefield solver showed a discrepancy between the field at a point on the wall in simulation results and the analytic field at the wall from a pencil beam for $\beta_r < 0.15$ (see Fig. 3.8).

Instead, the simulation results matched the expected signals from a uniform square beam with side length equal to twice the mesh cell size suggesting the discrepancy is caused by how CST handles the pencil beam in the wakefield solver. The pencil beam used in the wavefield solver transversely lays on the intersection of four mesh cells. The solver appears to assume all cells touching the thin, pencil beam are part of the beam and must be included in the analytic model. The damping of the transverse distribution effects by reducing gR_p is also confirmed by simulations with $\beta_r \geq 0.15$ which agree with the analytic results from a pencil beam and do not require a transverse distribution.

With this unwitting inclusion of a transverse distribution at low β, the wakefield solver was used for simulations including a BPM model. The model used is a simplified model

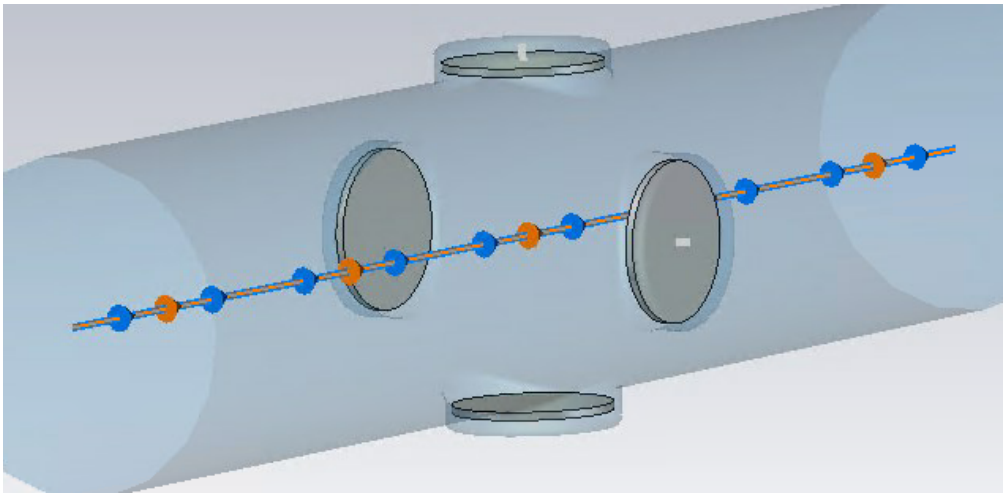

Figure 3.9: Model of the FRIB BPMS in CST Microwave Studio.

consisting of flat cylindrical buttons that are connected to ground via 50 Ω discrete ports (Fig. 3.9). The impedance of these pickups was measured using the transmission coefficient $S_{2,1}$ between two pickups and fitting for the resistance and capacitance (Fig. 3.10) similar to the procedure in Ref. [6]. The measured capacitance to ground was 4.1 pF.

The BPM signals match the expected analytic signals within 5% for $\beta = 0.033$ and the difference decreased when β was increased (Fig. 3.11). From these signals, a resonance due to the button size can be seen around 500 MHz for β=0.033. This resonance is not seen in beamline measurements due to low pass filtering.

3.2 Bunch profile measurements

3.2.1 TIS waveforms

The BPM system at FRIB can measure the signals from the buttons over a wide bandwidth using a Time Interleaved Sampling (TIS) method similar to the method described in Ref. [53]. This method assumes beam is comprised of a series of individual bunches that are

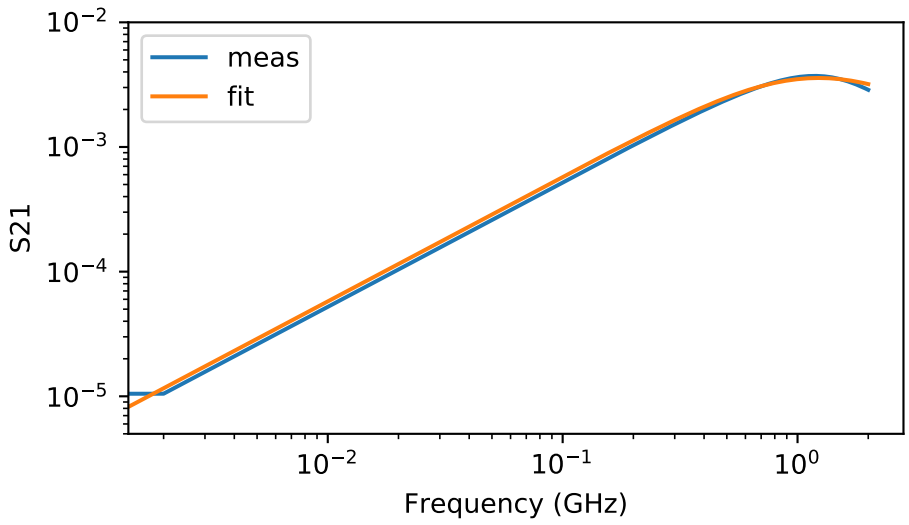

Figure 3.10: Fitting transmission coefficient, $S_{2,1}$, of a the CST button model to determine the impedance.

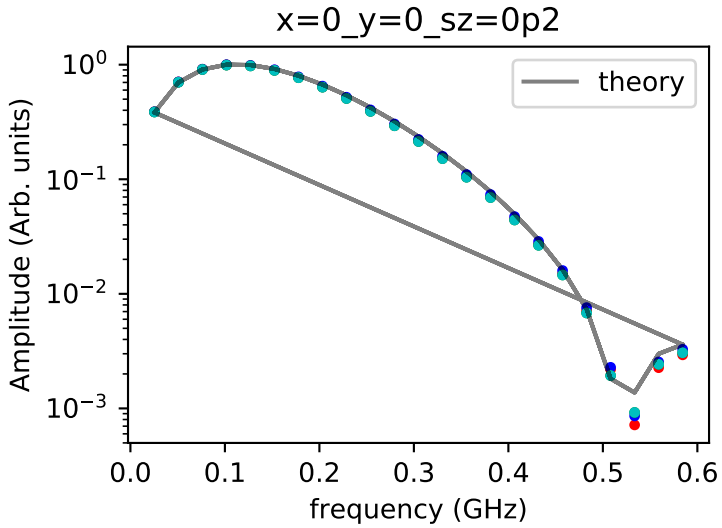

Figure 3.11: Simulation results compared to analytic results of BPM pickup signals from a centered pencil beam using the wakefield solver.

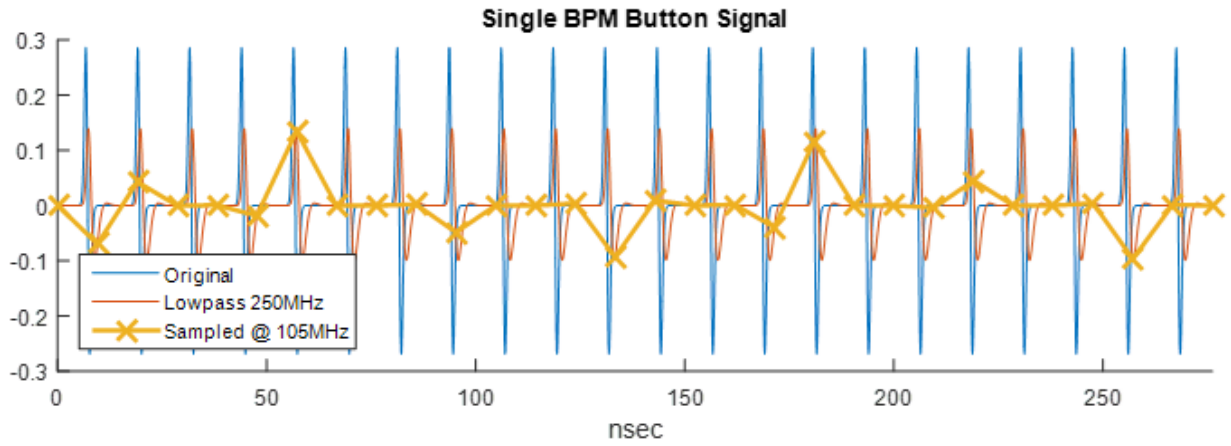

Figure 3.12: Example of the sampling procedure to measure the TIS waveforms. Each sample taken by the digitizer is at a different phase with respect to the signal and can be used to reconstruct the individual repeated pulse (image courtesy of S. Cogan).

assumed to be identical and longitudinally spaced at a repetition rate of either 40.25 MHz or 80.5 MHz. The pickup signals from the bunch train are sampled by the digitizer at 119 MHz. Each sample of the digitizer occurs at a different phase with respect to the bunches (Fig. 3.12) resulting in an effective sampling rate of 2.737 GHz and can resolve harmonics of 40.25 MHz up to 1.3 GHz. However, the measurements are limited to 0.5 GHz by a low-pass filter on the board. These measured signals are referred to here has the TIS waveforms.

3.2.2 Filtering effects

After the signal is measured by the pickup, it, passes through a cable and lowpass filter to a digitizer. The response to this system was characterized by removing the cables from the pickups and inputting a harmonic of 80.5 MHz up to 483 MHz into the cables and recording the output of the digitizer. For this calibration, the TIS waveforms could not be recorded because that system requires the input signal to be phase locked to the 80.5 MHz global clock while the signal generator could only lock to a 5 MHz or 10 MHz clock. Instead the raw signal from the digitizer was recorded. The Fourier transforms of these signals were used

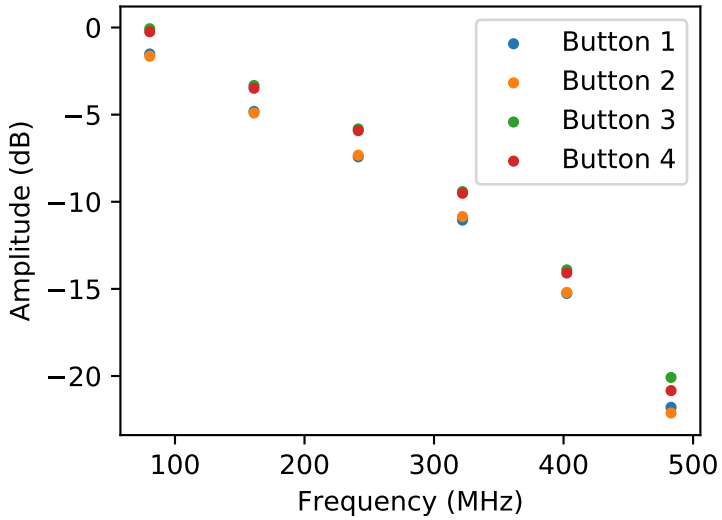

Figure 3.13: Cable and board calibration for four buttons on a BPM.

to determine the response for each harmonic. For any given input frequency, the harmonics of that frequency were also seen. The first higher harmonic at twice the input frequency was at least three orders of magnitude lower than the primary tone and ignored in the analysis. This calibration is stable within ±10% for tested BPMs.

The calibration of the four pickups on one of the FRIB BPMs is shown in Fig. 3.13. Note that two of the pickups are ∼ 1.5 dB lower than the other two. For these buttons, the signal processing board includes a switch for injecting signals which causes the reduction. All BPMs have these switches for two of the buttons and these must be correctly accounted for.

Only harmonics of 80.5 MHz were calibrated because, at the time the calibration was performed, the TIS waveforms could only measure harmonics of 80.5 MHz. The software was later updated to measure harmonics of 40.25 MHz. The uncalibrated 40.25 MHz harmonics, except for 40.25 MHz, are corrected using a cubic spline interpolation of the 80.5 MHz harmonics measurements. The 40.25 MHz harmonic was not used in measurements because

it could not be calibrated. These calibrations were only performed for the first nine warm BPMs near the RFQ including all four BPMs in the MEBT. For all other BPMs, the signals are approximately corrected using an average of these measurements and knowledge of the pickups with the switches.

3.2.3 Beamline measurements

Measurements of the BPM buttons signals were taken in the FRIB MEBT (Fig. 1.5). In this region the beam velocity is $\beta_r = 0.033$. The TIS waveforms were recorded for all four BPM in the MEBT which have a 47 mm diameter aperture and four, 20 mm diameter round pickups. However, most measurements of interest were taken with the third BPM because there is a wire profile monitor directly upstream of it and it is sufficiently downstream of a buncher cavity to cause variations in the bunch length. The TIS waveforms recorded harmonics of 40.25 MHz up to 483 MHz corresponding to a range of gR_p from 0.6 to 7.2.

The TIS waveform were taken to measure harmonics of 40.25 MHz, however the RF frequency of FRIB is 80.5 MHz. This is possible because, in single charge state operation, a prebuncher before the RFQ causes the bunches coming out of the RFQ only fill every other RF bucket. However, due to imperfect bunching, a small signal was seen in the bucket that was supposed to be empty. This causes the even harmonics of 40.25 MHz, i.e. the harmonics of 80.5 MHz, to be slightly higher than the odd harmonics (Fig. 3.14). The beamline was also operated without the prebuncher, in this case all RF buckets were filled and only the harmonics of 80.5 MHz are non-zero.

The raw TIS waveforms are corrected for the impedance and board effects (Fig. 3.15) then fit to Eq. 3.5 to determine the transverse and longitudinal sizes of the bunch. This fitting assumes the beam is Gaussian transversely and longitudinally with fit parameters x_0,

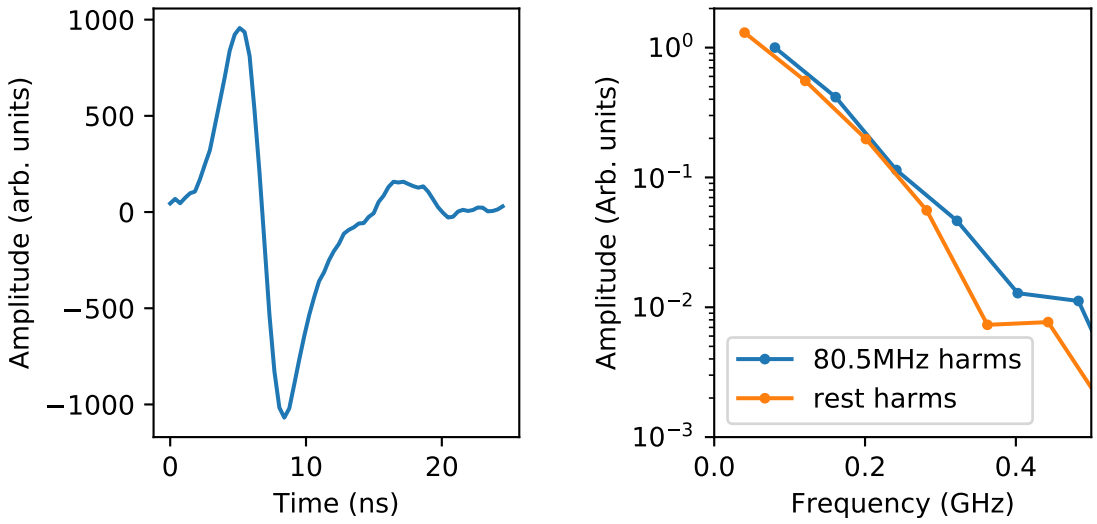

Figure 3.14: Example of a measured TIS waveform in the FRIB MEBT (left). The bump at 15 ns is a partially filled RF bucket. This causes the harmonics of 80.5 MHz to be higher than the rest of the harmonic of 40.25 MHz (right).

y_0, σ_x, σ_y, σ_{xy}, σ_z, an amplitude, and an offset to account for noise. Because the amplitude of each button depends on the transverse size and offset, all four button spectra must be fit simultaneously. The measured spectra in the MEBT fit within ±10% to Eq. 3.5 with differences primarily due to the discrepancy between the even and odd harmonics (Fig. 3.16).

3.2.4 RF buncher voltage scan

Measurements were taken with the third BPM in the MEBT for a range of voltages of the upstream buncher cavity with it set to a bunching phase to change the bunch length at the BPM. Along with the TIS waveforms, the transverse profiles were recorded with a wire profile scanner directly upstream of the BPM. The Fast Faraday Cup (FFC) located downstream of the third BPM could not be used to verify the longitudinal profile for most measurements because a Faraday cup at the same location needed to be inserted to act as a beam stop. Instead, simulations were used to compare the expected longitudinal size to

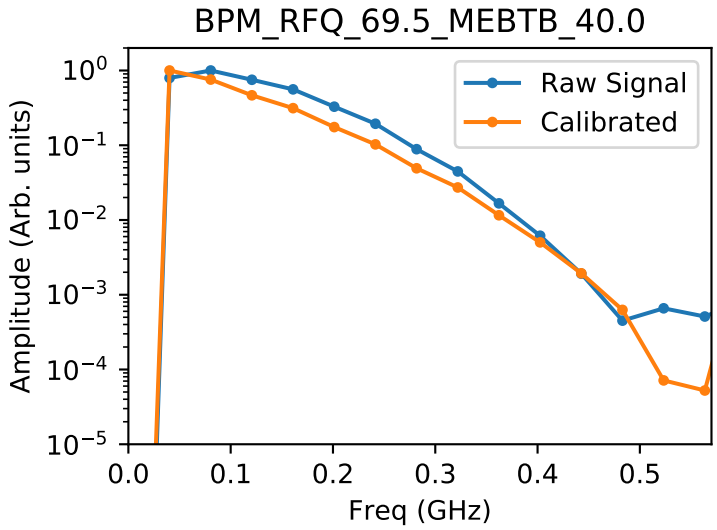

Figure 3.15: Raw and calibrated spectra of a BPM in the MEBT

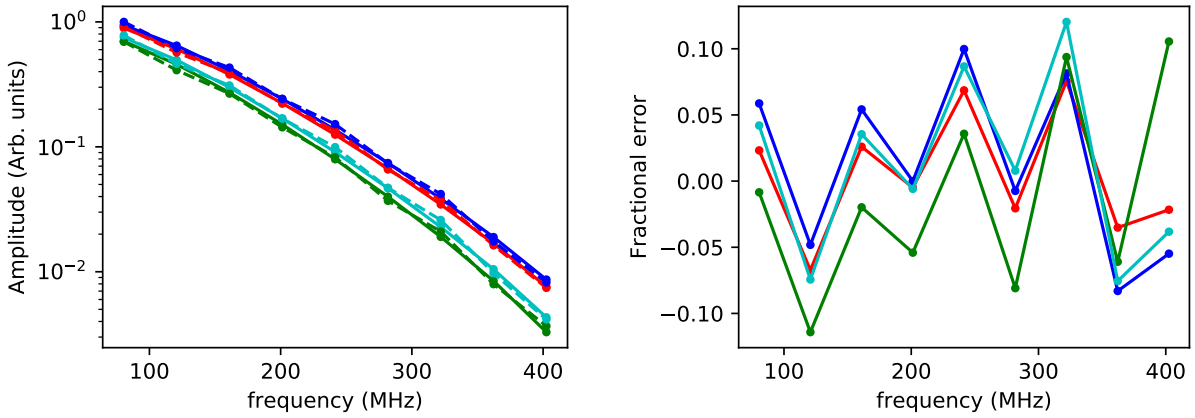

Figure 3.16: Fitting the measured spectra and fractional error from the measured values.

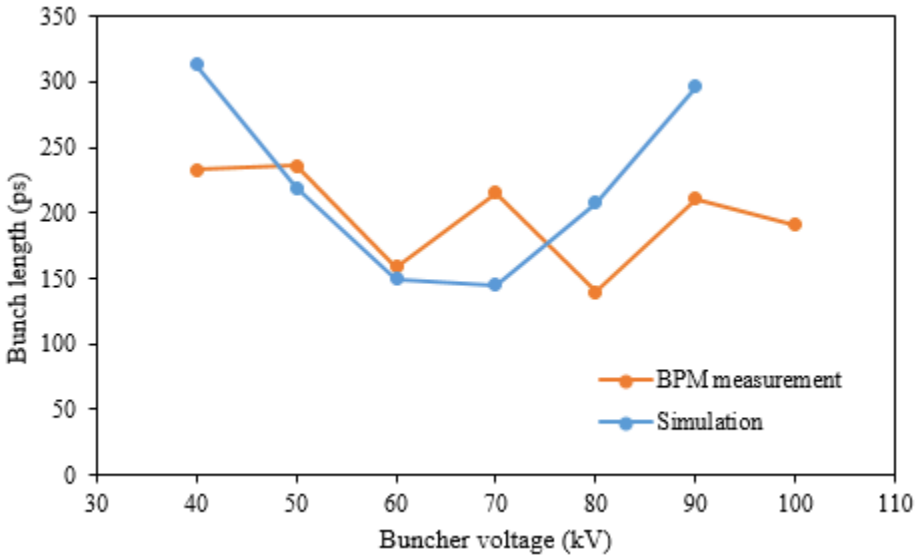

Figure 3.17: Comparison of the measured bunch length with simulations at the third BPM in the MEBT when the buncher cavity voltage is varied. The BPM measurement, while close to the expected values, fail to produced the expected trend.

the BPM measurements (Fig. 3.17). While the BPM measurements give longitudinal and transverse sizes on the same order as the simulation results, the longitudinal measurements fail to follow the expected trend from changing the buncher voltage.

To verify the simulation results, separate measurements were taken with the FFC for the same range of buncher voltages and they follow the expected trend of going through a minima. In addition the FFC measurements confirm that the longitudinal beam profile is primarily Gaussian.

The abnormal behavior of the BPM measurements is believed to be cased by the transverse distribution of the beam. Measurements of the transverse profile with the wire scanner clearly show clearly non-Gaussian profiles (Fig. 3.18), particularly in the vertical plane, while the fittings to the BPM measurements assumes a Gaussian distribution. The TIS waveforms were fit for harmonics of 40.25 MHz from 80.5 MHz up to 402.5 MHz corresponding to a range of gR_p from 1.2 to 6.0 and so the exact form of the transverse distribution will affect

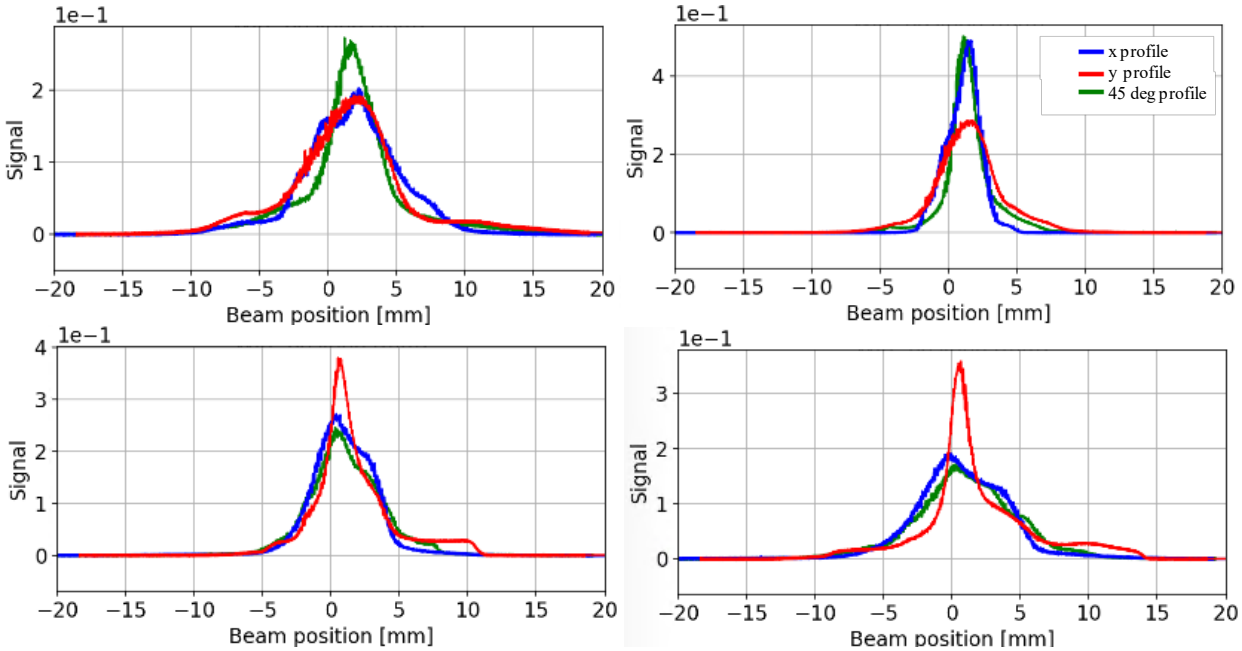

Figure 3.18: Examples of transverse profile measurement in the FRIB MEBT measured with a wire profile monitor.

the measured spectra. It was initially hoped that, while not exact, the Gaussian model would be capable of correctly approximating the second order moments. But, the buncher scan results showed this is not the case.

There exists a wire profile monitor directly upstream of the third BPM. It is possible to input the measured profiles from this scanner into Eq. 3.5 in order to fit the longitudinal profile. However, this procedure cannot be generally applied to the other BPM along the beamline because there are no measurements of the transverse distribution elsewhere. Varying an upstream quadrupole to change the transverse distribution at the third BPM in the MEBT resulted in a variety of measured transverse profiles at the BPM. Because of this, a better model of the transverse distribution to use in the fitting was not developed.

In an attempt to remove the transverse effects, the spectra were measured with BPMs at the end of the first accelerating linac segement of FRIB where the beam is traveling at $\beta_r = 0.185$ corresponding to a maximum gR_p of 1.07. This is sufficiently low to ignore the

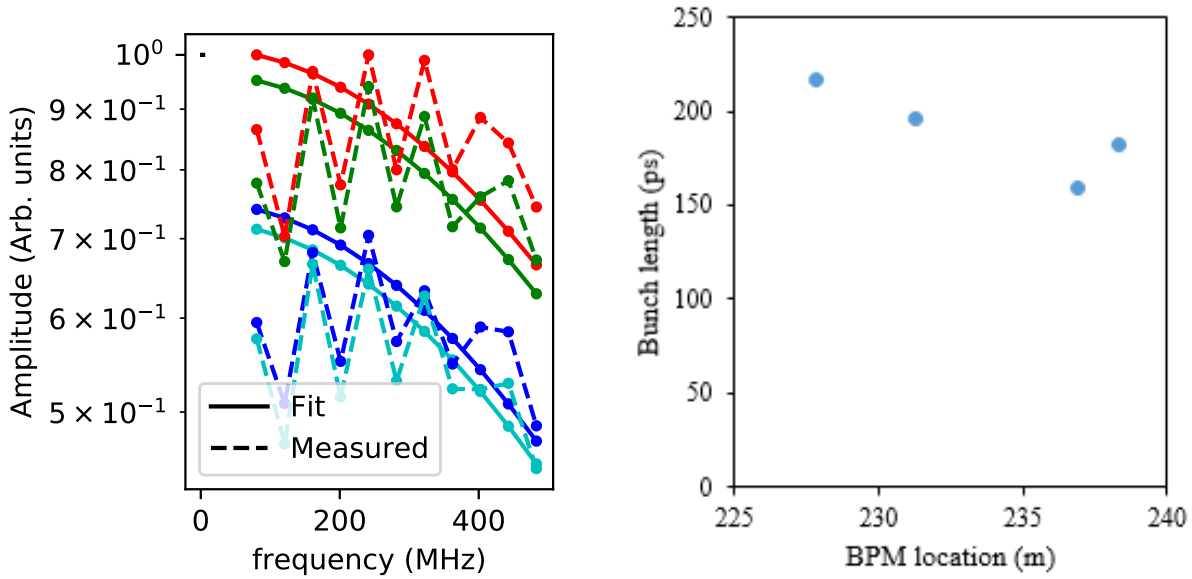

Figure 3.19: Spectra and fitting a pencil beam to measurements at $\beta = 0.185$. The droop at low frequency is hypothesized to be caused by incorrectly modeling the pickup impedance.

transverse distribution and assume a pencil beam. These measurements were taken with four BPMs and, based on simulations, the beam length should be linearly increasing across the four locations. The BPM measurements, once again, fail to reproduce the expected trend (Fig. 3.19 right).

It is suspected, that the averaged cable and board corrections were insufficient and/or the impedance of the BPM is not properly being compensated. The measured spectra, after corrections for the impedance and cable and board effects, retained a droop at low frequency (Fig. 3.19 left) which is a characteristic effect of the pickup impedance. In addition, the longitudinal profile was measured to be primarily Gaussian with a wire scanner in this region of the beamline which contradicts the BPM spectra.

3.3 Future work

Using the BPMs as transverse and longitudinal profile monitors is a complicated measurement particularly with the complex transverse profiles in the FRIB MEBT. However, one of the BPMs in the MEBT is directly downstream a wire profile monitor and it may be possible to directly input those transverse models into Eq. (3.5) and fit only for longitudinal bunch size. This method would only work for that single BPM and the profiles in the model would need to be continuously updated when the machine is retuned, e.g. for accelerating a different isotope. Another possibility for transverse profile measurements at high gR_p, is to apply this method to a different beamline that has cleaner distributions. For example, as shown in chapter 2, the beam is predominately Gaussian in the PIP2IT MEBT. In addition to further measurements, the analytic model should be further studied to understand how close the model to be to the beam distribution for reasonable errors.

At FRIB, TIS waveforms can be taken for BPMs in higher beam velocity, lower gR_p regions, where the effects from the transverse distribution should be damped out and a pencil can be assumed for fitting for the longitudinal size. However BMPs in this section of the accelerator were not calibrated for the effects of cable attenuation and low pass filtering and the average calibration was not sufficient. Once calibrations are performed on these BPMs, the measured signals should be able to be fit to determine the longitudinal size of the bunches.

In addition, the response BPM pickups to a beam as described in Eq. (3.5) makes some assumptions about the beam. Namely, it assumes the beam in mono-energetic and there is no longitudinal-transverse coupling. These affects should be included in the model and their effects characterized.

Chapter 4

Helical transmission line for BPM calibration

As shown in chapter 3, measurements with the BPMs of non-relativistic, high gR_p beams are more challenging than measurements at lower gR_p. These measurements are also challenging to study because we must rely on analytic and numeric models that, in practice, cannot exactly model the true BPM geometry. It would be beneficial for BPM measurements at high gR_p, both broadband measurements and position measurements, to have a test stand capable of calibrating and testing the BPMs' response in the high gR_p regime where they will be operated. In order to calibrate for the effects from non-relativistic, high gR_p beams, a test stand must be capable of replicating the measured beam's expected velocity and longitudinal profile and generate the correct field distribution on the BPM pickups. To calibrate and test the BPM signals expected from the beam in the FRIB MEBT, this requires replicating a 200 ps long bunch traveling at $\beta_r = 0.033$.

The typical test stand for calibrating for non-linearities in BPMs consists of a straight conducting wire that is strung through the BPM [5]. A tone at the measurement frequency of the BPM is passed down the wire and the signals on the pickups are measured. This is repeated while moving the wire over a grid of positions within the BPM. The wire position is then related to the pickup signals with a polynomial fitting to calibrate the BPM response.

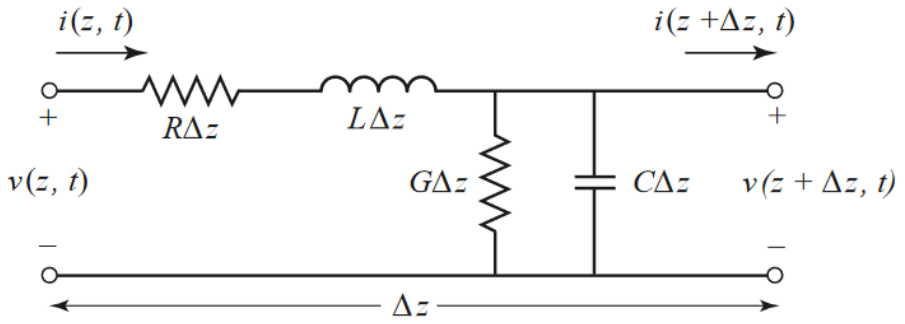

Figure 4.1: Circuit model of a transmission line [8].

Because these test stands rely on a straight wire, they propagate signals at the speed of light and cannot be used to calibrate for non-relativistic effects. These devices are still useful for BPM measurements of high gR_p beams to calibrate for the velocity independent non-linear effects and validate the models in the speed of light limit. To calibrate for the high gR_p effects, a new test stand must be developed capable of propagating signals at the same velocity as the beam in question.

4.1 Transmission lines primer

Before discussing possible test stand geometries, the basic properties of transmission lines should be introduced. Transmission lines are used to transport power and signals in the form of electromagnetic fields. They typically consist of two conductors that have a voltage difference between them $V(z,t)$ and a current travels along them $I(z,t)$. Over a small length Δz a transmission line can be approximated by a circuit with a series resistance per unit length R, series inductance per unit length L, shunt conductance per unit length G, and shunt capacitance per unit length C as shown in Fig. 4.1. Using Kirchhoff's laws the voltage and current can be shown to obey the equations [8]

$$V(z,t) - R\Delta z I(z,t) - L\Delta z \frac{\partial I(z,t)}{\partial t} - V(z+\Delta z,t) = 0 \tag{4.1}$$

$$I(z,t) - G\Delta z V(z+\Delta z,t) - C\Delta z \frac{\partial V(z+\Delta z,t)}{\partial t} - I(z+\Delta z,t) = 0. \tag{4.2}$$

The continuous limit, known as the telegrapher equations, can be found by dividing by Δz and taking the limit as $\Delta z \to 0$

$$\frac{\partial V}{\partial z} = -RI - L\frac{\partial I}{\partial t} \tag{4.3}$$

$$\frac{\partial I}{\partial z} = -GV - C\frac{\partial V}{\partial t}. \tag{4.4}$$

For an RF field $V(z,t) = \bar{V}(z)e^{i\omega t}$ and $I(z,t) = \bar{I}(z)e^{i\omega t}$. In this case the telegrapher equations become

$$\frac{\partial \bar{V}}{\partial t} = -(R + i\omega L)\bar{I} \tag{4.5}$$

$$\frac{\partial \bar{I}}{\partial t} = -(C + i\omega C)\bar{V} \tag{4.6}$$

Taking a derivative with respect to t gives the wave equations

$$\frac{\partial^2 \bar{V}}{\partial t^2} - \gamma^2 \bar{V} = 0 \tag{4.7}$$

$$\frac{\partial^2 \bar{I}}{\partial t^2} - \gamma^2 \bar{I} = 0 \tag{4.8}$$

where γ is the propagation constant

$$\gamma = \alpha + ih = \sqrt{(R + i\omega L)(G + i\omega G)}. \tag{4.9}$$

The electromagnetic fields will propagate along the transmission line with phase velocity

$$v_p = \frac{\omega}{h}. \tag{4.10}$$

The wave equations shows voltage and current oscillate with z i.e. $\bar{V}(z) = V_0 e^{-\gamma z}$ and $\bar{I}(z) = I_0 e^{-\gamma z}$. The current and voltage can be related by plugging this form into the telegrapher equations resulting in

$$\bar{V}(z) = Z\bar{I}(z) \tag{4.11}$$

where Z is the impedance of the transmission line

$$Z = \sqrt{\frac{R + i\omega L}{G + i\omega C}}. \tag{4.12}$$

For the case of a lossless transmission line $R = G = 0$. In this case the the phase velocity and impedance become frequency independent

$$v_p = \frac{1}{\sqrt{LC}} \tag{4.13}$$

$$Z = \sqrt{\frac{L}{C}}. \tag{4.14}$$

This formalization of the behavior of a transmission line requires knowledge of the circuit elements L, C, R, and G. For an arbitrary geometry of conductors, it can be non-obvious how to directly determine these. Instead, it can be more straight forward to derive the form of the electromagnetic fields first. For a geometry with two conductors with one nested inside

the other, one method for doing this is using the Hertzian potentials [54]

$$\nabla^2 \mathbf{\Pi_e} - \mu\epsilon \frac{\partial^2 \mathbf{\Pi_e}}{\partial t^2} = 0 \tag{4.15}$$

$$\nabla^2 \mathbf{\Pi_m} - \mu\epsilon \frac{\partial^2 \mathbf{\Pi_m}}{\partial t^2} = 0. \tag{4.16}$$

If $\mathbf{\Pi_e}$ and $\mathbf{\Pi_m}$ are assumed to only have a $\hat{z}$ component, then the fields are given by

$$\mathbf{E} = \nabla \times \nabla \times \mathbf{\Pi_e} - \nabla \times \frac{\partial^2 \mathbf{\Pi_m}}{\partial t^2} \tag{4.17}$$

$$\mathbf{H} = \nabla \times \nabla \times \mathbf{\Pi_m} - \nabla \times \frac{\partial^2 \mathbf{\Pi_e}}{\partial t^2}. \tag{4.18}$$

One of the benefits of this method is transverse electric (TE) and transverse magnetic (TM) modes naturally appear. For example, if $\mathbf{\Pi_e} = 0$ but $\mathbf{\Pi_m}$ does not, then $E_z = 0$ corresponding to a TE mode. Similarly if $\mathbf{\Pi_m} = 0$ then the resulting field will be a TM mode.

With the nested conductor geometry, a cylindrical coordinates system can often be used. In cylindrical coordinates with a dielectric between the two conductors with permittivity ϵ

and permeability μ, the general field equations from Hertzian potentials are

$$E_r = \Big[-ih\gamma\left(\mathrm{I}_n'(\gamma r)\,A_n^{(1)} + \mathrm{K}_n'(\gamma r)\,A_n^{(2)}\right) - \frac{\omega\mu n}{r}\left(\mathrm{I}_n(\gamma r)\,B_n^{(1)} + \mathrm{K}_n(\gamma r)\,B_n^{(2)}\right)\Big] e^{-in\theta}e^{-ihz} \tag{4.19}$$

$$E_\theta = \Big[-\frac{hn}{r}\left(\mathrm{I}_n(\gamma r)\,A_n^{(1)} + \mathrm{K}_n(\gamma r)\,A_n^{(2)}\right) + i\omega\mu\gamma\left(\mathrm{I}_n'(\gamma_e r)\,B_n^{(1)} + \mathrm{K}_n'(\gamma r)\,B_n^{(2)}\right)\Big] e^{-in\theta}e^{-ihz} \tag{4.20}$$

$$E_z = -\gamma^2\left[\mathrm{I}_n(\gamma r)\,A_n^{(i)} + \mathrm{K}_n(\gamma r)\,A_n^{(2)}\right] e^{-in\theta}e^{-ihz} \tag{4.21}$$

$$H_r = \Big[\frac{\omega\epsilon n}{r}\left(\mathrm{I}_n(\gamma r)\,A_n^{(1)} + \mathrm{K}_n(\gamma r)\,A_n^{(2)}\right) - ih\gamma\left(\mathrm{I}_n'(\gamma r)\,B_n^{(1)} + \mathrm{K}_n'(\gamma r)\,B_n^{(2)}\right)\Big] e^{-in\theta}e^{-ihz} \tag{4.22}$$

$$H_\theta = \Big[-i\omega\epsilon\gamma\left(\mathrm{I}_n'(\gamma r)\,A_n^{(1)} + \mathrm{K}_n'(\gamma r)\,A_n^{(2)}\right) - \frac{hn}{r}\left(\mathrm{I}_n(\gamma r)\,B_n^{(1)} + \mathrm{K}_n(\gamma r)\,B_n^{(2)}\right)\Big] e^{-in\theta}e^{-ihz} \tag{4.23}$$

$$H_z = -\gamma^2\left[\mathrm{I}_n(\gamma r)\,B_n^{(1)} + \mathrm{K}_n(\gamma r)\,B_n^{(2)}\right] e^{-in\theta}e^{-ihz} \tag{4.24}$$

where I_n and K_n are the modified Bessel functions of the first and second kind [21], primes denote derivatives with respect to the argument, n is the azimuthal harmonic number, and γ and h are the transverse and longitudinal propagation constants respectively and are related by

$$h^2 = k^2 + \gamma^2 \tag{4.25}$$

where $k = \sqrt{\mu\epsilon}\omega$ is the free space propagation constant. The field coefficients $A_n^{(1)}$, $A_n^{(2)}$, $B_n^{(1)}$, and $B_n^{(2)}$ are found by applying the boundary conditions at the conductors.

From the fields the current I can be determined from Biot-Savart law and voltage V can be determined by integrating the electric field between the conductors. These can be

used to determine the impedance. In addition the circuit elements R, L, C, and G can be determined by

$$L = \frac{\mu}{|I|^2} \int_S |\mathbf{H}|^2 \mathrm{d}s \tag{4.26}$$

$$C = \frac{\epsilon}{|V|^2} \int_S |\mathbf{E}|^2 \mathrm{d}s \tag{4.27}$$

$$R = \frac{R_s}{|I|^2} \int_{C_1+C_2} |\mathbf{H}|^2 \mathrm{d}\ell \tag{4.28}$$

$$G = \frac{\omega\epsilon''}{|I|^2} \int_S |\mathbf{E}|^2 \mathrm{d}s \tag{4.29}$$

where S is the cross sectional area of the transmission line, C_1 and C_2 and the curves defining the boundaries of the two conductors, R_s is the surface resistance, and $\epsilon = \epsilon' - i\epsilon''$ [8].

4.2 Initially considered test stand geometries

To create a test stand capable of replicating non-relativistic beams it is possible to use an electron beam tuned to match the velocity and shape of the desired beam. However, this relies on an entirely new test stand from the currently existing straight wire one which requires additional hardware and cost. It would be preferable to modify the existing test stand to allow for calibration for non-relativistic effects.

A possible RF structure to replace the straight wire is a Goubau line which can propagate signals at less than the speed of light and can be used to replicate electron beams to calibrate beamline devices [55, 56, 57]. Goubau lines are single conductor transmission lines comprised of a conducting wire of radius R_i covered in a dielectric with radius a and permittivity ϵ_i (Fig. 4.2). This dielectric layer causes a surface wave to propagate at less than the speed of light. The dispersion relation for a Goubau line in a dielectric ϵ_e and centered in a conducting

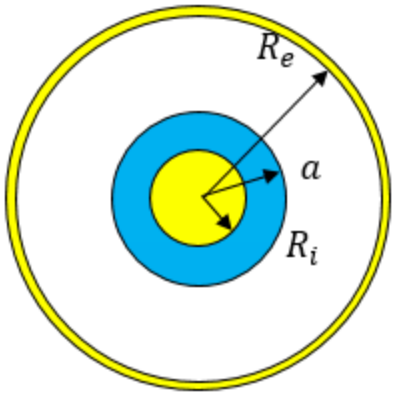

Figure 4.2: Cross section of a Goubau line.

pipe of radius R_e is

$$\frac{\gamma_i}{\epsilon_i}\frac{I_0(\gamma_i R_i)K_0(\gamma_i a) - I_0(\gamma_i a)K_0(\gamma_i R_i)}{I_0(\gamma_i R_i)K_1(\gamma_i a) + I_1(\gamma_i a)K_0(\gamma_i R_i)} = \frac{\gamma_e}{\epsilon_e}\frac{I_0(\gamma_e R_e)K_0(\gamma_e a) - I_0(\gamma_e a)K_0(\gamma_e R_e)}{I_0(\gamma_e R_e)K_1(\gamma_e a) + I_1(\gamma_e a)K_0(\gamma_e R_e)} \tag{4.30}$$

where γ_i and γ_e are the transverse propagation constants in the dielectric and outside the dielectric respectively. This is found following the same steps shown in section 4.4 and using the appropriate boundary conditions. The longitudinal propagation constant h is found by

$$h^2 = \gamma_i^2 + k_i^2 = \gamma_e^2 + k_e^2 \tag{4.31}$$

The dispersion relation is used to relate the longitudinal propagation constant to the frequency. If h is linear with frequency, i.e. $h = a\omega$, then the phase velocity will be constant and the transmission line is said to be dispersion free. If the relation is non-linear, then the phase velocity will vary with frequency and the transmission line is disperive.

For the Gaubou line, assuming $\epsilon_e = \epsilon_0$, the high frequency limit of the phase velocity $v_p = c/\sqrt{\epsilon_i}$ which it reaches when $\lambda \approx a$. In order to achieve a phase velocity of $v_p = 0.033c$, a material with a dielectric constant of $\sim$900 must be used which is impractical. In addition,

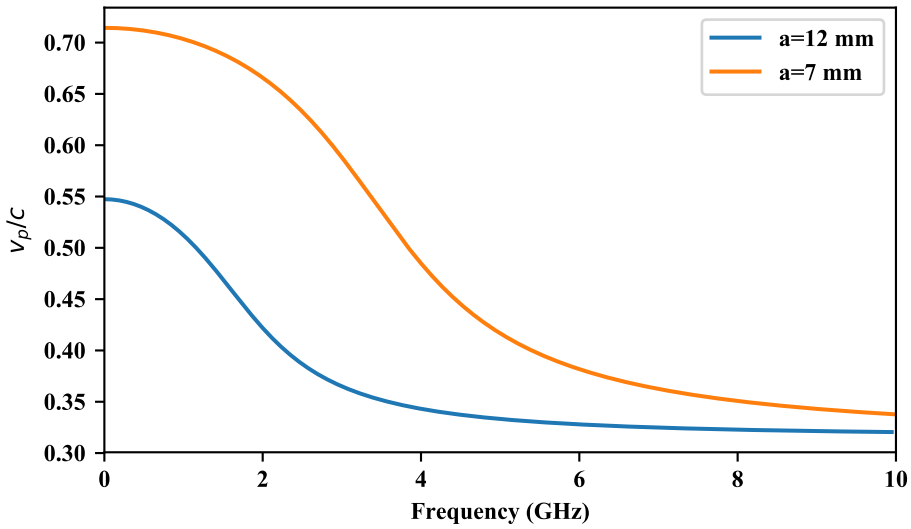

Figure 4.3: Normalized phase velocity of a Gaubou line with R_i=2 mm, R_e=20 mm, ϵ_i=10ϵ_0, and two different dielectric layer radii a. The low frequency limit is too large to replicate a non-relativistic beam.

the low frequency limit is significantly larger than the high frequency limit (Fig. 4.3). To calibrate the broadband measurements of the BPMs, the phase velocity must match the beam within the measured bandwidth, e.g. up to 0.5 GHz for the FRIB BPMs. The low frequency limit can be reduced by increasing a, however, even when the dielectric layer fills a significant portion of the beampipe, the reduction is not enough to reach non-relativistic phase velocities.

4.3 Helical RF structures

An RF structure that is known to be capable of propagating at sufficiently low phase velocities is a helical transmission line. The low phase velocity of helices is relied on for devices such as slow traveling wave tubes for RF power amplifiers [58] and the fast kickers for PIP-II [59]. There are many applications of helical RF structures, however, many concern radiation modes for antennae [60] or transmission lines for signal propagation at 10s to 100s of GHz

[61]. General solutions have also been published (e.g. [62, 63]), however, most solution focus on deriving impedance, dispersion, and radiation properties of these structures. For the desired test stand, the largest concern is the behavior of the electric fields as they propagate along the helix because they must replicate the fields generated by a beam.

The general solutions can provide insights into the challenges of using a helical transmission line at lower frequencies. The dispersion relation for a helix in free space [62] shows the high frequency limit of the phase velocity is $v_p = c \cdot \sin(\psi)$ where ψ is the pitch angle of the helix. This allows these structures to be created for any desired phase velocity by constructing a helix with the correct ψ, however the low frequency limit of the phase velocity of a helix in free space is the speed of of light [62]. Many uses of helical transmission lines can ignore this effects because they operate at high enough frequencies where the phase velocity has reached its high frequency limit. However, this clearly will not replicate the velocity of a non-relativistic beam within the desired frequency band and, in addition, the large discrepancy between the high and low frequency limits quickly causes the input pulse to deform due to dispersion making replicating the correct bunch shape challenging. These effects will affect the lower frequency transmission line and steps must be taken to mitigate this issue.

4.4 Helical transmission lines - analytic solution

The geometry of a helical conductor makes exactly solving for the electromagnetic fields challenging. However, the boundary conditions can be significantly simplified using the sheath helix model [62]. This model approximates a helix as an infinitesimally thin cylinder that conducts on a helical path along the surface making the structure a 1D conductor that

is longitudinally uniform. Specifically, the boundary conditions at the helix become

$$E_{i,\parallel} = E_{e,\parallel} = 0 \tag{4.32}$$

$$E_{i,\perp} = E_{e,\perp} \tag{4.33}$$

$$H_{i,\parallel} = H_{e,\parallel} \tag{4.34}$$

where the subscripts e and i denote fields in the external and internal regions of the helix and the subscripts $\parallel$ and $\perp$ denote the field components parallel and perpendicular to the direction of conductivity of the sheath helix. These unit vectors in cylindrical coordinates are

$$\hat{\parallel} = \sin(\psi)\hat{z} + \cos(\psi)\hat{\theta} \tag{4.35}$$

$$\hat{\perp} = \cos(\psi)\hat{z} + \sin(\psi)\hat{\theta} \tag{4.36}$$

where ψ is the pitch angle of the helix. While this model is an abstraction from real helix, it is shown below that it well represents the tightly wound helices needed to replicate non-relativistic beams.

The transmission line for the test stand consists of a helix of radius a and pitch ψ, a conducting rod of radius R_i centered inside of the helix, a dielectric with permittivity ϵ_i of thickness $s = a - R_i$ fills the space between the rod and the helix to support the helix, and the helix is centered inside a conducting pipe of radius R_e. The analytic solution also assumes the region between the helix and the outer conductor is filled with a dielectric with permittivity ϵ_e; however, this is set to ϵ_0 for all studies (Fig. 4.4).

The derivation of the electromagnetic fields presented here follows the work of S. Sensiper

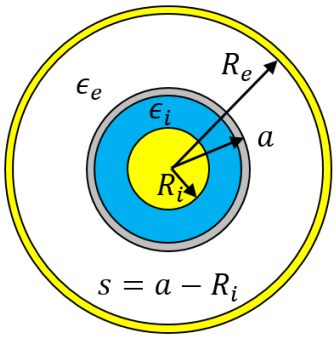

Figure 4.4: Cross section of helical transmission line geometry. The grey circle represents the helix.

[62] and others [63] starting with the Hertzian potentials, Eqs. 4.15 and 4.16

In this geometry the fields must be defined in the internal region, between the inner conductor and the helix, and the external region, between the helix and outer conductor. The general field equations in the internal region are

$$E_{i,r} = \left[-ih\gamma_i \left(\mathrm{I}'_n(\gamma_i r) A^{(1)}_{i,n} + \mathrm{K}'_n(\gamma_i r) A^{(2)}_{i,n}\right) - \frac{\omega\mu n}{r}\left(\mathrm{I}_n(\gamma_i r) B^{(1)}_{i,n} + \mathrm{K}_n(\gamma_i r) B^{(2)}_{i,n}\right)\right] e^{-in\theta} e^{-ihz} \tag{4.37}$$

$$E_{i,\theta} = \left[-\frac{hn}{r}\left(\mathrm{I}_n(\gamma_i r) A^{(1)}_{i,n} + \mathrm{K}_n(\gamma_i r) A^{(2)}_{i,n}\right) + i\omega\mu\gamma_i \left(\mathrm{I}'_n(\gamma_i r) B^{(1)}_{i,n} + \mathrm{K}'_n(\gamma_i r) B^{(2)}_{i,n}\right)\right] e^{-in\theta} e^{-ihz} \tag{4.38}$$

$$E_{i,z} = -\gamma_i^2 \left[\mathrm{I}_n(\gamma_i r) A^{(i)}_{i,n} + \mathrm{K}_n(\gamma_i r) A^{(2)}_{i,n}\right] e^{-in\theta} e^{-ihz} \tag{4.39}$$

$$H_{i,r} = \left[\frac{\omega\epsilon_i n}{r}\left(\mathrm{I}_n(\gamma_i r) A^{(1)}_{i,n} + \mathrm{K}_n(\gamma_i r) A^{(2)}_{i,n}\right) - ih\gamma_i \left(\mathrm{I}'_n(\gamma_i r) B^{(1)}_{i,n} + \mathrm{K}'_n(\gamma_i r) B^{(2)}_{i,n}\right)\right] e^{-in\theta} e^{-ihz} \tag{4.40}$$

$$H_{i,\theta} = \left[-i\omega\epsilon_i\gamma_i \left(\mathrm{I}'_n(\gamma_i r) A^{(1)}_{i,n} + \mathrm{K}'_n(\gamma_i r) A^{(2)}_{i,n}\right) - \frac{hn}{r}\left(\mathrm{I}_n(\gamma_i r) B^{(1)}_{i,n} + \mathrm{K}_n(\gamma_i r) B^{(2)}_{i,n}\right)\right] e^{-in\theta} e^{-ihz} \tag{4.41}$$

$$H_{i,z} = -\gamma_i^2 \left[\mathrm{I}_n(\gamma_i r) B^{(1)}_{i,n} + \mathrm{K}_n(\gamma_i r) B^{(2)}_{i,n}\right] e^{-in\theta} e^{-ihz} \tag{4.42}$$

where I_n and K_n are the modified Bessel functions of the first and second kind and γ_i and h_i are the transverse and longitudinal propagation constants respectively and are related by

$$h^2 = k_i^2 + \gamma_i^2 = k_e^2 + \gamma_e^2 \tag{4.43}$$

where $k_i = \sqrt{\mu\epsilon_i}\omega$ is the free space propagation constant. The external fields have the same form except with different propagation constants and coefficients and are denoted by exchanging the subscript i for e.

The field coefficients $A_{i,n}^{(1)}$, $A_{i,n}^{(2)}$, $A_{e,n}^{(1)}$, $A_{e,n}^{(2)}$, $B_{i,n}^{(1)}$, $B_{i,n}^{(2)}$, $B_{e,n}^{(1)}$, and $B_{e,n}^{(2)}$ are found by applying the boundary conditions at the helix (Eqs. 4.32, 4.33, 4.34) and the inner and outer conducting surfaces. The boundary conditions in cylindrical coordinates at the conductors and the sheath helix are

$$E_{i,z}\big|_{R_i} = 0 \tag{4.44}$$

$$E_{i,\theta}\big|_{R_i} = 0 \tag{4.45}$$

$$H_{i,r}\big|_{R_i} = 0 \tag{4.46}$$

$$E_{e,z}\big|_{R_e} = 0 \tag{4.47}$$

$$E_{e,\theta}\big|_{R_e} = 0 \tag{4.48}$$

$$H_{e,r}\big|_{R_e} = 0 \tag{4.49}$$

$$H_{i,z}\big|_a + H_{i,\theta}\big|_a \cot(\psi) = H_{e,z}\big|_a + H_{e,\theta}\big|_a \cot(\psi) \tag{4.50}$$

$$H_{i,r}\big|_a = H_{e,r}\big|_a \tag{4.51}$$

$$E_{i,z}\big|_a = E_{e,z}\big|_a \tag{4.52}$$

$$E_{i,\theta}\big|_a = E_{e,\theta}\big|_a \tag{4.53}$$

$$E_{e,z}\big|_a = -E_{e,\theta}\big|_a \cot(\psi) \tag{4.54}$$

$$E_{i,z}\big|_a = -E_{i,\theta}\big|_a \cot(\psi), \tag{4.55}$$

Only a linearly independent subset of the boundary conditions are needed to solve for the field coefficients. Using $A_{i,n}^{(1)}$ as an overall amplitude and Eqs. 4.44, 4.46, 4.48, 4.49, 4.50, 4.52, and 4.53 the field coefficients become:

$$A_{i,n}^{(2)} = -A_{i,n}^{(1)} \cdot \frac{\mathrm{I}_n(\gamma_i R_i)}{\mathrm{K}_n(\gamma_i R_i)} \tag{4.56}$$

$$A_{e,n}^{(2)} = -A_{e,n}^{(1)} \cdot \frac{\mathrm{I}_n(\gamma_e R_e)}{\mathrm{K}_n(\gamma_e R_e)} \tag{4.57}$$

$$A_{e,n}^{(1)} = A_{i,n}^{(1)} \cdot \frac{\gamma_i^2}{\gamma_e^2} \frac{K_n(\gamma_e R_e) w_{1,i}}{K_n(\gamma_i R_i) w_{1,e}} \tag{4.58}$$

$$B_{i,n}^{(2)} = -B_{i,n}^{(1)} \cdot \frac{\mathrm{I}_n'(\gamma_i R_i)}{\mathrm{K}_n'(\gamma_i R_i)} \tag{4.59}$$

$$B_{e,n}^{(2)} = -B_{e,n}^{(1)} \cdot \frac{\mathrm{I}_n'(\gamma_e R_e)}{\mathrm{K}_n'(\gamma_e R_e)} \tag{4.60}$$

$$\begin{aligned} B_{i,n}^{(1)} = -iA_{i,n}^{(1)} \cdot \Bigg[& a^2 \gamma_i \gamma_e^2 \mathrm{K}_n'(\gamma_i R_i) w_{4,e} \left(\gamma_i k_e^2 w_{1,i} w_{2,e} - \gamma_e k_i^2 w_{1,e} w_{2,i} \right) \\ & - nhw_{1,i} w_{1,e} w_{3,e} \mathrm{K}_n'(\gamma_i R_i) \left(nh\cot(\psi) + a\gamma_e^2 \right) \left(\gamma_i^2 - \gamma_e^2 \right) \Bigg] \times \\ & \Bigg\{ a\mu\omega\gamma_e^2 \mathrm{K}_n(\gamma_i R_i) w_{1,e} \times \\ & \left[\gamma_i \left(nh\cot(\psi) + a\gamma_e^2 \right) w_{3,e} w_{4,i} - \gamma_e \left(nh\cot(\psi) + a\gamma_i^2 \right) w_{3,i} w_{4,e} \right] \Bigg\}^{-1} \end{aligned} \tag{4.61}$$

$$\begin{aligned} B_{e,n}^{(1)} = B_{i,n}^{(1)} \cdot \Bigg[& a^2 \gamma_i^2 \gamma_e \mathrm{K}_n'(\gamma_e R_e) w_{4,i} \left(\gamma_i k_e^2 w_{1,i} w_{2,e} - \gamma_e k_i^2 w_{1,e} w_{2,i} \right) \\ & - nhw_{1,i} w_{1,e} w_{3,i} \mathrm{K}_n'(\gamma_e R_e) \left(nh\cot(\psi) + a\gamma_i^2 \right) \left(\gamma_i^2 - \gamma_e^2 \right) \Bigg] \times \\ & \Bigg[a^2 \gamma_e \gamma_i^2 \mathrm{K}_n'(\gamma_i R_i) w_{4,e} \left(\gamma_i k_e^2 w_{1,i} w_{2,e} - \gamma_e k_i^2 w_{1,e} w_{2,i} \right) \\ & - nhw_{1,i} w_{1,e} w_{3,e} \mathrm{K}_n'(\gamma_i R_i) \left(nh\cot(\psi) + a\gamma_e^2 \right) \left(\gamma_i^2 - \gamma_e^2 \right) \Bigg]^{-1} \end{aligned} \tag{4.62}$$

where

$$w_{1,i,e} = \mathrm{I}_n\left(\gamma_{i,e}a\right)\mathrm{K}_n\left(\gamma_{i,e}R_{i,e}\right) - \mathrm{I}_n\left(\gamma_{i,e}R_{i,e}\right)\mathrm{K}_n\left(\gamma_{i,e}a\right) \tag{4.63}$$

$$w_{2,i,e} = \mathrm{I}'_n\left(\gamma_{i,e}a\right)\mathrm{K}_n\left(\gamma_{i,e}R_{i,e}\right) - \mathrm{I}_n\left(\gamma_{i,e}R_{i,e}\right)\mathrm{K}'_n\left(\gamma_{i,e}a\right) \tag{4.64}$$

$$w_{1,i,e} = \mathrm{I}_n\left(\gamma_{i,e}a\right)\mathrm{K}'_n\left(\gamma_{i,e}R_{i,e}\right) - \mathrm{I}'_n\left(\gamma_{i,e}R_{i,e}\right)\mathrm{K}_n\left(\gamma_{i,e}a\right) \tag{4.65}$$

$$w_{1,i,e} = \mathrm{I}'_n\left(\gamma_{i,e}a\right)\mathrm{K}'_n\left(\gamma_{i,e}R_{i,e}\right) - \mathrm{I}'_n\left(\gamma_{i,e}R_{i,e}\right)\mathrm{K}'_n\left(\gamma_{i,e}a\right). \tag{4.66}$$

The dispersion relation can be found by creating a matrix from the boundary conditions used to determine the field coefficients and setting the determinant to 0.

$$\begin{vmatrix}
0 & 0 & I_n(\gamma_e R_e) & K_n(\gamma_e R_e) \\
0 & 0 & \frac{n\epsilon_e\omega}{R_e} I_n(\gamma_e R_e) & \frac{n\epsilon_e\omega}{R_e} K_n(\gamma_e R_e) \\
I_n(\gamma_i R_i) & K_n(\gamma_i R_i) & 0 & 0 \\
\frac{n\epsilon_i\omega}{R_i} I_n(\gamma_i R_i) & \frac{n\epsilon_i\omega}{R_i} K_n(\gamma_i R_i) & 0 & 0 \\
-i\omega\cot(\psi)\gamma_i\epsilon_i I'_n(\gamma_i a) & -i\omega\cot(\psi)\gamma_i\epsilon_i K'_n(\gamma_i a) & i\omega\cot(\psi)\gamma_e\epsilon_e I'_n(\gamma_e a) & i\omega\cot(\psi)\gamma_e\epsilon_e K'_n(\gamma_e a) \\
0 & 0 & -\left(\gamma_e^2 + \frac{nh}{a}\cot(\psi)\right) I_n(\gamma_e a) & -\left(\gamma_e^2 + \frac{nh}{a}\cot(\psi)\right) K_n(\gamma_e a) \\
-\gamma_i^2 I_n(\gamma_i a) & -\gamma_i^2 K_n(\gamma_i a) & \gamma_e^2 I_n(\gamma_e a) & \gamma_e^2 K_n(\gamma_e a) \\
-\frac{nh}{a} I_n(\gamma_i a) & -\frac{nh}{a} K_n(\gamma_i a) & \frac{nh}{a} I_n(\gamma_e a) & \frac{nh}{a} K_n(\gamma_e a)
\end{vmatrix}$$

$$\begin{vmatrix}
0 & 0 & 0 & 0 \\
0 & 0 & -ih\gamma_e I'_n(\gamma_e R_e) & -ih\gamma_e I'_n(\gamma_e R_e) \\
0 & 0 & 0 & 0 \\
-ih\gamma_i I'_n(\gamma_i R_i) & ih\gamma_i K'_n(\gamma_i R_i) & 0 & 0 \\
-\left(\gamma_i^2 + \frac{nh}{a}\cot(\psi)\right) I_n(\gamma_i a) & -\left(\gamma_i^2 + \frac{nh}{a}\cot(\psi)\right) K_n(\gamma_i a) & \left(\gamma_e^2 + \frac{nh}{a}\cot(\psi)\right) I_n(\gamma_e a) & \left(\gamma_e^2 + \frac{nh}{a}\cot(\psi)\right) K_n(\gamma_e a) \\
0 & 0 & i\mu\omega\cot(\psi)\gamma_e I'_n(\gamma_e a) & i\mu\omega\cot(\psi)\gamma_e K'_n(\gamma_e a) \\
0 & 0 & 0 & 0 \\
i\mu\omega\gamma_i I_n(\gamma_i a) & i\mu\omega\gamma_i K_n(\gamma_i a) & -i\mu\omega\gamma_e I_n(\gamma_e a) & -i\mu\omega\gamma_e I_n(\gamma_e a)
\end{vmatrix} = 0 \tag{4.67}$$

After simplification the dispersion relation is

$$\begin{aligned} 0 =& \gamma_i^3 \left[nh\cot(\psi) + a\gamma_e^2 \right]^2 w_{1,i} w_{1,e} w_{3,e} w_{4,i} + \gamma_e^3 \left[nh\cot(\psi) + a\gamma_i^2 \right]^2 w_{1,i} w_{1,e} w_{3,i} w_{4,e} \\ &+ a^2 \cot^2(\psi) \gamma_e^2 \gamma_i^2 w_{4,i} w_{4,e} \left(\gamma_e k_i^2 w_{1,e} w_{2,i} - \gamma_i k_e^2 w_{1,i} w_{2,e} \right). \end{aligned} \tag{4.68}$$

This is solved numerically for γ_e as a function of k_e using

$$\gamma_e^2 = \gamma_i^2 + k_i^2 - k_e^2 \tag{4.69}$$

and then $h(\omega)$ can be determined along with the phase velocity $v_p(\omega) = k_e/h = \beta c$.

4.4.1 Dispersion distortion correction

In order to produce the specific pulse shape at the device under test, it is ideal for the transmission line to be dispersion free so any pulse input into the transmission line will not be deformed throughout propagation. However, for a helix in free space, the phase velocity varies from $\beta = 1$ to $\beta = \sin(\psi)$ which causes significant deformation to the input pulse. For many applications the helix is inside of pipe (e.g. for RF power amplifiers [58]), and initial designs of the test stand added a conducting pipe around the helix. For this geometry, the low frequency limit of the phase velocity is significantly less than $\beta = 1$. For example for the parameters given for Fig. 4.7, the high frequency limit is $v_p = 0.05c$ and low frequency limit is $v_p = 0.09c$. However, the deformation due to dispersion is still a major issue with significant deformation to the pulse shape seen even for relatively short propagation distances (see Fig. 4.5).

One method to mitigate the deterioration is to use dispersion itself to correct the pulse

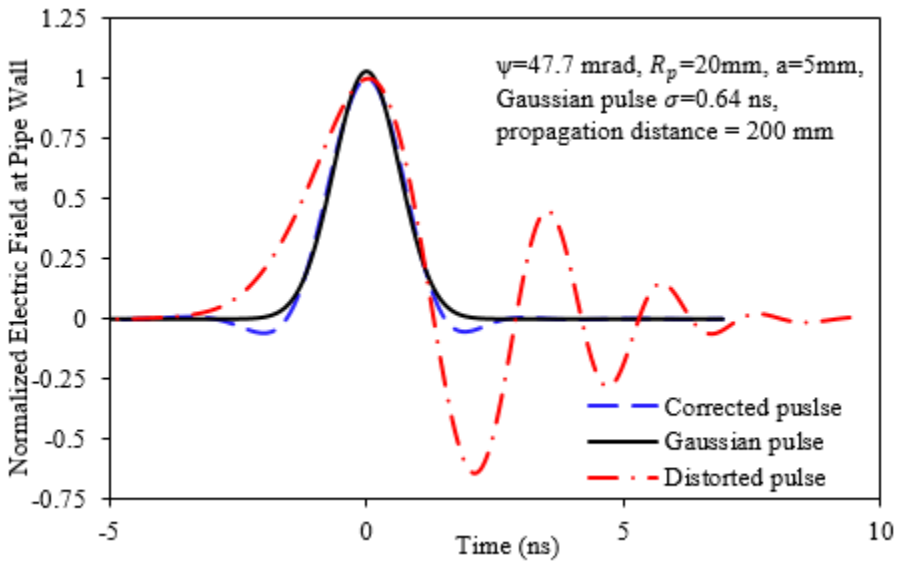

Figure 4.5: The deformed pulse due to dispersion is found by analytically propagating a pulse a set distance. This can be corrected by reversing the deformed pulse in time and inputting it into the transmission line. When this pulse is propagated along the transmission line, the dispersion will correct the pulse at the set distance. The DUT can be placed at this location.

at a given location. This is achieved by propagating the desired pulse along the helix and measuring the pulse at the desired location of the device under test. This pulse is then reversed in time and input into the helix. This effectively subtracts the accumulated phase shifts at each frequency due to dispersion and the original signal will be reconstructed at the place of measurement (Fig. 4.5). This method was rejected because the deformed pulses input into the helix are rather complex and analytic and numerical models are required to generate them which may not sufficiently replicate the physical device. In addition, generating these signals with an arbitrary signal generator would require a fast rise time and would have proved challenging.

Another considered method is to slowly decrease the pitch of the helix from a loosely wound helix at the input to the required pitch for the desired velocity. In the region of decreasing ψ, the decreasing pitch can compress the pulse more quickly than dispersion can

distort it. This results in a shorter pulse at the end of the compression section than was input and the pulse at the end will be well formed with minimal deformation (Fig. 4.6). Once the pulse starts to propagate along the constant pitch portion of the system, the effects of dispersion once again deforms the pulse shape. For this geometry the device under test needs be placed directly after the compression section to measure the desired pulse shape at the correct velocity. However, this placement of the device must be done very carefully. If the device is too far to one side and the helix will have the wrong pitch and the fields will be traveling at the wrong velocity. If the device is too far in the other direction, then the fields will be deformed due to dispersion.

4.4.2 Dispersion reduction geometry

A more practical solution to prevent pulse deformation due to dispersion is to add a conductor inside of the helix. Using the separation s=0.5 mm, the dispersion becomes significantly flatter than without the inner conductor with all other geometry the same (see Fig. 4.7). The change total variation in phase velocity is Δv_p=0.039 without the inner conductor and Δv_p=0.001 with the inner conductor for the parameters given in Fig. 4.7. Numerically solving Eq. 4.68 shows the low frequency limit of the phase velocity linearly varies with separation s between the helix and inner conductor as approximately

$$\lim_{f\to 0}(v_p) \propto 0.0025s. \tag{4.70}$$

for s in mm. The high frequency limit remains the same but the phase velocity converges more slowly for smaller s. The slow convergence results in less variation in v_p over a given bandwidth despite the larger variation between the low and high frequency limits. For

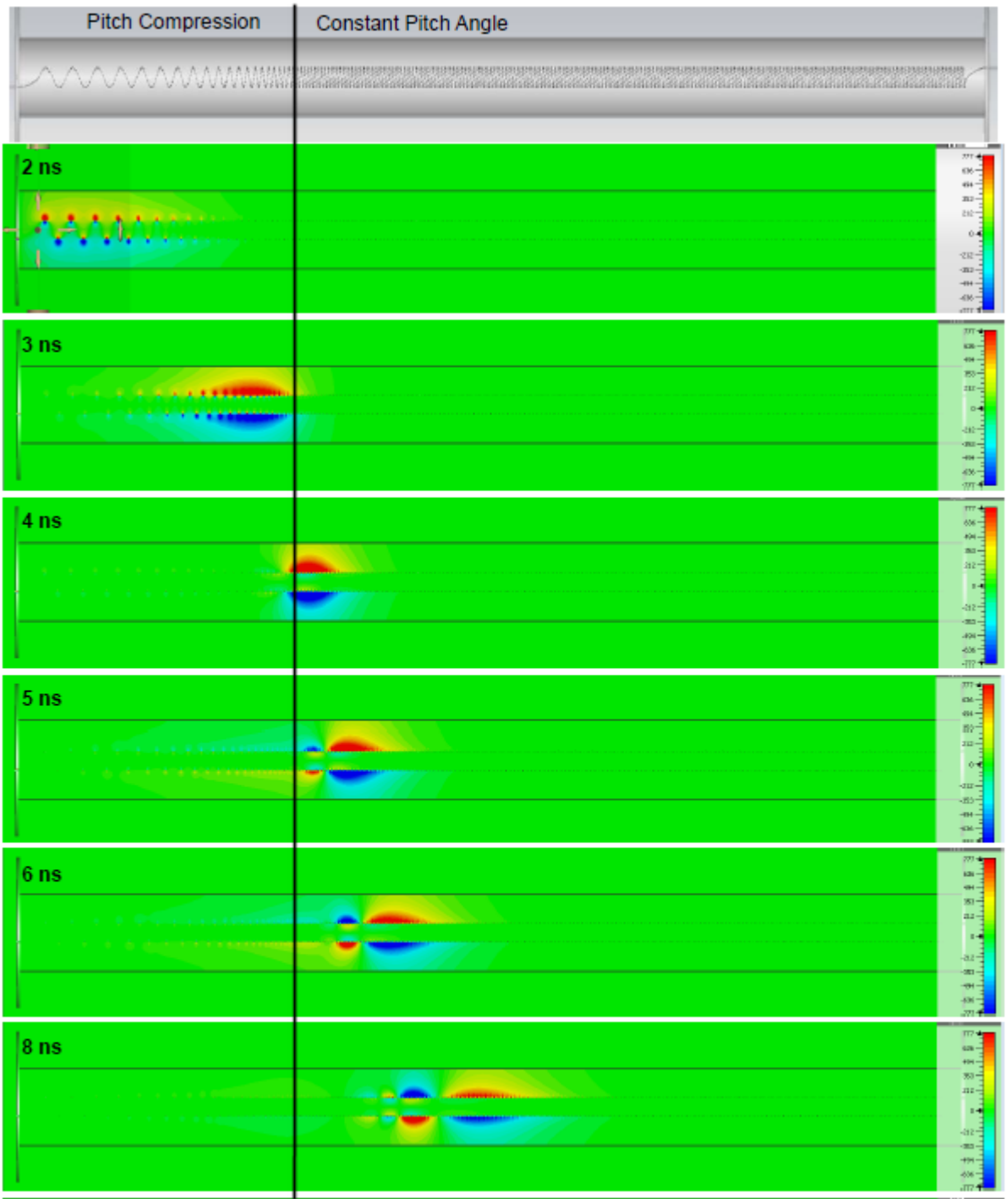

Figure 4.6: Propagation of a Gaussian pulse along a helix with reducing pitch. The horizontal axis is the longitudinal position and the vertical axis the transverse position. The vertical line represents the end of the pitch compression section. The pulse is compressed but maintains its form during the pitch reduction but dispersion deforms the pulse in the constant pitch section.

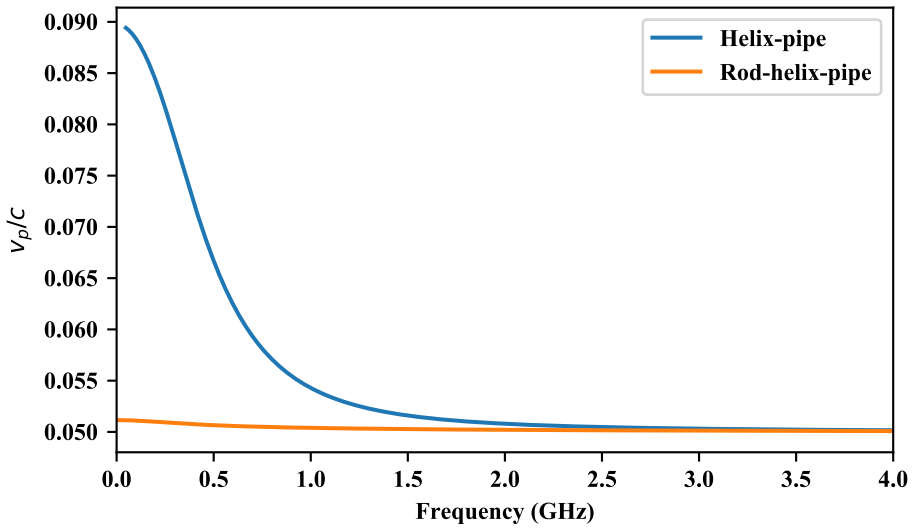

Figure 4.7: Dispersion for different transmission line geometries. The addition of the inner conductor significantly flattens $v_p(\omega)$. Helix parameters s=0.5 mm, a=5 mm, R_e=23.75 mm, ψ=0.05, $\epsilon_i = \epsilon_0$.

example, in Fig. 4.8, for a bandwidth up to 1 GHz, s=1 mm have a range of Δv_p=0.0028 and for s=0.1 mm Δv_p=0.00057. Therefore, a narrow separation should be used when constructing a helical transmission line to limit the deformation of pulses due to dispersion.

The dielectric constant of the dielectric layer can also be varied. In the case of $\epsilon_i = \epsilon_e = \epsilon_0$, the high frequency limit of the phase velocity is $v_p = c \cdot \sin(\psi)$ and the low frequency limit is higher than this. As the internal dielectric constant increases for a fixed geometry the high frequency limit drops approximately as $\epsilon_i^{-1/3}$ while the low frequency limit drops as $\epsilon_i^{-1/2}$ (Fig. 4.8 right). This causes the low frequency limit to drop below the high frequency limit. The difference in scaling causes the disparity between the low and high frequency limits of the phase velocity to increase with ϵ_i which is non-ideal for maintaining pulse shapes. However, its effects can be mitigated by reducing s. In theory, the dielectric constant can be chosen such that the high and low frequency limits of v_p are equal which would be an ideal system, however, in practice this is difficult to realize.

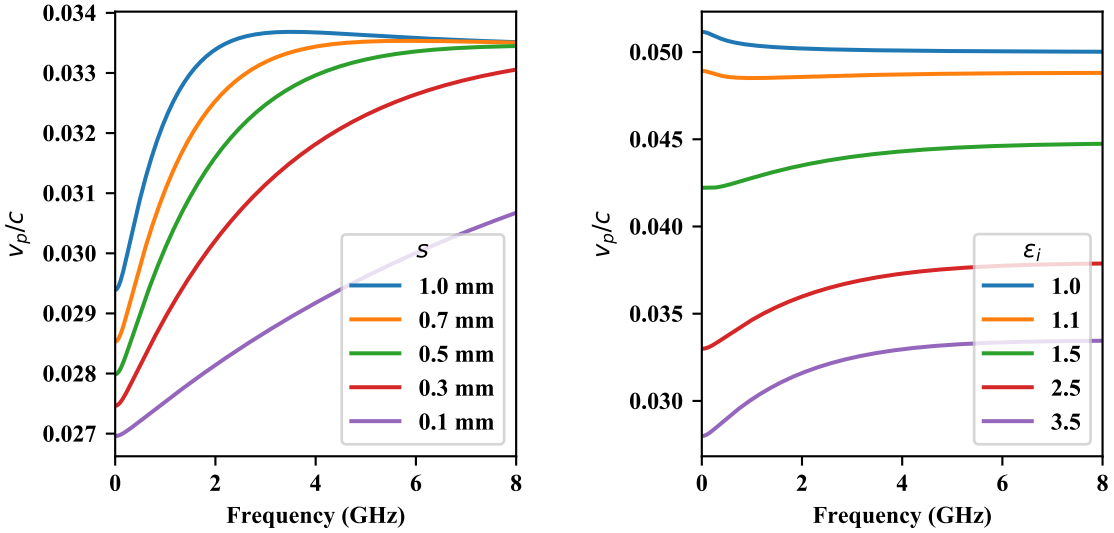

Figure 4.8: Dispersion scaling with s (left) and ϵ_r (right). Helix parameters: s=0.5 mm, a=5 mm, R_e=23.75 mm, ψ=0.05, $\epsilon_i = \epsilon_0$.

When the pitch angle of the helix is changed, the low and high frequency limits of the phase velocity scale as $\sin(\psi)$ (Fig. 4.9). Therefore, the total variation in v_p will increase with the pitch angle. However, with larger pitch angles, the phase velocity converges more slowly. This can result in less deformation to the pulse during propagation.

It should be noted that while significant efforts were made to flatten the dispersion curve to reduce deformations, the electric field near the helix still becomes significantly deformed due to dispersion (see Fig. 4.10). This is caused by the short pulse propagating along helix of ∼200 ps rms needed to replicate the bunch. For pulses this short the bandwidth is large enough to cause significantly different phase shifts resulting in distortion. However, the fields near the helix are not representative of the fields at the pipe wall where they will be measured by the BPM being calibrated. As the radial distance from the helix increases, the high frequency components are suppressed because the field is non-relativistic. Therefore, the fields at the pipe wall will propagate with minimal deformation even though the signal near the helix has significant distortions (Fig. 4.10).

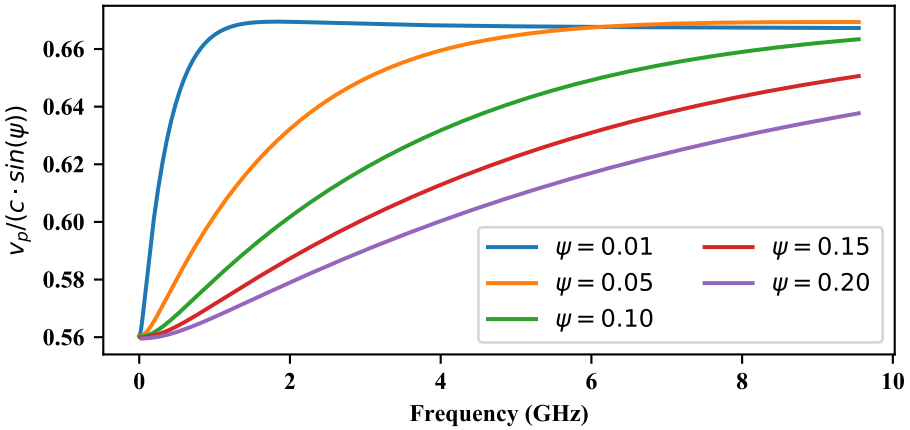

Figure 4.9: The low and high frequency limits of the phase velocity scale with $\sin(\psi)$.

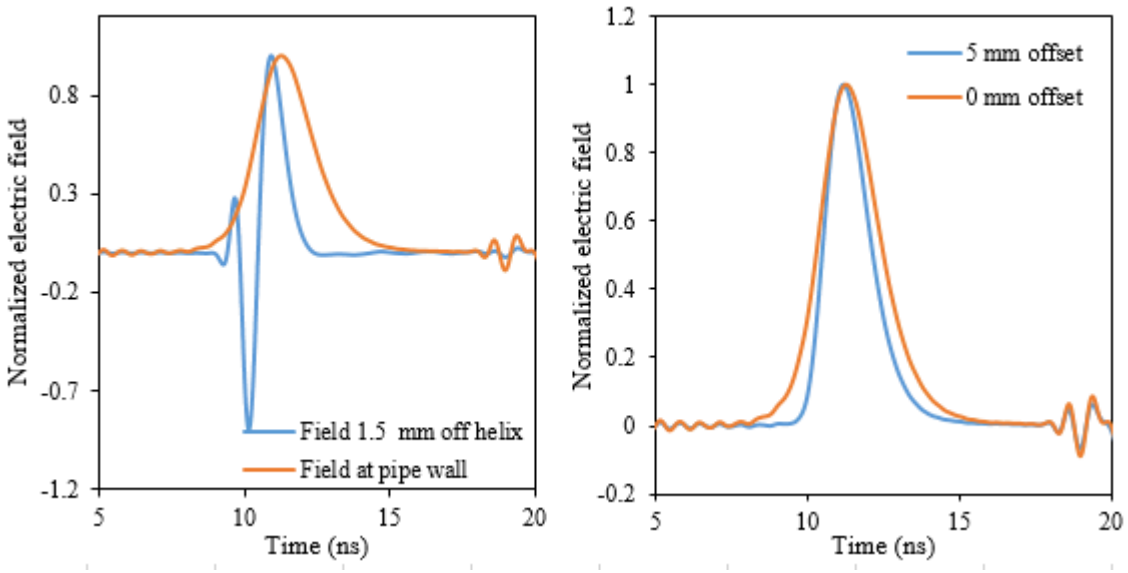

Figure 4.10: Despite efforts to reduce dispersion effects, the pulses near the helix are significantly deformed due to dispersion (left). However, the fields near the pipe wall have the high frequency components suppressed and therefore maintain their shape. This same effect distorts the pulse when the helix is offset in the pipe. Offsets up to 5 mm can be achieved with minimal deformations (right). The pulses shown here are from CST Microwave Studio simulations.

For the test stand, the helix will need to be offset in the pipe. As shown in section 4.5.6, this does not change the dispersion properties, however, it will reduce the radial distance between the helix and the pipe wall resulting in a shorter pulse being measured by at least one of the BPM pickups. Fortunately, for offsets up to 5 mm, the higher frequencies are still sufficiently suppressed in the measured bandwidth and the measured signals are still not significantly deformed.

4.4.3 Higher order effects

The discussions above focuses solely on the $n = 0$ azimuthal mode, however, helical transmission lines support higher order modes [62]. The n^{th} higher order mode is excited at $ka \approx n$. For $a = 5$ mm which will be used for the test stand, this corresponds to $\omega \approx$10 Ghz which is well outside the required bandwidth. Unlike the $n = 0$ mode, which has significantly reduced phase velocity at low frequency compared to the helix in free space, the higher order modes propagate at $v_p(\omega_c) = c$ at the cutoff frequency (Fig. 4.12). The high frequency limits of v_p of the higher order modes are the same as the $n = 0$ mode.

The presented analysis relies solely on the sheath helix model. More complex models can also be made using a tape helix with windings of finite width [63]. These models introduce forbidden regions in $k - h$ space and near the boundaries of these regions, the dispersion diverges from the sheath helix model [62]. However, for the given geometry, the required bandwidth is far from a forbidden region and the sheath helix model is a reasonable approximation (see Fig. 4.11). In addition, the tape helix models predict radiating modes at low frequencies. It is believed that these are seen in simulations, however these travel near the speed of light and can be easily separated from the slow signals (see Fig. 4.21).

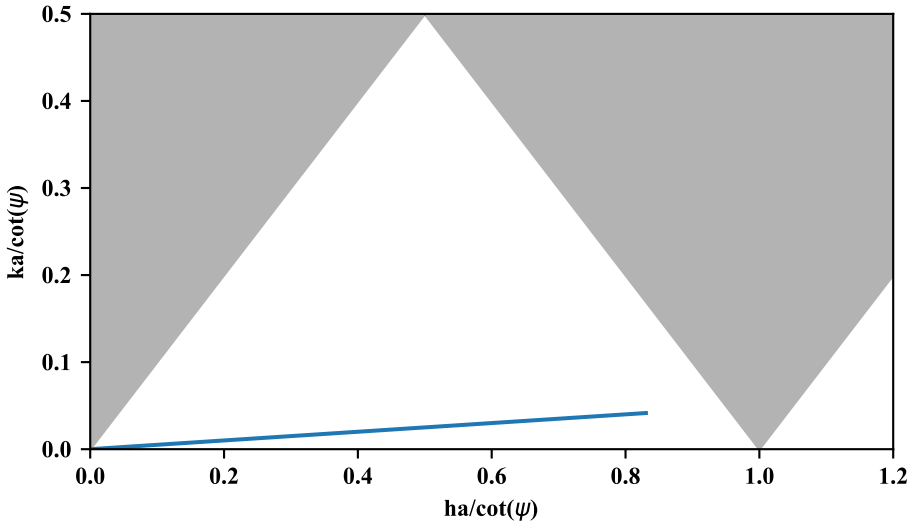

Figure 4.11: The shaded areas are forbidden regions of a tape helix model. For the geometry, ψ=0.05, R_p=20 mm, a=5 mm, s=0.5 mm, up to 8 GHz (blue curve) the helix operates far from the forbidden regions and the sheath helix will be a good approximation.

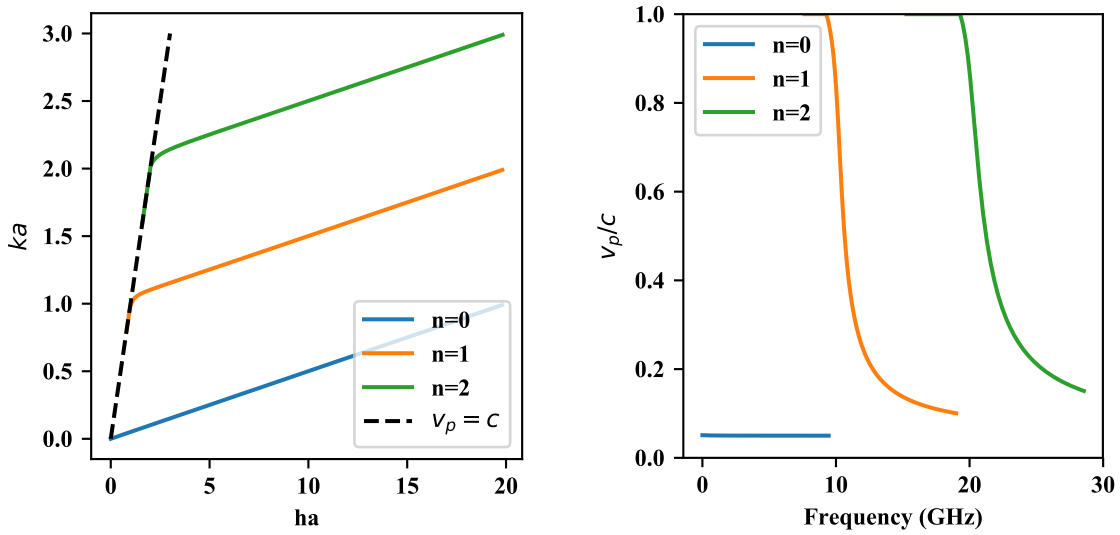

Figure 4.12: Higher order modes have cutoff frequency at $ka \approx n$ and propagate at the speed of light at the cut off frequency. Shown is the first three modes for a helix with geometry ψ=0.05, R_p=20 mm, a=5 mm, s=0.5 mm, $\epsilon_i = \epsilon_0$

4.4.4 Impedance Properties

Once the field coefficients and propagation constants are found, a complete description of the fields is known and the impedance can be calculated. For the three conductor geometry described above, two separate impedances can be defined: Z_i which between the inner conductor and the helix, and Z_e between the helix and pipe. The impedance in each region was calculated by

$$Z_i = \frac{\int_{R_i}^{a} E_{r,i} \mathrm{d}r}{a \int_{-\pi}^{\pi} H_{\theta,i}(a) \mathrm{d}\theta} \tag{4.71}$$

$$Z_e = \frac{\int_{a}^{R_e} E_{r,e} \mathrm{d}r}{R_e \int_{-\pi}^{\pi} H_{\theta,e}(R_e) \mathrm{d}\theta - a \int_{-\pi}^{\pi} H_{\theta,i}(a) \mathrm{d}\theta}. \tag{4.72}$$

In general, these are similar except at low frequencies (Fig. 4.13).

Reducing s maintains the high frequency behavior of the impedance but reduces the low frequency limit and reduces the variation at lower frequencies. This causes the impedance to converge more slowly to the high frequency behavior (Fig. 4.13 left). Ideally, a small enough s should be used to achieve a near constant Z over the desired bandwidth so the input and output of the helical transmission line can easily matched with a resistive network. Increasing the dielectric constant reduces the low frequency limit of the impedance and causes the impedance to start to decrease at a lower frequency (Fig. 4.13 right). While it is preferable to use a lower dielectric constant to increase the bandwidth of near constant impedance region, the effect of the dielectric is not as significant as the effect of s.

The low frequency limit of the impedance scales as $1/sin(\psi)$ while the high frequency limit does not change with the pitch angle (Fig. 4.14. The higher pitch angles converge to the high frequency limit at a higher frequency which can make matching simpler.

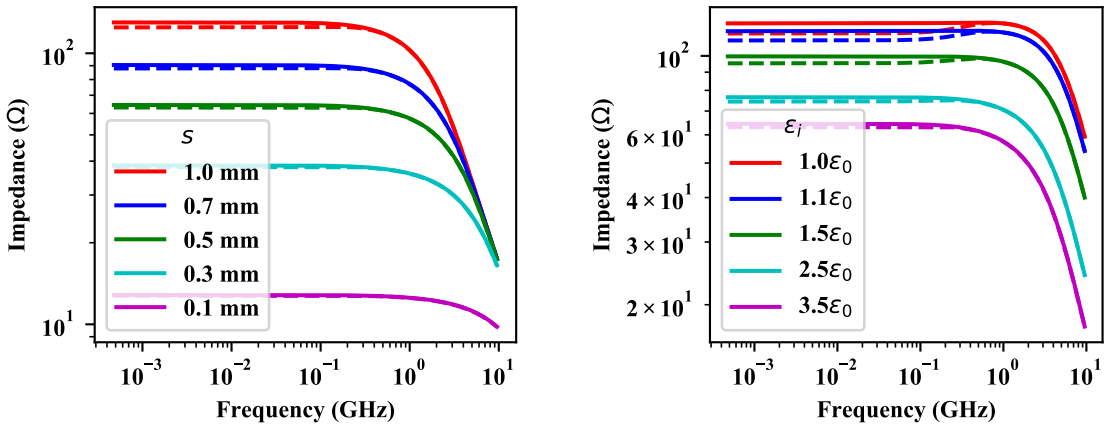

Figure 4.13: Impedance scaling with s and ϵ_i. The solid line is the external impedance and the dashed line is the internal. Helix parameters: s=0.5 mm, a=5 mm, R_e=23.75 mm, ψ=0.05, $\epsilon_i = \epsilon_0$.

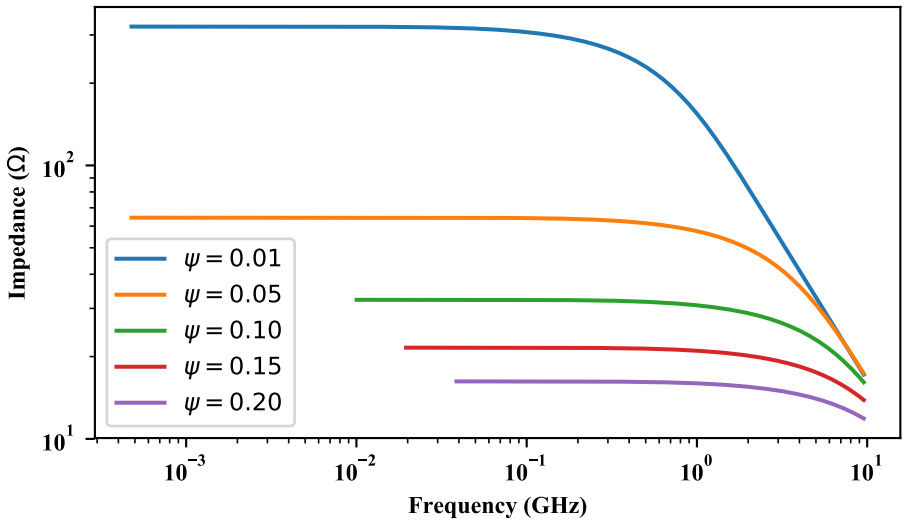

Figure 4.14: The low frequency limit of the impedance scales with $1/\sin(\psi)$

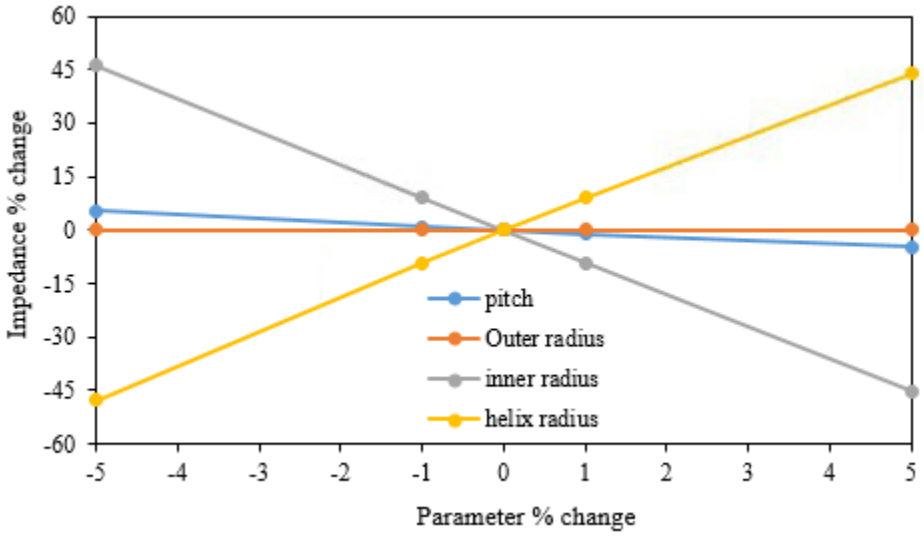

Figure 4.15: Sensitivity of the low frequency limit of the external impedance to variation of different parameters. The impedance is most susceptible to changes in s.

To avoid internal reflections due to changes to the impedance caused by variations in construction, the geometric parameters were varied in the analytic model to determine to which the system is most sensitive. Most of the geometry factors, such as the pitch and outer pipe radius, have a minimal impact on the impedance. The impedance is primarily sensitive to the the inner conductor radius and helix radius, but they have opposite effects the impedance. For example as seen in Fig. 4.15, a 5% increase in the helix radius causes an almost 50% increase in the low frequency limit of the impedance while increasing the inner conductor radius by 5% reduces the impedance by $\sim 50\%$. Therefore, the separation s between the helix and inner conductor must be constant along the transmission line to limit large variations in the impedance for even small changes. The radius of the inner conductor can vary as long as the helix radius also changes to keep the separation constant.

4.4.4.1 Inductance and Capacitance

The inductance L and capacitance C per unit length of the lossless helical transmission line can be determined from the longitudinal propagation constant and impedance based on the general forms derived from the telegraphers equations (Eqs. 4.10, 4.13, 4.14)

$$L_{i,e} = \frac{h}{\omega}\frac{1}{Z_{i,e}} \tag{4.73}$$

$$C_{i,e} = \frac{h}{\omega}Z_{i,e}. \tag{4.74}$$

As with the impedance, these parameters are defined separately for the internal and external regions.

The concept of adding the internal conductor was devised as a method to increase the capacitance of the transmission line to reduce the phase velocity (Eq. 4.13). This is effect can be seen by calculating the internal capacitance for different values of s (Fig. 4.16). Decreasing s does result in a larger capacitance at low frequency and converges to the same limit at high frequency as expected based on dispersion. However, competing with this effect is a decrease in the inductance at low frequency with decreasing s which will increase the phase velocity. The inductance is decreased by almost the same factor as the increase in capacitance with the largest discrepancy seen at frequencies <1 GHz. This similarity results in minimal changes to the phase velocity and large changes to the impedance when changing s. As expected from Fig. 4.13, changing ϵ_i results in significant changes to the high and low frequency limits of the capacitance and inductance.

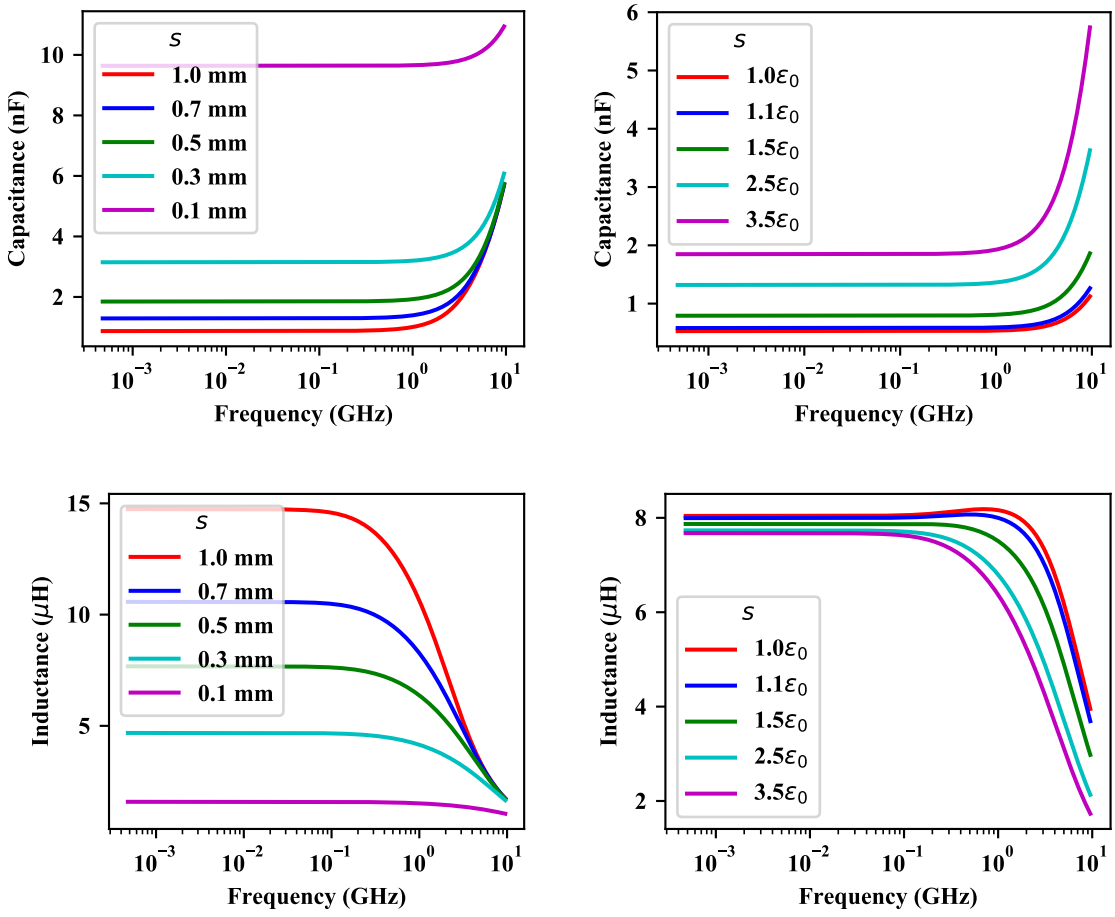

Figure 4.16: Scaling of the internal C and L with s and ϵ_i. The decreasing s reducing the capacitance and increases the inductance by approximately the same factor. Helix parameters: s=0.5 mm, a=5 mm, R_e=23.75 mm, ψ=0.05, $\epsilon_i = \epsilon_0$.

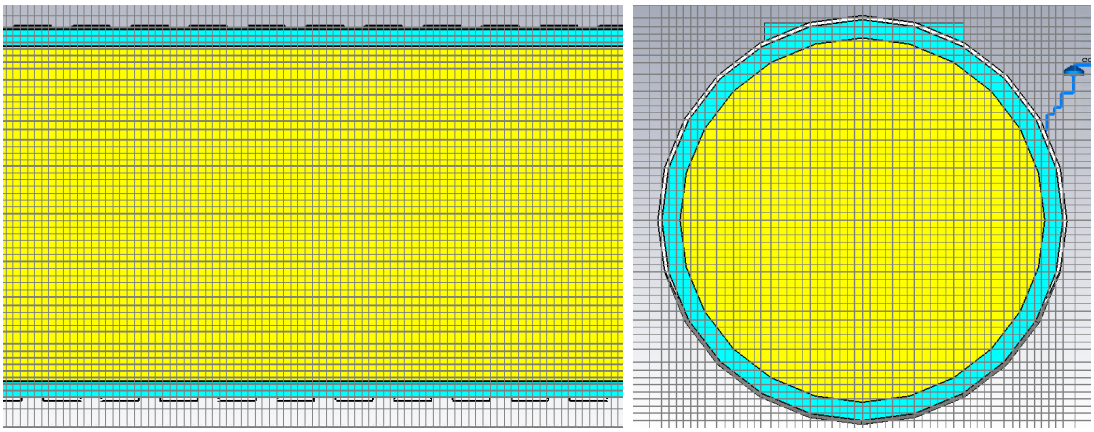

Figure 4.17: Meshing of helical transmission line in CST Microwave Studio for time domain simulations.

Table 4.1: Simulated helical transmission line geometry parameters.

Pipe radius, R_e	20.65 mm
Inner conductor radius, R_i	4.5 mm
Helix radius, a	5 mm
Separation, s	0.5 mm
Pitch angle, ψ	0.05 rad
Dielectric constant, ϵ_i	$3.5\epsilon_0$
Helix wire width	1 mm
Helix wire thickness, Δa	0.1 mm

4.5 Simulations

Time domain simulations of the helical transmission line were performed in CST microwave studio with properties given in Table 4.1 unless otherwise stated. This geometry is expected to be close to what will be used for a BPM test stand. Simulations were performed up to 1.5 GHz which is well below the cutoff frequency of the first higher mode. Note, while it is best to minimize s to improve pulse propagation, $s = 0.5$ mm was used because it was impractical to create a mesh for smaller values. The mesh size was set to resolve the dielectric layer and spacing between windings with at least two mesh cells (Fig. 4.17). The helix has thickness Δa centered around the helix radius a.

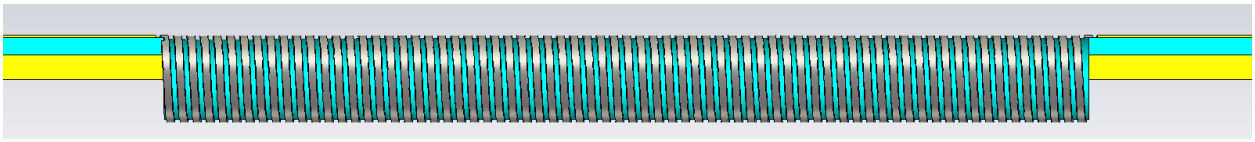

Figure 4.18: Helical transmission line model. Microstrips are used to match the input and output.

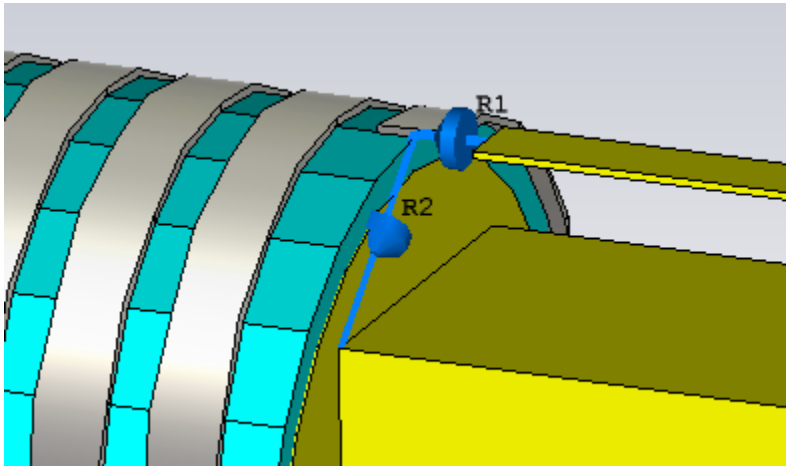

Figure 4.19: Lumped elements used for impedance matching.

4.5.1 Matching

Signals were input onto the helical transmission line using a stripline connected to the helix and inner conductor on either end of the helix (Fig. 4.18). For most simulations, the stripline impedance was set equal to the low frequency limit of the helix impedance and no matching network was used. Alternatively, the stripline impedance can be set unequal to the the helix impedance then matched using a resistive L-network [64] (Fig. 4.19). With the stripline input geometry, the signal is input into the internal region of the transmission line and the stripline (with or without the L-network) only provides an impedance match to this region. The external region must also me matched. This performed with an additional resistor with impedance equal to the low frequency limit of Z_e placed between the outer conductor and helix.

With the stripline matched to the helix, a good match is seen with $S_{1,1}$ <-15 dB and

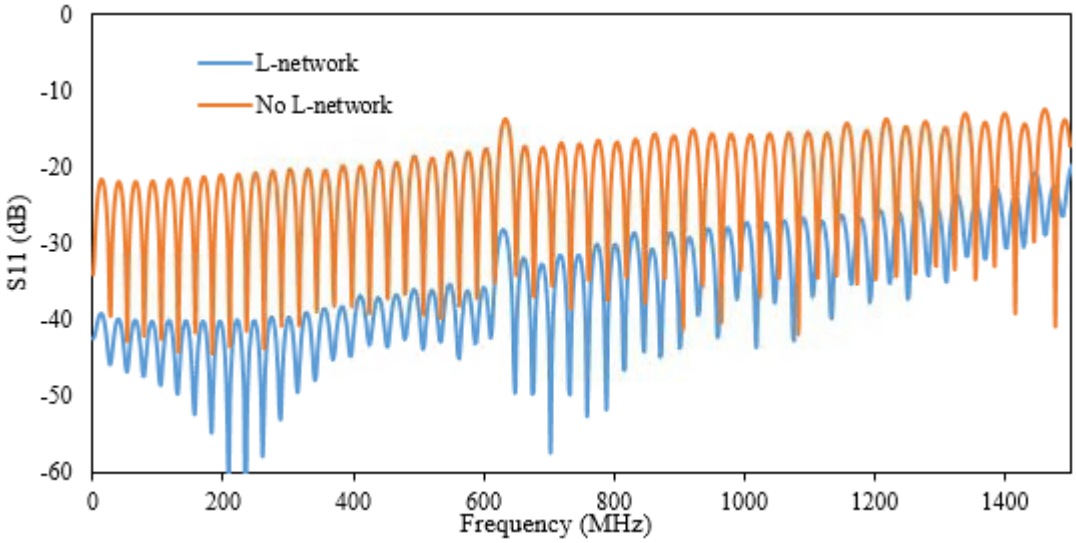

Figure 4.20: $S_{1,1}$ with and without a resistive L-network for matching.

$S_{2,1}$ >-1.5 dB up to 2 GHz. Strong resonances are seen corresponding the harmonics of the helix length for signals traveling at the expected slow phase velocity. These resonances can be damped by using the resistive L-network in the matching scheme (Fig. 4.20). However, the L-network also reduces transmission by ∼11 dB due to losses in the resistors [64]. Therefore, to maximize the amplitude of the propagated signal, the L-network was only used when it was necessary to damp the resonances.

With both matching geometries, a signal traveling at the speed of light proceeds the slow pulse that is a factor of ∼10 lower in amplitude (Fig. 4.21). The speed of light signal is not reflected when it reaches the end of the transmission line, however, it is seen again when the slow signal reaches the end of the helix. This signal may be an excited higher order mode. However, the amplitude of the fast signal is independent of θ therefore it is not an $n > 0$ mode of the sheath helix. It could also be a radiating mode, but the amplitude does not decrease with propagation distance. Another possibility is tape helices, which is used in simulations, are known to support additional modes not present in analytic solutions using the sheath helix approximation. It is possible one of these modes is excited and this

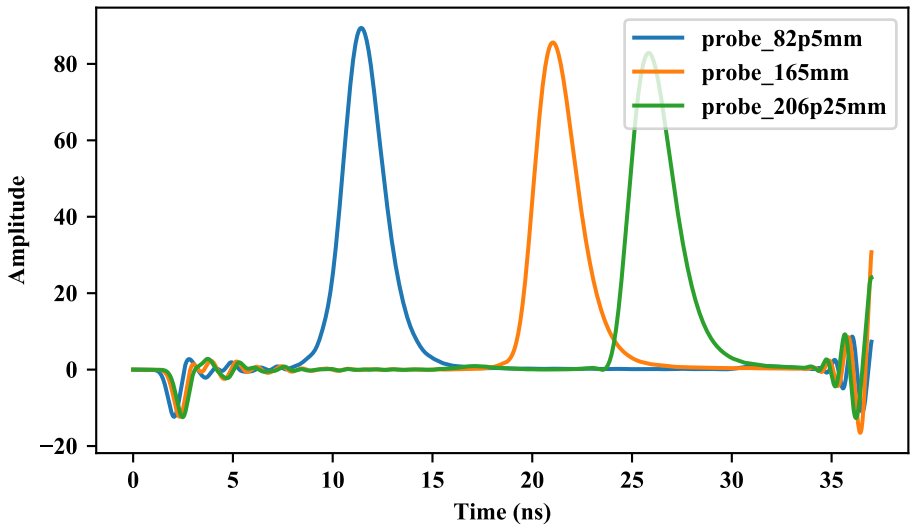

Figure 4.21: The radial electric field at the wall shows minimal deformation during propagation along the transmission line. The slow pulses are proceeded by a smaller speed of light signal that reappears once the slow pulse has reached the end of the transmission line.

geometry should be further studied.

For a single pulse propagating along the helix, which was used for all studies presented in this dissertation, there is enough separation between the fast and slow pulses to easily distinguish them and this abnormality does not affect the results.

4.5.2 Dispersion measurements

The dispersion was measured by inputting a Gaussian pulse into the system and measuring the radial electric field using probes along the transmission line. Nine probes were evenly spaced along the transmission line. The probes were be placed as close as possible to the helix to measure the largest bandwidth. However, if a probe is too close it will measure near field effects from the winding of the helix. To ensure minimal near field effects, eight probes were placed around the helix in $\pi/4$ increments. The probes were moved from 0.25 mm to 2 mm away from the helix to determine the radius where the field is no longer significantly

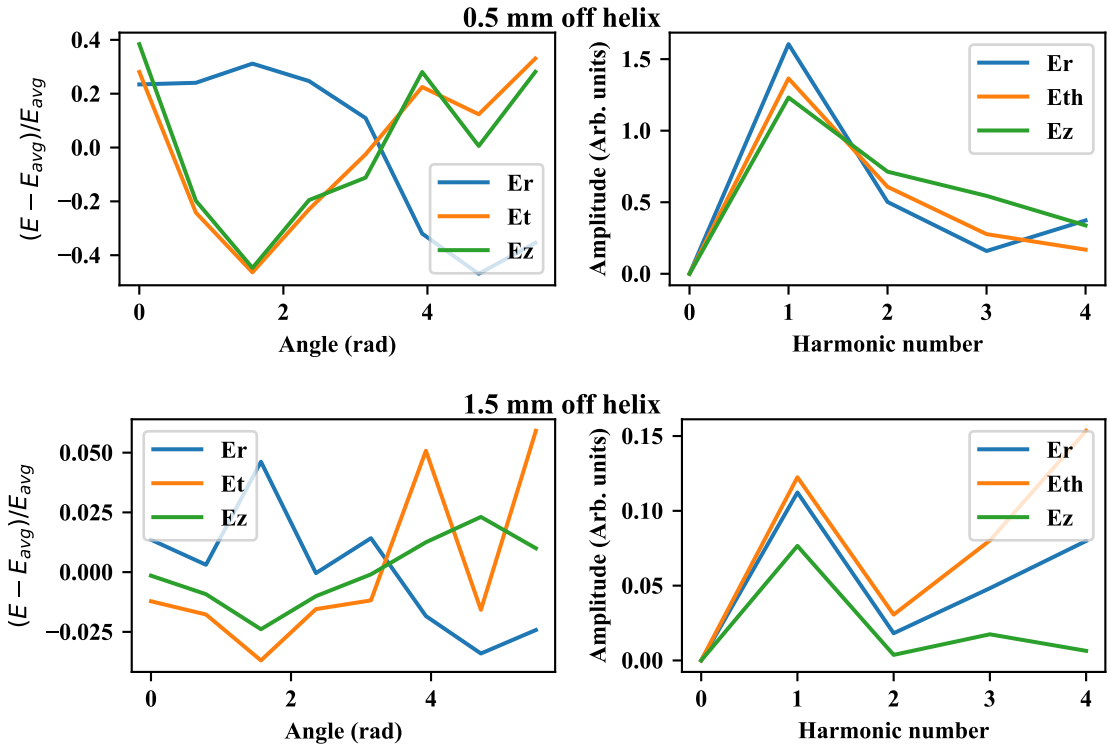

Figure 4.22: The electric field 0.5 mm away from the helix has a strong first harmonic due to the helix windings. At 1.5 mm away from the helix the the angular dependence is significantly reduced.

dependent on θ because within the simulated frequency range, only the $n = 0$ mode should be excited, therefore there should be no azimuthal dependence in the fields.

The fields 0.25 mm from the helix varies chaotically with θ by $\pm 50\%$. At 0.5 mm off the helix, the variations are slightly reduced and show a strong $\cos(\theta)$ dependence due to the helix winding (Fig. 4.22). This behavior is sufficiently reduced for the fields 1.5 mm radially off from the helix with variations on the 1-4% level. While the E_z field still has a clear $\cos(\theta)$ dependence, its amplitude is small enough to ignore.

For measurements of the phase velocity, the probes were placed 1.5 mm away from the helix to maximize the measured bandwidth and avoid near field effects (Fig. 4.23). The time signals from each probe were transformed into the frequency domain to determine the phase

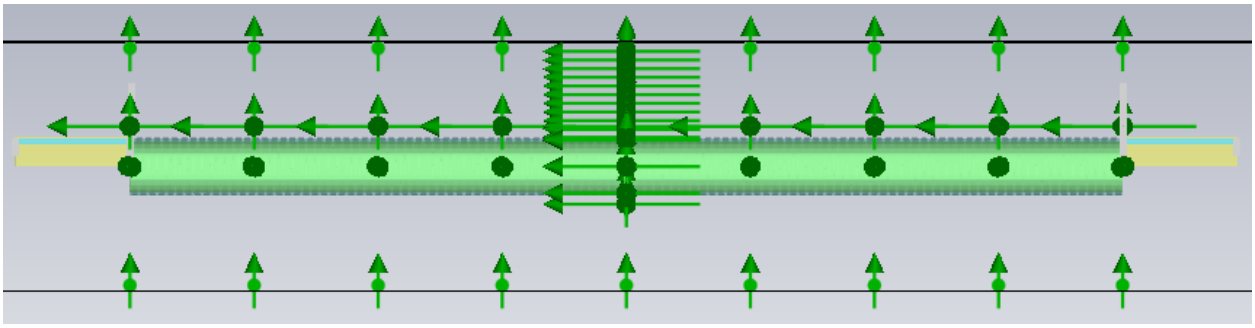

Figure 4.23: Probe suite used to measure the fields from the helix.

shifts as a function of frequency and location. A linear fit of the phases as a function of the probe position gives the phase velocity for each frequency (Fig. 4.24)

$$\phi(f, z) = \frac{f}{v_p} z. \tag{4.75}$$

The measured phase velocity agrees with the sheath helix model within 3% up to 2 GHz at which point, the signals are dominated by noise.

However, near exact agreement can be achieved by assuming $a = a + \Delta a = 0.51$ mm in the analytic model (Fig. 4.25). This value is the sum of the helix radius and the helix thickness in the simulation. This scaling also holds for thicker helices, however, the agreement with theory is poorer most likely because the assumption of an infinitesimally thin helix used in the analytic model no longer holds.

The cause of this phenomenon is unknown and it is particularly strange considering in the simulations the helix conductor is placed at $r \in [a - \Delta a/2, a + \Delta a/2]$. The helix conductor does not reach $a + \Delta a$. In addition, increasing Δa will reduce s which should cause significant changes in the impedance and dispersion, but these effects are not seen. It is speculated that these deviations are caused issues with meshing the thin geometry of the helix.

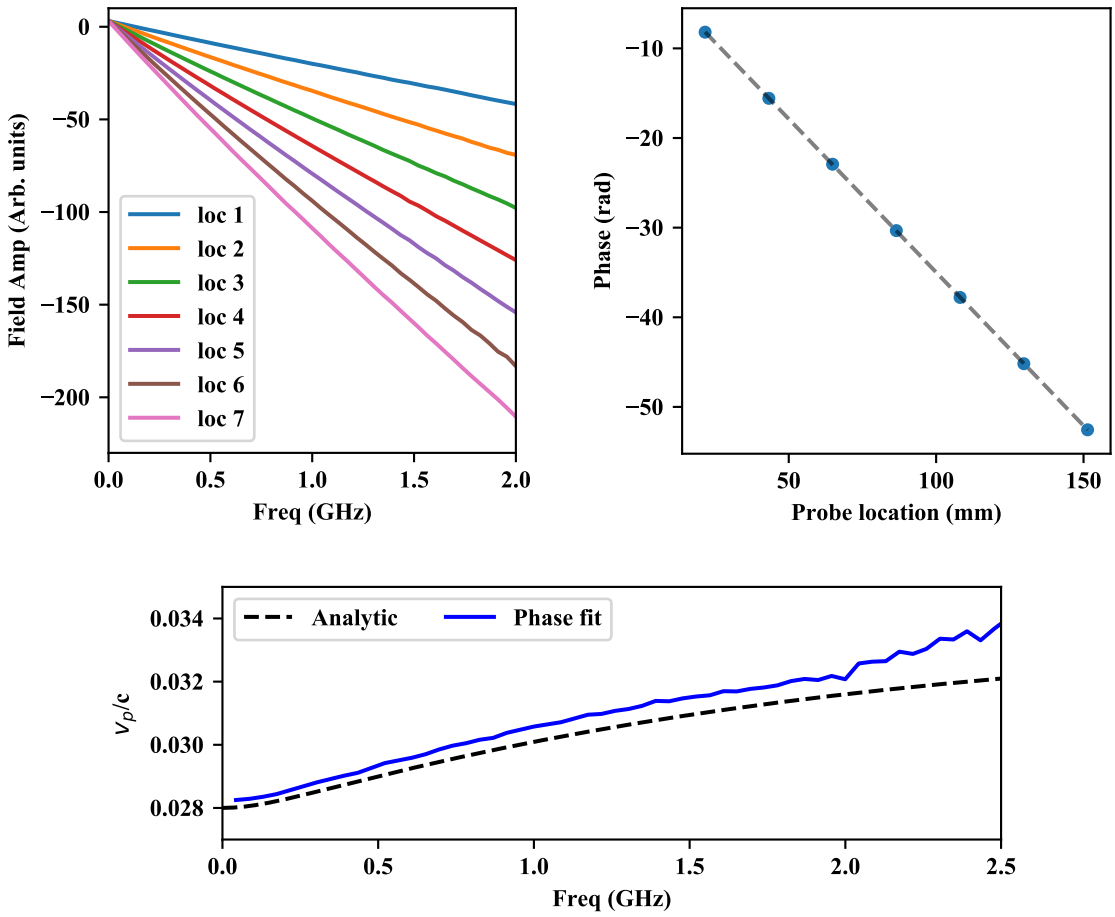

Figure 4.24: The phases at each frequency (top left) for each probe are fitted according to Eq. 4.75 to calculate the phase velocity. The top left plot shows the fitting at 500 MHz. The resulting phase velocity agrees with theory within 3%.

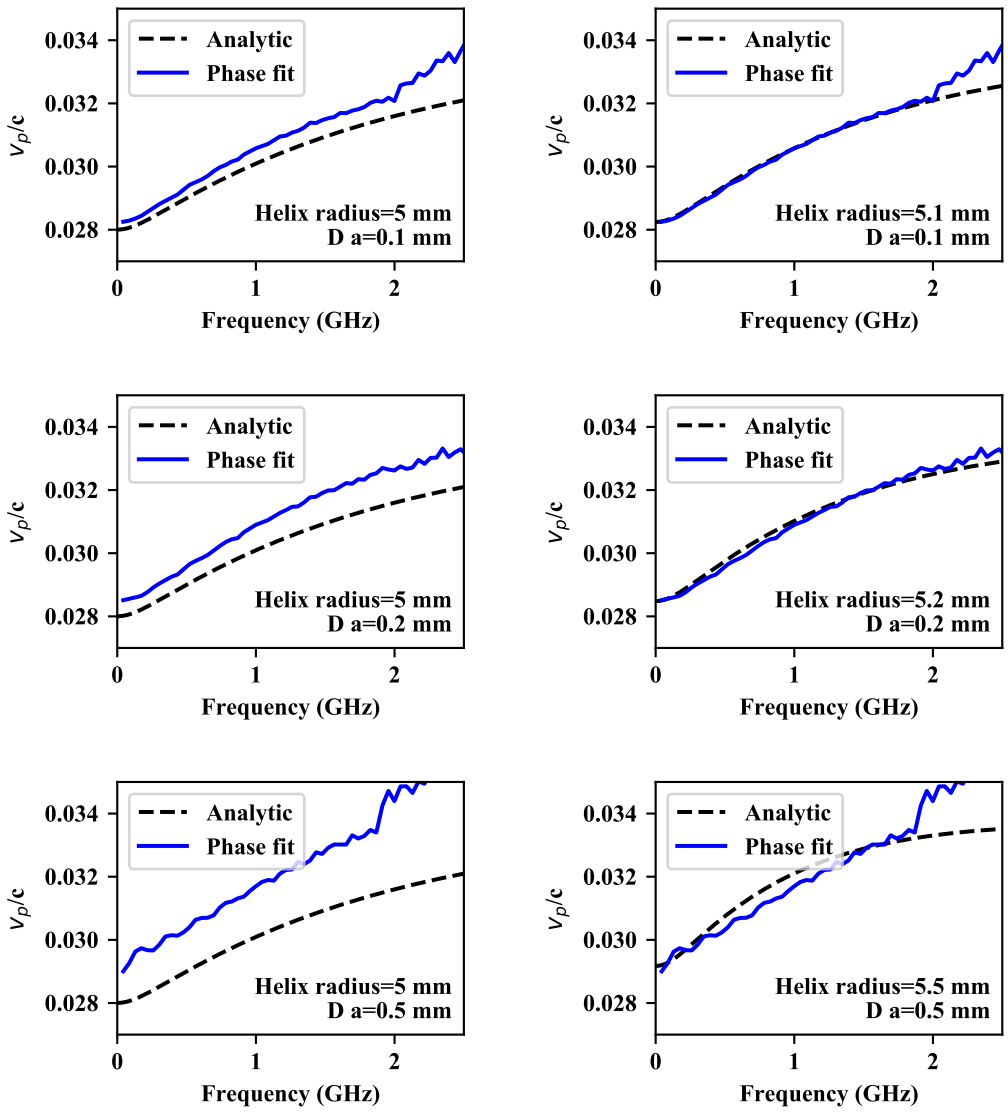

Figure 4.25: Exact matching of the dispersion can be achieved by setting the helix radius in the analytic model to $a + \Delta a$ used in the simulations. The helix radius in simulations is 5 mm for all presented measurements with Δa given by Da on each plot. The stated helix radius is the radius used to analytically calculate the dispersion.

4.5.3 Impedance measurements

The impedance of the helical line was measured using the reflection coefficient $S_{1,1}$. For this measurement, the stripline impedance was changed to 102.5 Ω to be unequal to the helix impedance of $Z_{\text{helix}} \approx 64.5\ \Omega$ and matched to the helix using a resistive L-network to damp the resonances. In addition, to increase $S_{1,1}$ the resistors in the L-network were intentionally set incorrectly for a poor impedance match. With this network, the helix impedance can be found by

$$Z_{\text{helix}} = \left(R_{sh}^{-1} + \left[Z_0 \frac{1 - S_{11}}{1 + S_{11}} + R \right]^{-1} \right)^{-1} \tag{4.76}$$

where Z_0 is the impedance of the microstrip, R is the series resistance, and R_{sh} is the shunt resistance of the L-network.

The real part of the impedance from simulations agrees with the analytic model within 5% up to 2 GHz (see Fig. 4.26). The simulation also showed a small reactance that was <15% of the real impedance which was not present in the analytic model. No attempt was made to match the reactance because the reflections and transmission were adequate with the current matching networks. The added complications of developing a frequency dependent, reactive network to improve the impedance match outweigh the benefits of a slightly better match. However, the source of the imaginary impedance should be explored in the future. In addition, when constructing a helical transmission line for the test stand, it would be best to use $s < 0.5$ mm which will result in less frequency dependence in Z and a better match would be expected.

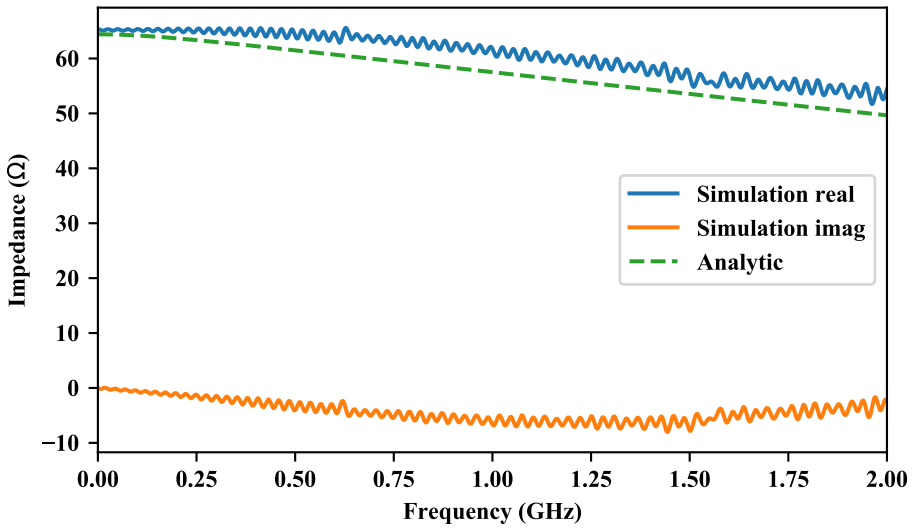

Figure 4.26: The analytic impedance matches the results from simulations with 5%

4.5.4 Electric field scaling

The electric field was compared to the analytic solution by measuring the field using field probes at multiple radii along the transmission line. The fields measured 1.5 mm off the helix were used to determine the field coefficients in the analytic fields. The expected field near the pipe wall can then be calculated using the analytic model and it within 10% with the simulation results up to 0.4 GHz where noise starts to dominate the simulation results (Fig. 4.27).

An unexpected feature of the fields is, when a Gaussian pulse is input, near the helix the amplitude of the radial electric field decreases at low frequency (Fig. 4.28). There are no signs of losses or reflections in the S parameters at low frequency to explain this reduction.

It was found that this phenomena is caused by the coupling between the internal and external regions of the transmission line. This coupling can be derived analytically by taking

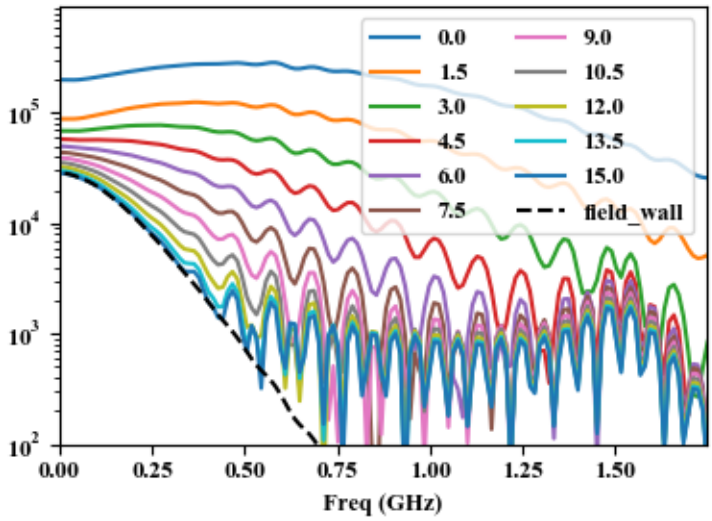

Figure 4.27: The field coefficients were derived from fitting the electric field 1.5 mm from the helix. These are used to calculate the analytic electric field 15 mm from the helix. This field profile agrees well with simulations.

the ratio of the internal and external radial electric fields at the helix

$$\left.\frac{E_{r,e}}{E_{r,i}}\right|_{r=a} = \frac{\gamma_i K_0^2(\gamma_e R_e) w_{1,i} w_{2,e}}{\gamma_e K_0^2(\gamma_i R_i) w_{1,e} w_{2,i}}. \tag{4.77}$$

This can be inverted to determine the appropriate input pulse to have a Gaussian field profile at the helix in the external region which is necessary to replicate a given bunch shape. This coupling agrees with the results of simulations (Fig. 4.28). While an exact input can be generated, for simplicity, for a Gaussian pulse input in the internal region, the spectra near the helix can be roughly fit to the difference of two Gaussians (Fig. 4.28)

$$E_{r,e}\big|_{r=a} \approx G_1 \exp(-2\pi^2\sigma_1^2 f^2) - G_2 \exp(-2\pi^2\sigma_2^2 f^2). \tag{4.78}$$

The standard deviations and amplitudes of the two Gaussian can be determined from the standard deviation σ_i of the input Gaussian pulse. For the parameters given in Table 4.1,

the coefficients can be determined by

$$G_1 = 0.119e^{-0.653\sigma_i} \tag{4.79}$$

$$G_2 = 0.066e^{-0.826\sigma_i} \tag{4.80}$$

$$\sigma_1 = 0.905\sigma_i - 0.005 \tag{4.81}$$

$$\sigma_2 = 1.582\sigma_i + 0.111 \tag{4.82}$$

for σ_i in ns. This fitting can be inverted to determine the required input to achieve a Gaussian pulse of length σ_i in the external region. However, the quality of the double Gaussian fit deteriorates for pulses less than 100 ps rms.

4.5.5 Beam comparison

The electric field propagated by the helical transmission line needs to replicate the fields from a non-relativistic, high gR_p beam. The longitudinal profile can be set by the input pulse with proper consideration of the internal-external coupling. The radial electric field from a line charge (Eq. 1.43) has the same general dependence on coordinates as the field from the helix (Eq. 4.37). However, the beam has g as a transverse propagation constant which corresponds to a fixed beam velocity while the helix has γ_e and the phase velocity varies with frequency.

The variation of the phase velocity of the helix means a choice must be made for the velocity of the modeled beam. It was found for comparing the fields up to 1 GHz, using $v_p(f = 1 \text{ GHz})$ gives the best agreement. The variation in phase velocity makes it only possible to accurately replicate the fields from a beam within a specific bandwidth. To increase the bandwidth the dispersion curve must be flatted which is an addition reason to

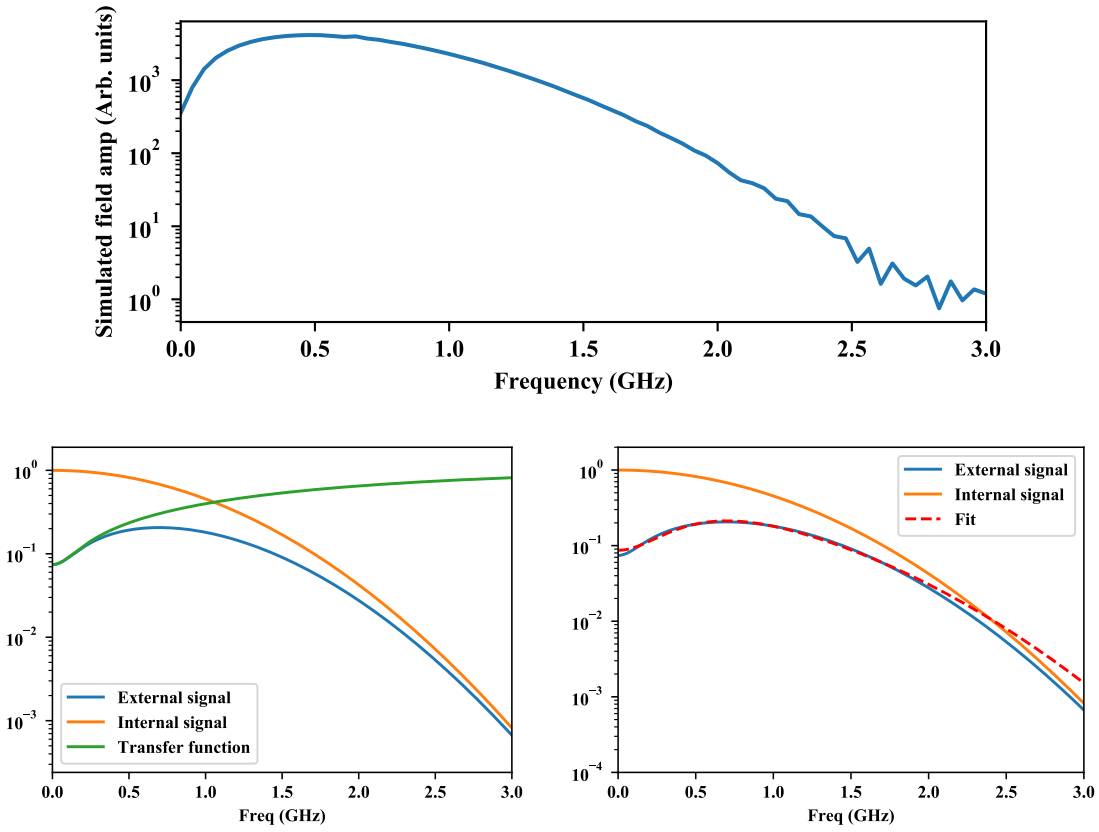

Figure 4.28: The field in the external region is suppressed at low frequency compared to the field in the internal region. This matches with signals measured 1.5 mm off the helix in simulations. For a Gaussian input, the field in the external region can be roughly fit to the difference of two Gaussians.

reduce s. The smaller s there will be less variations in the phase velocity, which will result in better agreement over a larger bandwidth.

This disparity in propagation constants also causes the fields to scale differently with r. Therefore the fields of a beam and a helix cannot be the same over the entire pipe aperture. In order to replicate the BPM signals from a beam, the field profile from the helix at the pipe wall must match the expected fields from a beam. This exact profile on the pipe will be dependent of the choice of the transverse distribution of the modeled beam. To determine the best transverse profile, the radial electric field of the beam was fit to the field of the helix for a pencil beam, ring beam, and uniform beam using the beam radius as a fit parameter (Fig. 4.29). The ring distribution best fit the helix fields with deviation of at most 10% up to 1 GHz. Up to 0.5 GHz, the bandwidth of the FRIB BPMs, the ring distribution varies from the helix field by less than 1%. The fields from a uniform beam match well up to ∼0.3 GHz which is sufficient for calibrating position measurements taken at 161 MHz. The helix fields cannot model a pencil beam. This is primarily because there is no geometric parameter of a pencil, such as radius, that can be varied to fit the fields.

4.5.6 Offset helices

The analytic and simulation work presented in this chapter has all been concerned with centered helices. However, for the test stand to calibrate BPMs, the helix must be moved off center to replicate offset beams. The performance and applicability of the helical transmission line as a test stand would be limited if the dispersion and impedance properties of the helical transmission line vary significantly when the helix is offset in a pipe. To explore the effects of offsetting the helix in simulations, a helix was moved off center in a pipe in 2 mm steps up to 10 mm. At each step the the dispersion was calculated from probes measuring

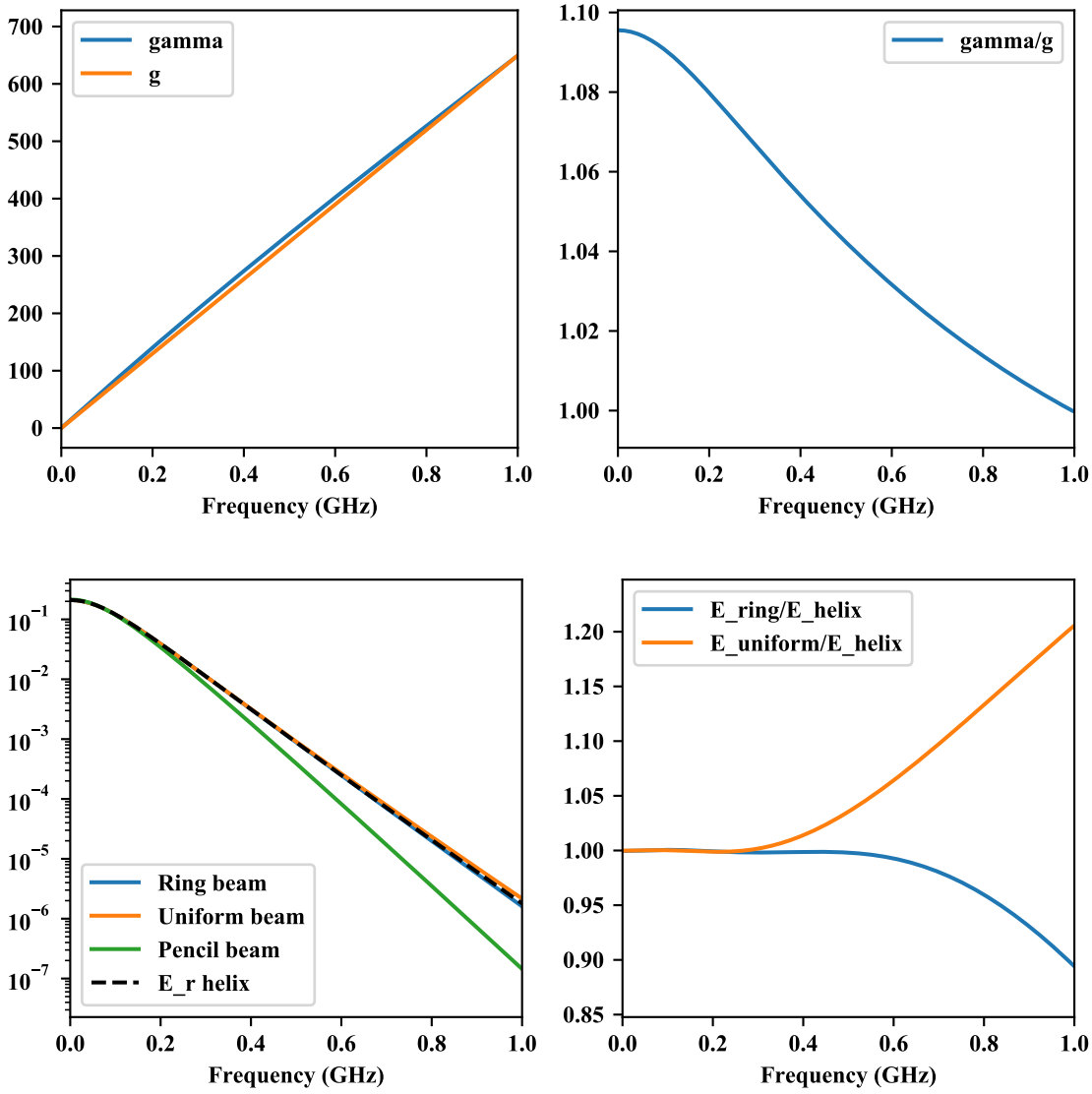

Figure 4.29: The fields from the helix best match a ring beam. R_i=4.5 mm, a=5 mm, R_e=20.65 mm, ψ=0.05, $\epsilon_i = 3.5\epsilon_0$

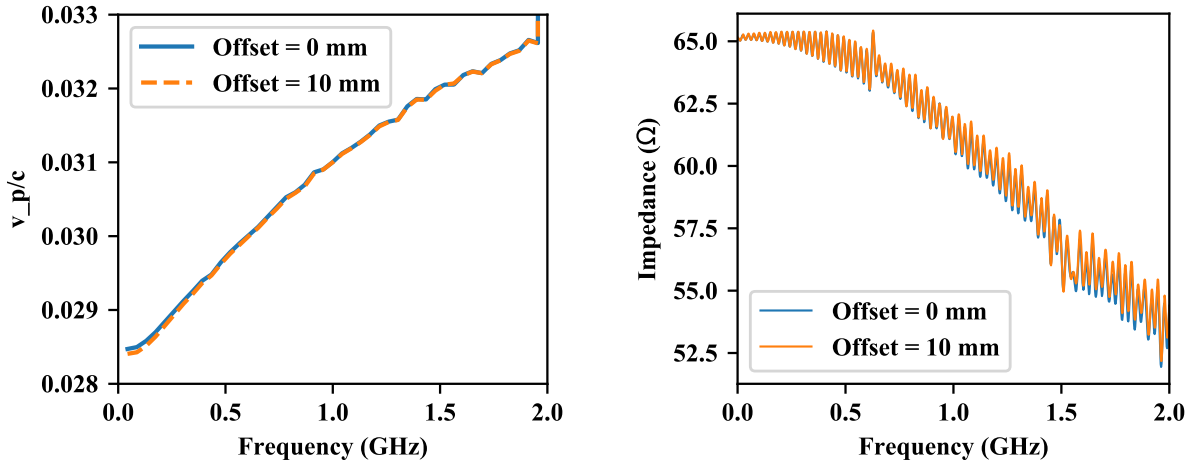

Figure 4.30: The dispersion and impedance sees no significant variation due to offsets up to 10 mm offsets.

the electric field 1.5 mm off the helix as described in section 4.5.2. No significant change in the dispersion was seen with offsetting the helix up to 2 GHz (Fig. 4.30). In addition, the impedance was determined using the reflection coefficient from a mismatched L-network for each helix location. Once, again, no significant change in the impedance was seen when the helix was offset (Fig. 4.30). These are highly beneficial behaviors because no additional considerations need to be taken when the helix is offset to replicate off center beams. The helix can be significantly offset in the pipe and the input pulse will not need to be changed because there is no change to dispersion and the matching network will not need to varied because the impedance is also stable.

4.6 Future work

while the analytic and numeric models show a helical transmission line is capable of replicating the field profiles and velocity of a non-relativistic beam, there are discrepancies between the two models. Most notable is the fast pulses seen in simulations and the imaginary part

of the impedance do not appear in the analytic solution. These may be caused by the sheath helix approximation used analytically not fully describing the fields generated by the tape helix used in simulations. Analytic models of tape helices exist and predict additional modes that could explain the discrepancies. While the sheath helix approximation is sufficient to show helical transmission lines can be used for this test stand, it would be beneficial to develop an analytic model using a tape helix geometry to determine if the higher order affects will cause issues.

In addition, further tests of the numerical model should be performed. In particular, further studies of the discrepancy between the dispersion measured in the simulations and the analytic model. In particular, the scaling with Δa should be further explored to determined if this is a real affect or caused by issues with the meshing of the thin geometry of the helix and dielectric layer.

The next step for this project is to construct and test a helical transmission line to verify the results presented in this chapter. A straight forward method for constructing the helix is to insert a conducting rod into a dielectric tube then creating a grove to lay the helix with a thread cutter. From discussions with the staff at the MSU physics machine shop, it is expected this method can at best achieve $s \sim 0.5$ mm. This value of s was used in most simulations and it is sufficient to propagate pulses with minimal dispersion effects. However, a smaller s would be preferable for impedance matching and less variations in the phase velocity. This would require a different construction method to be developed.

The initial construction should be focused on measuring the properties of the transmission line and not be used as a BPM test stand. For this the outer pipe should be outfitted with multiple pickups at different positions in z to measure the dispersion. These pickups should be as small as is practical to limit the effects of their geometry on the measured signals which

will allow easier comparison to the expected field structure from the analytic and numeric models.

Chapter 5

Conclusions

It is important to characterize and monitor the beam quality in hadron accelerators. It is particularly important to do so in the front ends where the beam is non-relativistic and evolving rapidly. The large diagnostic suites in the front ends are used ensure a quality beam enters the main accelerating structure to reduces losses and maximize the performance of the accelerator. The operation of the accelerator can be improved by gaining more information about the beam quality by adding more measurements of the beam properties and taking more detailed measurements of the beam distribution. This can be achieved by furthering the analysis of signals produced by existing diagnostic devices.

One particular feature of the beam that needs characterized is the beam tails as these portions of the beam are far from the beam center are the most likely to be lost in the accelerator. To quantify the phase space distributions and beam tails measured in $x - x'$ phase space, the phase portraits can be converted to $J - \phi$ coordinates. In this coordinate system the distribution is stable under linear optics and can be quantified and directly compared to other measurements to study tail growth caused by non-linear forces.

The presented method for characterizing the beam core and tails relies on fitting to a model of the core distribution. For the measurements presented in this disseration, taken in the PIP2IT MEBT, the core was Gaussian. However, the same methodology can be used for any distribution and applied to other accelerators as long there is an adequate model of the beam core for fitting. With this analysis technique, the beam tails are clearly visible

when plotting in $J - \phi$ coordinates which could be a useful tool in the control room to help visualize, quantify, and reduce the tails.

For monitoring the beam properties, BPMs are one of the most important and prevalent devices. By adding measurements of multiple harmonics of the bunch repetition rate, these position monitors can in theory also monitor the bunch size which would be highly beneficial for monitoring the beam quality. Unfortunately, it was shown in the front ends, where beam is non-relativistic, determining the bunch size from these measurements is challenging and requires a adequate model of transverse profile of the beam. While the measurements in the FRIB MEBT failed to replicate the expected trends, the resulting measurements were close to the expected values. This gives some hope that for beams with simpler transverse profiles, this method can be successful for non-relativistic beam.

It was also show analytically that these multi-harmonics measurements can be made easier by measuring relativistic beam because the effects of the transverse distribution damps out and only the longitudinal profile needs to be fit. While, this is less information about the bunch, by using every BPM in a relativistic section to measure the bunch length, the longitudinal dynamics can be continuously monitored along the beam line even while delivering the beam to the users. This extensive monitoring is currently not possible with the existing devices and techniques.

Key to the multi-harmonic BPM measurements and position measurements for non-relativistic beams is understanding the signals generated by the BPM pickups and how they relate to the beam. Current studies of these signals rely on analytic and numeric models. To study and calibrate the signals from the physical devices that will be used in the beamline, a test stand was developed using a helical transmission line. This will allow further development of the multi-harmonic analysis by propagating pulses with known properties to

verify the behavior of the BPM signals.

Analytic and numeric models of this test stand show it is capable of replicating the velocity and electric field profiles on the BPM pickups of a non-relativistic beam. With these properties understood, all that remains construct, test, and use these helical structures as a test stand for BPMs.

All of the devices and techniques presented in this dissertation promise to improve our ability to monitor and characterize the beam quality. They warrant further investigation and have the possibility to greatly benefit the beam diagnostic's toolbox. The broadband BPM measurements have the most obvious advantage of turning every BPM into a non-interceptive longitudinal profile monitor. The helical test stand should accompany these BPM measurements for measurements at low energies. And the action-phase analysis can give a more detailed view of the beam distribution with less concern of variations between separate measurements.

BIBLIOGRAPHY

BIBLIOGRAPHY

[1] Jie Wei. The Very High Intensity Future. In *International Particle Accelerator Conference (IPAC 2014)*, page MOYBA01, June 15-20 2014.

[2] D. Leitner, M. L. Galloway, T. J. Loew, C. M. Lyneis, I. Castro Rodriguez, and D. S. Todd. High intensity production of high and medium charge state uranium and other heavy ion beams with venus. *Review of Scientific Instruments*, 79(2):02C710, 2008.

[3] Thomas P. Wangler. *RF Linear Accelerators*. Wiley, 2nd ed. edition, 2008.

[4] J. Struckmeier and M. Reiser. Theoretical studies of envelope oscillations and instabilities of mismatched intense charged-particle beams in periodic focusing channels. *Part. Accel.*, 14:227–260, 1984.

[5] Robert E. Shafer. Beam position monitoring. *AIP Conference Proceedings*, 212(1):26–58, 1990.

[6] Oren Yair, Jenna Crisp, Gerlind Kiupel, Steve Lidia, and Robert Webber. Frib beam position monitor pick-up design. In *Proceedings, International Beam Instrumentation Conference, IBIC2014*, 09 2014.

[7] P Forck, P Kowina, and D Liakin. Beam position monitors. In *CERN Accelerator School: Course on Beam Diagnostics*, 05 2008.

[8] David M. Pozar. *Microwave Engineering*. Wiley, 4th ed. edition, 2012.

[9] R. Scrivens. Proton and ion sources for high intensity accelerators. In *9th European Particle Accelerator Conference (EPAC 2004)*, July 2004.

[10] Ian Brown. *The Physics and Technology of Ion Sources*. Wiley, 2004.

[11] Helmut Wiedemann. *Particle Accelerator Physics*. Springer, 2015.

[12] P. F. Derwent, J.-P. Carneiro, J. Edelen, V. Lebedev, L. Prost, A. Saini, A. Shemyakin, and J. Steimel. PIP-II injector test: challenges and status. In *Proc. of LINAC'16*, September 2016. WE1A01.

[13] PIP-II conceptual design report, 2018.

[14] Jie Wei et al. The FRIB Superconducting Linac - Status and Plans. In *28th International Linear Accelerator Conference*, page MO1A01, 2017.

[15] John David Jackson. *Classical electrodynamics*. Wiley, New York, NY, 3rd ed. edition, 1999.

[16] John Irwin. The Application of Lie algebra techniques to beam transport design. *Nucl. Instrum. Meth. A*, 298:460–472, 1990.

[17] Alexander Wu Chao, Karl Hubert Mess, Maury Tigner, and Frank Zimmerman. *Handbook of Accelerator Physics and Engineering*. World Scientific, 2nd ed. edition, 2013.

[18] M. Reiser. *Theory and Design of Charged Particle Beams*, volume 2. Wiley-VCH, Weinheim, Germany, 1994.

[19] F.J. Sacherer. Rms envelope equations with space charge. *IEEE Trans. Nucl. Sci.*, 18:1105–1107, 1971.

[20] J. Cuperus. Monitoring of Particle Beams at High Frequencies. *Nucl. Instrum. Meth.*, 145:219, 1977.

[21] M. Abramowitz and I. A. Stegun. *Handbook of Mathematical Functions with Formulas, Graphs, and Mathematical Tables*. National Bureau of Standards, 1972.

[22] Wolfram Research, Inc. Mathematica, Version 12.1. Champaign, IL, 2020.

[23] P. Kowina, W. Forck, P. Kaufmann, and P. Moritz. Beam position monitor sensitivity for low-β beams. In *9th European Workshop on Beam Diagnostics and Instrumentation for Particle Accelerators (DIPAC 09)*, May 25-27 2009.

[24] Robert E. Shafer. Beam position monitor sensitivity for low-β beams. *AIP Conference Proceedings*, 319(1):303–308, 1994.

[25] Chris Wilcox, J.C. Medland, S. Payne, Alex Pertica, and M. Probert. Optimisation of a split plate position monitor for the isis proton synchrotron. In *International Beam Instrumentation Conference, IBIC2013*, 09 2013. WEPC25.

[26] Seadat Varnasseri, Rafael Baron, Ibon Bustinduy, Hooman Hassanzadegan, Andreas Jansson, Arturo Ortega, Igor Rueda, Thomas Shea, and Aitor Zugazaga. Design of

Stripline Beam Position Monitors for the ESS MEBT. In *5th International Beam Instrumentation Conference, IBIC12*, page WEPG05, 2017.

[27] M. Hoffmann. Measurements, statistics, and errors. In *CERN Accelerator School: Course on Beam Diagnostics*, 05 2008.

[28] A. Alexopoulos, C. Barschel, E. Bravin, G. Bregliozzi, N. Chritin, B. Dehning, M. Ferro-Luzzi, M. Giovannozzi, R. Jacobsson, L. Jensen, R. Jones, V. Kain, R. Kieffer, R. Matev, M. Rihl, V. Salustino Guimaraes, R. Veness, S. Vlachos, B. Würkner, A. Bay, F. Blanc, S. Giani, O. Girard, G. Haefeli, P. Hopchev, A. Kuonen, T. Nakada, O. Schneider, M. Tobin, Z. Xu, R. Greim, T. Kirn, S. Schael, and M. Wlochal. Noninvasive lhc transverse beam size measurement using inelastic beam-gas interactions. *Phys. Rev. Accel. Beams*, 22:042801, Apr 2019.

[29] P. Strehl. *Beam Instrumentaiton and Diagnostics*. Springer, 2006.

[30] Herman Kremers, JPM Beijers, Vladimir Mironov, J Mulder, Suresh Saminathan, and Sytze Brandenburg. Trace space reconstruction from pepperpot data. *Proceedings of ECRIS2010, Grenoble, France*, 01 2010. TUCOAK02.

[31] M. W. Wang, Q. Z. Xing, S. X. Zheng, X. L. Guan, W. H. Huang, X. W. Wang, Z. M. Wang, D. Wang, C. Y. Wei, and M. T. Qiu. Design and test results of a double-slit emittance meter at xipaf. *7th International Beam Instrumentation Conference, IBIC18*, 2018. WEPC09.

[32] A. Zhukov and A. Aleksandrov. High resolution emittance measurements at sns front end. *Linear Accelerator Conference, LICAC12*, 2012. THPB012.

[33] P. W. Allison, J. D. Sherman, and D. B. Holtkamp. An emittance scanner for intense low-energy ion beams. *IEEE Transactions on Nuclear Science*, 30(4):2204–2206, 1983.

[34] B. X. Han, M. P. Stockli, R. F. Welton, T. R. Pennisi, S. N. Murray, M. Santana, and C. D. Long. Emittance studies of the spallation neutron source external-antenna h- ion source. *Review of Scientific Instruments*, 81(2):02B721, 2010.

[35] Martin Stockli, R. Welton, and R. Keller. Self-consistent, unbiased root-mean-square emittance analysis. *Review of Scientific Instruments*, 75:1646–1649, 05 2004.

[36] A. Zhukov and A. Aleksandrov. High resolution emittance measurements at sns front end. In *Proc. of LINAC'12*, 2012. THPB012.

[37] Alan S. Fisher. Summary of the 2014 Beam-Halo Monitoring Workshop. In *Proceedings, 4th International Beam Instrumentation Conference, IBIC2015*, 2016. THBLA01.

[38] Z. Zhang, A. Aleksandrov, and S. Cousineau. Fodo lattice design for beam halo research at sns. In *Proceedings, International Particle Accelerator Conference, IPAC2017*, 2017. TUPVA148.

[39] A. Shemyakin, J.-P. Carneiro, B. Hanna, V. Lebedev, L. Prost, V. Scarpine A. Saini, V.L.S. Sista, and C. Richard. Experimental study of beam dynamics in the PIP-II MEBT prototype. In *Proc. of HB'18*, June 2018. MOP1WB03.

[40] A. Saini, B. Hanna, J. Huber, L. Prost, V. Scarpine, J. Steimel, S.V.L.S. Rao, and C. Richard. Beam tests of the pip-ii injector test radio frequency quadrupole. *Nuclear Instruments and Methods in Physics Research Section A: Accelerators, Spectrometers, Detectors and Associated Equipment*, 978:164368, 2020.

[41] V. L. A. Sista and A. Shemyakin. Beam jitter in the pip2it mebt, 2017. PIP-II Document 1106.

[42] C. Richard, M. Alvarez, J. P. Carneiro, B. Hanna, L. Prost, A. Saini, V. Scarpine, and A. Shemyakin. Measurements of a 2.1 mev h- beam with an allison scanner. *Review of Scientific Instruments*, 91(7):073301, 2020.

[43] L. Prost, J.-P. Carneiro, and A. Shemyakin. Low emittance growth in a low energy beam transport line with un-neutralized section. *Phys. Rev. Accel. Beams*, 21:020101, Feb 2018.

[44] O.A. Anderson and L. Soroka. Emittance growth in intense mismatched beams. 870316:1043, 1987.

[45] Richard D'Arcy and Alexander Shemyakin. Calculation of the effect of slit size on emittance measurements made by a two-slit scanner, 2016.

[46] Jonathan C. Wong, Steven M. Lund, and Tomofumi Maruta. High resolution phase space measurements with allison-type emittance scanners. *Phys. Rev. Accel. Beams*, 22:072801, Jul 2019.

[47] A. Saini and A. Shemyakin. Optical design of the PI-Test MEBT beam scraping system. In *Proc. of LINAC'16*, 2016. THPRC026.

[48] Tracewin code. http://irfu.cea.fr/dacm/logiciels/.

[49] L.R. Prost, R. Andrews, C.M. Baffes, J.-P. Carneiro, B.E. Chase, A.Z. Chen, E. Cullerton, P. Derwent, J.P. Edelen, J. Einstein-Curtis, D. Frolov, B.M. Hanna, D.W. Peterson, G.W. Saewert, A. Saini, V.E. Scarpine, A.V. Shemyakin, V.L. Sista, J. Steimel, D. Sun, A. Warner, and C. Richard. PIP-II injector test warm front end: Commissioning update. In *Proc. of HB'18*, June 2018. THYGBF2.

[50] A. Shishlo and A. Aleksandrov. Noninterceptive method to measure longitudinal twiss parameters of a beam in a hadron linear accelerator using beam position monitors. *Phys. Rev. ST Accel. Beams*, 16:062801, Jun 2013.

[51] A. Shishlo, A. Aleksandrov, Yong Liu, and Zhijun Wang. Measuring longitudinal beam parameters in the low energy section of the oak ridge spallation neutron source accelerator. *Phys. Rev. Accel. Beams*, 21:092803, Sep 2018.

[52] Cst studio suite. https://www.cst.com.

[53] S. Ahmed, G. Neveux, T. Reveyrand, D. Barataud, and J. M. Nebus. Time-domain interleaved high sampling rate system for large signal characterization of non-linear devices. In *79th ARFTG Microwave Measurement Conference*, pages 1–4, 2012.

[54] E. A. Essex. Hertz vector potentials of electromagnetic theory. *American Journal of Physics*, 45(11):1099–1101, 1977.

[55] Sebastien Artinian, Julien Bergoz, Frank Stulle, Bergoz Instrumentation, V. Schlott, and P Pollet. Goubau line and beam characterization of turbo-ict for swissfel. 05 2013.

[56] J. Musson, K. Cole, and S. Rubin. Application of Goubau Surface Wave Transmission Line for Improved Bench Testing of Diagnostic Beamline Elements. In *Particle Accelerator Conference (PAC 09)*, page TH6REP047, 2010.

[57] Frank Stulle and Julien Bergoz. The goubau line - surface waves for bench testing of beam instrumentation at high frequencies. 05 2012.

[58] J. X. Qiu, D. K. Abe, T. M. Antonsen, B. G. Danly, and B. Levush. Traveling-wave tube amplifier performance evaluation and design optimization for applications in digital communications with multilevel modulations. *IEEE Transactions on Microwave Theory and Techniques*, 51(8):1911–1919, 2003.

[59] G. Saewert, M. H. Awida, B. E. Chase, A. Chen, J. Einstein-Curtis, D. Frolov, K. Martin, H. Pfeffer, D. Wolff, S. Khole, and D. Sharma. First performance results of the pip2it mebt 200 ohm kicker prototype. 2018.

[60] A. Neureuther, P. Klock, and R. Mittra. A study of the sheath helix with a conducting core and its application to the helical antenna. *IEEE Transactions on Antennas and Propagation*, 15(2):203–210, 1967.

[61] X. Zhang, G. Yang, H. Ou, Z. Duan, Z. Wang, H. Gong, Y. Gong, Y. Zhao, Q. Deng, and Z. He. Theoretical investigation into an ultra-wideband helix traveling-wave tube. In *2019 International Vacuum Electronics Conference (IVEC)*, pages 1–2, 2019.

[62] Samuel Sensiper. *Electromagnetic wave propagation on helical conductors*. PhD thesis, Massachusetts Institute of Technology, 1951.

[63] G. N. Babu and R. J. Stanislaus. Fast wave propagation characteristics of dielectric loaded tape helix structures placed around and within a cylindrical core. In *2016 International Conference on Micro-Electronics and Telecommunication Engineering (ICMETE)*, pages 66–70, 2016.

[64] *Reference Data for Engineers: Radio, Electronics, Computers, and Communications*. Newnes, 9th ed. edition, 2001.